UNIVERSITY OF CALIFORNIA

Los Angeles

Aspects of RPE Cell Biology in Disease

A dissertation submitted in partial satisfaction of the

requirements for the degree Doctor of Philosophy

in Neuroscience

by

Roni Hazim

2018

ABSTRACT OF THE DISSERTATION

Aspects of RPE Cell Biology in Disease

by

Roni Hazim

Doctor of Philosophy in Neuroscience

University of California, Los Angeles, 2018

Professor David S. Williams, Chair

The RPE is a polarized epithelium, whose apical surface faces the outer segments of photoreceptor cells in the neurosensory retina, and performs numerous functions that are essential for healthy vision. In this dissertation, I investigated aspects of RPE biology that are critical for cellular homeostasis and, when perturbed, may contribute to RPE dysfunction and retinal degeneration. In particular, I focused on the RPE's phagocytic function in which the cells internalize shed disks of photoreceptor outer segments and subsequently degrade the resultant phagosomes, thereby maintaining photoreceptor health. Using in vitro models of RPE, phagocytosis assays were performed to test the kinetics of outer segment degradation using state-of-the-art live-cell imaging. The kinetics of this process were further tested in a mouse model of dominant Stargardt 3 macular degeneration, which showed that the digestion of mutant outer segments is delayed and thus contributes to photoreceptor degeneration. This

data implicated the impaired motility of phagosomes in the RPE as a major contributor to their delayed degradation, thereby identifying a sensitive measurement of a parameter that is critical to overall RPE health. Given that the RPE is a primary site of insult in retinal degeneration, cell transplantation may be a viable treatment to replace damaged RPE cells in human patients. To that end, we generated human RPE cells from induced pluripotent stem cells and extensively characterized the critical aspects of their cell biology. Importantly, we demonstrated that when these cells manifest phagosome degradation kinetics, comparable to that in vivo, and, when transplanted into a mouse model of retinal degeneration, they are capable of integrating into the host monolayer and partially rescue the photoreceptor from degenerating. Lastly, we developed a rapid method to differentiate a human immortalized RPE cell line such that the cultures exhibit many of the characteristics of their in vivo counterparts, and we propose that when these cells are properly differentiated, they can be used to draw meaningful inferences about RPE physiology and pathology.

The dissertation of Roni Hazim is approved.

Nicholas C Brecha

William Edward Lowry

Alapakkam P Sampath

David S. Williams, Committee Chair

University of California, Los Angeles

DEDICATION

First, I would like to thank the members of my doctoral committee for their expert advice and continuous support throughout my scientific training. I especially would like to thank my thesis advisor, Professor David Williams, for his mentorship and guidance throughout this period of my life. At the time that I first met David, his laboratory had been mainly run by postdoctoral researchers, with no graduate students, for quite some time. Nonetheless, David made it a mission to instill a great deal of confidence in me, and pushed me to perform at a higher standard than what may have been expected of a young PhD student. I can recall numerous instances when we would have discussions that lasted for hours, many of which went beyond midnight. Those interactions were the most memorable and the most useful for my training; after thorough analysis of experimental data, we would then formulate the next hypothesis and design the appropriate experiment to test it. As my confidence grew, David encouraged me to pursue my own ideas, allowed me to design my own experiments, and with his guidance, gave me the freedom to steer my projects in the directions of my choosing. Without a doubt, David's mentorship made me into a rigorous experimenter, one who can make careful observations, formulate a sound and testable hypothesis, design and execute carefully planned experiments, and compile data that make for an interesting story of publishable quality.

When it came to matters at the laboratory bench, I was fortunate to have supportive and knowledgeable lab mates who taught me numerous skills and techniques. Many of my lab mates, past and present, are co-authors on my published work. I would also like to express my gratitude to our research specialist, Barry Burgess, whose thirty-plus years of experience at the bench was invaluable to my training. In addition to teaching me various techniques and procedures, Barry always made himself available with open ears to listen to the countless problems I faced during my PhD, and more importantly, provide moral support for when things

would go wrong. To this day, he is still the first person I would go to when my experiments at the bench are not going as planned.

Last but not least, I would like to thank my parents, younger brother, and friends who stood by me and supported me during this important period of my life. To my parents, I would like to say thank you for your incredible sacrifices and for making my education a priority of the utmost importance. Without you, none of this would have been possible!

TABLE OF CONTENTS

Abstract *ii*

Dedication *v*

List of Figures and Tables *viii*

List of Acronyms *x*

Acknowledgements *xiii*

Vita *xiv*

Chapter 1: *1*

Introduction

Chapter 2: *19*

Cell Culture Analysis of the Phagocytosis of Photoreceptor Outer Segments by Primary Mouse RPE Cells

Chapter 3: *25*

Live-Cell Imaging of Phagosome Motility in Primary Mouse RPE Cells

Chapter 4: *30*

Defective Phagosome Motility and Degradation in Cell Non-Autonomous RPE Pathogenesis of a Dominant Macular Degeneration

Chapter 5: *59*

Differentiation of RPE cells from Integration-free iPS Cells and Their Cell Biological Characterization

Chapter 6: *89*

Rapid Differentiation of the Human RPE Cell Line, ARPE-19, induced by Nicotinamide

Chapter 7: *107*

Conclusions from the Present Studies

Appendix: *109*

Gene Therapy Approaches for Prevention of Retinal Degeneration in Usher Syndrome

References *116*

LIST OF FIGURES AND TABLES

Figure 1.1: Transverse section of a human eye----------2

Figure 1.2: A section of the multilayered retina----------4

Figure 2.1: Isolation of RPE, and purification of POSs from murine eyes----------20

Figure 2.2: Dual-labeling of opsin following a pulse-chase phagocytosis assay----------21

Figure 3: Method for monitoring phagocytosis of photoreceptor outer segments in live RPE----27

Figure 4.1: Retinal degeneration and localization of ELOVL4----------33

Figure 4.2: Detection of WT and mutant ELOVL4 by N-terminal ELOVL4 antibody----------35

Figure 4.3: Detection of ELOVL4 in TG2 phagosomes----------36

Figure 4.4: Degradation of POS phagosomes in WT and mutant mouse RPE in vivo----------37

Figure 4.5: Impaired degradation of mutant ELOVL4 POSs by WT RPE cultures----------39

Figure 4.6: Impaired motility of TG2 phagosomes in WT primary mouse RPE cells----------42

Figure 4.7: Tracking and analysis of phagosome motility----------44

Figure 4.8: Membranous debris in RPE of young TG2 mice----------45

Figure 4.9: Loss of ZO-1 junctional localization in TG2 RPE----------46

Figure 4.10: Increased oxidative stress in TG2 RPE----------47

Figure 4.11: Increased oxidative stress in WT RPE fed TG2 POSs----------48

Figure 4.12: Activated microglia in the retina of TG2 mice----------49

Figure 5.1: Reprogramming of human fibroblasts into induced pluripotent stem cells----------61

Figure 5.2: Differentiation of iPSCs intro retinal pigment epithelial cells----------63

Figure 5.3: Characterization of iPSCs-derived RPE cells----------64

Figure 5.4: Specific protein and gene expression profiling of iPSC-derived RPE cells----------66

Figure 5.5: Phagocytosis of photoreceptor outer segments by iPSC-RPE in vitro----------67

Figure 5.6: Quantification of phagocytosis in iPSC-RPE----------68

Figure 5.7: Microtubule organization and trafficking of endolysosomes in iPSC-RPE----------70

Figure 5.8: Alpha tubulin labeling in iPSC-RPE----------72

Figure 5.9: Tight junction proteins and the transepithelial resistance of iPSC-RPE----------74

Figure 5.10: Transplantation of human iPSC-RPE intro murine eyes----------76

Figure 6.1: Cellular morphology of differentiated ARPE-19 cells----------92

Figure 6.2: Expression profile and functional assessment of differentiated ARPE-19 cells-------96

Figure 6.3: Differentiated ARPE-19 cells possess apically-oriented cilia----------98

Figure 6.4: Karyotype analysis of chromosomes from ARPE-19 cells----------106

Appendix Figures and Tables

Figure 1: Strategies for gene augmentation therapies----------110

Table 1: List of Usher syndrome genes----------115

Supplementary Material

Movies S1 and S2: Phagosome motility in live RPE

Movie S3: Endolysosome motility in live iPSC-RPE

LIST OF ACRONYMS

$\alpha_V\beta_5$	Alpha V Beta 5
AAV	Adeno-associated virus
ABCA4	ATP binding cassette subfamily A member 4
Ad5	Adenovirus type 5
AMD	Age-related macular degeneration
AU	Arbitrary unit
BEST1	Bestrophin1
bp	Base pairs
BM	Bruch's membrane
BSA	Bovine serum albumin
Cas9	CRISPR associated protein 9
CFH	Complement factor H
COSs	Cone outer segments
CRISPR	Clustered regularly-interspaced short palindromic repeats
DAPI	4', 6-Diamidino-2-Phenylindole, Dihydrochloride
DIC	Dynein intermediate chain
DMEM	Dulbecco's modified eagle medium
DNA	Deoxyribonucleic acid
DPBS	Dulbecco's phosphate buffered saline
EBs	Embryoid bodies
ELOVL4	Elongation of very long chain fatty acids 4
ER	Endoplasmic reticulum
ESCs	Embryonic stem cells
FA	Formaldehyde
fAAV	Fragmented adeno-associated virus
FBS	Fetal bovine serum
FGF2	Fibroblast growth factor 2
FOV	Field of view
FSP-1	Fibroblast-specific protein-1

GAPDH	Glyceraldehyde-3-phosphate dehydrogenase
GFP	Green fluorescent protein
gRNA	Guide RNA
HBSS	Hank’s balanced salt solution
HEK	Human embryonic kidney
HDR	Homology-directed recombination
HR	Homologous recombination
iPSC	Induced pluripotent stem cells
IRBP	Interphotoreceptor retinoid-binding protein
MITF	Microphthalmia-associated transcription factor
4-HNE	4-Hydroxynonenal
MEM-α	Minimum essential medium alpha
MerTK	Mer tyrosine kinase
MFGE8	Milk fat globule-EGF factor 8
NDS	Normal donkey serum
NEAA	Non-essential amino acids
NGS	Normal goat serum
NHEJ	Non-homologous end joining
ON	Optic nerve
ONL	Outer nuclear layer
OPL	Outer plexiform layer
oxPC	Oxidized phosphotidylcholine
PEDF	Pigment epithelial derived factor
PCR	Polymerase chain reaction
PIS	Photoreceptor inner segments
POS	Photoreceptor outer segments
RGCs	Retinal ganglion cells
RHO	Rhodopsin
RNA	Ribonucleic acid
ROSs	Rod outer segments
RPE	Retinal pigment epithelium

RPE65	Retinal pigment epithelium-specific protein 65 KDa
SD	Standard deviation
SEM	Standard error of mean
SNP	Single nucleotide polymorphism
STGD3	Stargardt macular dystrophy 3
TER	Transepithelial resistance
TGFB1	Transforming growth factor beta 1
VEE	Venezuelan equine encephalitis
VEGF	Vascular endothelial growth factor
WT	Wildtype
ZO-1	Zona occluden-1

ACKNOWLEDGMENTS

I have had the pleasure of working with numerous wonderful collaborators throughout my PhD. These collaborators also became my fellow co-authors on the papers I have published during the course of my training. Chapters 2-5, as well as the Appendix chapter, of my dissertation are modified from work that has already been published as follows: Chapter 2 (Hazim and Williams, 2018); Chapter 3 (Hazim et al., 2016); Chapter 4 (Esteve-Rudd et al., 2018); Chapter 5 (Hazim et al., 2017); Appendix (Williams et al., 2017). The contributions of each person listed as a co-author on the published works mentioned above are listed in the original articles published online. Chapter 6 is modified from a manuscript that we have submitted to the peer-reviewed journal, *Experimental Eye Research*. This work lists Roni Hazim as the first author, with Dr. Stefanie Volland, Alice Yen (undergraduate trainee), Barry Burgess, and Dr. David Williams as co-authors. The manuscript was reviewed, and is currently in revision.

I am grateful for the financial support that made all this work possible, including an NEI Vision Science Training Grant (T32EY007026), and an NIH NRSA (F31) Fellowship (F31EY026805).

VITA

EDUCATION

University of California, Irvine (UCI) 2008 – 2012
Bachelor of Science in Developmental and Cell Biology (*cum laude*)

PUBLICATIONS

- Esteve-Rudd J, **Hazim RA***, Diemer T, Paniagua AE, Volland S, Umapathy A, Williams DS. Defective phagosome motility and degradation in cell nonautonomous RPE pathogenesis of a dominant macular degeneration. PNAS. 2018;115: 5468-5473.
- **Hazim RA**, Williams DS. Cell culture analysis of the phagocytosis of photoreceptor outer segments by primary mouse RPE cells. Methods in Molecular Biology. 2018; 63-71.
- **Hazim RA***, Karumbayaram S, Jiang M, Dimashkie A, Lopes VS, Li D, Burgess BL, Vijayaraj P, Alva-Ornelas JA, Zack JA, Kohn DB, Gomperts BN, Pyle AD, Lowry WE, Williams DS. Differentiation of RPE cells from integration-free iPS cells and their cell biological characterization. Stem Cell Research & Therapy. 2017;8:1-17.
- Williams DS, Chadha A, **Hazim R***, Gibbs D. Gene therapy approaches for prevention of retinal degeneration in Usher syndrome. Gene Ther. 2017;24:68-71.
- **Hazim R***, Jiang M, Esteve-Rudd J, Diemer T, Lopes VS, Williams DS. Live-cell imaging of phagosome motility in primary mouse RPE cells. Adv Exp Med Biol. 2016;854:751-5.

*** co-first author**

POSTERS AND PRESENTATIONS

- **Hazim, RA,** Volland, S, Yen, A, Burgess, BL, Williams, DS. A rapid protocol for the differentiation of human ARPE-19 cells. ARVO, Honolulu, Hawaii, USA, May 2018.
- **Hazim, R**, Williams, DS. Mutations in CFH perturb RPE homeostasis *in vitro*. ARVO, Seattle, Washington, USA, May 2016.
- Williams, DS, Esteve, J., **Hazim, R.,** Diemer, T., Radu, R. Defective processing of POS phagosomes from mutant *ELOVL4* retinas by the RPE. XVIIth International Symposium on Retinal Degeneration, Kyoto, Japan, September 2016.
- **Hazim, R**, Burgess, B, Williams, D. Live imaging of organelle trafficking in differentiated ARPE-19 cells. FASEB (The Biology and Chemistry of Vision), Big Sky, Montana, USA, June 2015.
- Karumbayaram, S, Dimashkie, A, Lopes, V, **Hazim, R**, Alva-Ornelas, J, Radu, R, Galic, Z, Byrne, J, Gomperts, B, Pyle, A, Clark, A, Kohn, D, Zack, J, Lowry, W, Williams, D. RPE cells derived from iPSCs for cell replacement therapy. BSCRC Annual Stem Cell Symposium, Los Angeles, California, USA, February 2015.
- **Hazim, R**, Esteve-Rudd, J, Diemer, T, Zhang, K, Williams, D. Stargardt-3 macular degeneration: Defective processing of photoreceptor outer segments by RPE cells. XVIth International Symposium on Retinal Degeneration, Pacific Grove, California, USA, July 2014.

ACADEMIC & RESEARCH AWARDS

Stein Eye Institute Pre-Doctoral Research Fellow Award, UCLA	2018
NIH NRSA (F31) Fellowship Recipient, UCLA	2017 – 2018
NEI Vision Science Training Grant Recipient, UCLA	2013 – 2016
Young Investigator Travel Award, RD Conference; Monterey Bay, CA	2014

TEACHING EXPERIENCE

Teaching assistant for Molecular and Developmental Neuroscience, UCLA	2018

Chapter 1

Introduction

1.1 The Eye

Vision is one of our five primary senses, and is certainly vital to our ability to interact with the objects in our surrounding while appreciating the beauty of the world. The organ responsible for our sense of vision is the eye, an asymmetrical sphere consisting of three distinct layers (Kolb, 2007). The external layer serves a protective role for the eye and includes the **cornea** and **sclera**. The former is a transparent barrier against microbes and dirt particles, and is important for focusing incoming light, while the latter is an avascular dense fibrous tissue that maintains the shape of the eye and also provides anchorage for extraocular muscles that move the eye. The intermediate layer is composed of the iris and ciliary body in the anterior region, and the choroid in the posterior region. The **iris** is the part of the eye that gives us our distinct eye color; it surrounds the **pupil**, changing its size to control how much light enters the eye. Directly behind the iris is the **lens**, a transparent structure that bends the light entering from the pupil such that a clear image of the visual field is formed at the back of the eye. The shape of the lens is controlled by the ciliary muscles, important components of the **ciliary body**, which also secretes a clear liquid, called the aqueous humor, that fills the anterior chamber of the eye. The **choroid** is a vascular layer consisting of blood vessels that supply oxygen and nutrients to various layers in the eye. Lastly, the internal layer of the eye consists of the neurosensory **retina** (Kolb, 2007).

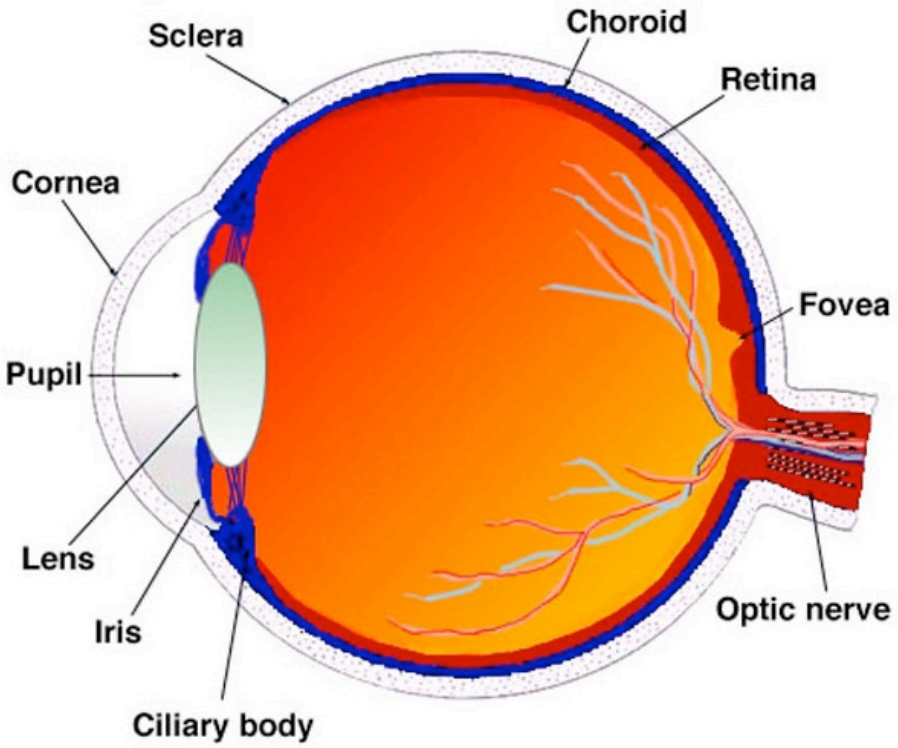

Figure 1.1: Transverse section of a human eye.

1.2 Neurosensory Retina

The neurosensory retina is a multilayered tissue in the posterior of the eye whose main functions include the (1) detection of light entering the eye, (2) the conversion of the light stimulus to a chemical signal, and (3) the rely of that signal to regions of the brain where it can be processed for visual information. The retina is a part of the central nervous system; it is derived from an embryonic structure called the neural tube, which also gives rise to the brain and spinal cord (Kolb, 2007). Similar to the cerebral cortex, the neurosensory retina develops in an inside-to-outside manner; thus, the retinal ganglion cells are the first cells to be born while the photoreceptor cells are the last to mature (Rapaport, 2006). The retinal layers in between form as a consequence of cell division and subsequently cell migration.

When light enters the eye, it is detected by the **photoreceptor cells**, which include rods and cones. The rods far out number the cones in all regions of the retina, with the exception of a pitted region in the middle of the retina known as the fovea. The rod cells are also significantly more sensitive to light than the cones, and therefore are better suited for scotopic vision (i.e. night vision). The cones on the other hand require higher levels of light to become active and thus contribute to our photopic vision (i.e. daylight vision) (Chien et al., 2000). While rods exist as a single cell type, the cones in a human retina come in three different varieties, each sensitive to a particular range of wavelengths of light (short, middle and long). It is these cone photoreceptors (S-, M-, and L-cones) that allow us to see the world in color and with high spatial acuity (Imai et al., 2005).

Following light detection by the photoreceptor cells, the signal is relayed to the **bipolar cells**, many of which synapse directly onto **retinal ganglion cells (RGCs)**; the RGCs project their axons, which are bundled together to form the optic nerve, to the brain for visual processing. In addition to this vertical flow of visual information, there is also a lateral pathway that is carried out by the **horizontal** and **amacrine cells**. These interneurons mediate interactions between photoreceptors and bipolar cells (horizontal) and interactions between bipolar cells and RGCs (amacrine). Both cell types integrate visual information as it travels to the RGCs in order to increase contrast and thereby enhance object detection in the visual field.

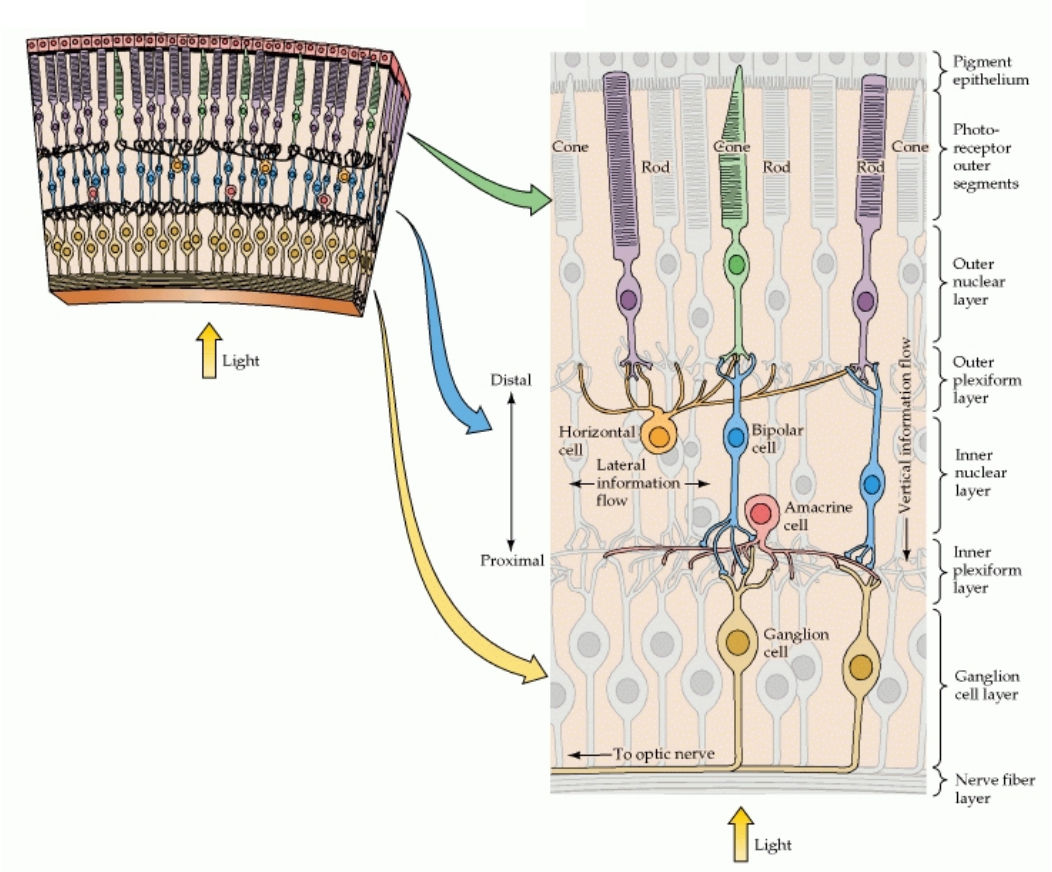

Figure 1.2: Modified from Purves Neuroscience 2nd edition. A section of the multilayered retina. Incoming light first reaches the nerve fiber layer, which consists of the axons of retinal ganglion cells. The next group of cells to come into contact with light are the bipolar, horizontal, and amacrine cells, all of which have cell bodies that occupy the inner nuclear layer. The synapses that these cells make with each other and with the ganglion cells localize to the inner plexiform layer. Posteriorly, the photoreceptor cells have their cell bodies in the outer nuclear layer, while synapsing with bipolar cells in the outer plexiform layer. Light is detected in the outer segments of rod and cone photoreceptor cells. These outer segments are in direct contact with an adjacent layer of pigmented epithelium.

1.3 Retinal Pigment Epithelium

Directly adjacent to the outer segments of photoreceptors is a monolayer of epithelial cells known as the retinal pigment epithelium (RPE). This monolayer is situated above a five-layered lamina called Bruch's membrane, which includes an inner and outer layer of collagen, and a central layer of elastin; the inner- and outer-most layers are formed by the basal membranes of the RPE and the capillaries of the choroid (choriocapillaris), respectively (Booij et

al., 2010). The RPE serves numerous essential functions that maintain retinal homeostasis, and is believed to be the primary site of pathogenesis for various retinal degenerative diseases.

1.3.1 RPE Functions

1.3.1.1 Visual Cycle

When light hits the photoreceptor outer segments, it activates the G-protein-coupled receptor, rhodopsin, which is studded onto the millions of disk membranes that are stacked throughout the outer segment. The rhodopsin molecule is composed of a visual chromophore (11-*cis* retinal) attached to an opsin protein. The 11-*cis* retinal is converted to an all-*trans* configuration in the presence of light (Mannu, 2014). To ensure proper photoreceptor function, the all-*trans* retinal must be reisomerized to 11-*cis* retinal. The reisomerization of the chromophore, a process known as the visual cycle, occurs in the RPE. The all-*trans* retinal is detached from the opsin protein, released from the outer segment disk membrane into the interphotoreceptor matrix, and transported to the RPE by a carrier protein called interphotoreceptor retinoid binding protein (Kiser et al., 2014).

Inside the RPE, the visual cycle continues with three enzymatic reaction, including esterification (performed by lecithin retinol acyl transferase), simultaneous hydrolysis and isomerization (performed by RPE65) (Jin et al., 2005), and oxidation (performed by 11-*cis* retinol dehydrogenase). These enzymatic reactions regenerate 11-*cis* retinal that is able to cross the interphotoreceptor matrix and return to the photoreceptors.

1.3.1.2 Blood-Retina Barrier

Like many other types of epithelial cells in the body, the RPE acts as a barrier, regulating the flow of water, solute, nutrients, and waste between the choriocapillaris and the neurosensory retina (Strauss, 2005). While the plasma membrane of the RPE cells contributes

to this barrier by impeding the movement of hydrophilic solutes, an intercellular seal must also be formed to regulate substance movement between the cells that make up the barrier. This seal is formed by apically-located junctional complexes, including adherens and tight junctions. Both of these junctions require proper organization of the cell's actin cytoskeleton.

The adherens junction forms prior to the tight junction, initiating and stabilizing the adhesion of neighboring cells (Nusrat et al., 2000). It is composed of transmembrane, calcium-dependent proteins called cadherins and cytoplasmic proteins known as catenins, which facilitate the interactions of cadherins with the actin cytoskeleton (Hartsock and Nelson, 2008). Members of the cadherin proteins include E-cadherins and N-cadherins, which are found in epithelial tissue and neurons, respectively. The RPE is unusual in that it predominately expresses N-cadherin rather than E-cadherin (McKay et al., 1997; Youn et al., 2006).

The tight junction is further apically-located than the adherens junction and performs two main functions in epithelial cells, including limiting paracellular movement of solutes, and preventing the mixing of apical membrane proteins with those found in the basal-lateral membrane. This type of junction is composed of integral membrane proteins, including occludin and claudin, as well as cytoplasmic proteins belonging to the zonula occludens family, which interact with the filaments of the actin cytoskeleton (Hartsock and Nelson, 2008). The permeability of tight junctions varies across different types of epithelial cells; in epithelial cell culture models, the permeability of the tight junction can be indirectly inferred by measuring the transepithelial resistance across the cell monolayer (Rahner et al., 2004).

1.3.1.3 Phagocytosis of Photoreceptor Outer Segments

One of the primary functions of the RPE that is essential for retinal health and vision is the phagocytosis of photoreceptor outer segments (POS). The outer segment of a photoreceptor cell is a specialized cilium that contains millions of membrane disks, each

studded with rhodopsin molecules that allow for the detection of light entering the eye. These disks are continuously renewed at the base of the outer segment while those at the tip of the outer segment are shed on a daily cycle (Young, 1967; LaVail, 1976). These two opposing processes at the ends of the outer segment ensure a constant supply of light-sensing disks in a postmitotic cell that maintains its length during the lifetime of the animal.

The shed tips of the POS are phagocytized by the adjacent RPE, and the resultant POS phagosomes are subsequently degraded (Young and Bok, 1969). As this process occurs on a daily basis and throughout the animal's lifetime, the RPE is widely considered a professional phagocyte in the retina. In fact, each RPE cell in the murine retina is responsible for more than 200 photoreceptor cells, representing an exorbitant amount of material that requires efficient clearance (Volland et al., 2015).

The mechanisms of POS binding, internalization, and degradation have been elucidated using RPE cell culture models. At light onset, the distal tips of POS expose their phosphatidylserines, which serve as "eat me" signals (Ruggiero et al., 2012). This signal is recognized by an RPE-secreted protein called milk fat globule-EGF Factor 8 (MFG-E8), which is the ligand of the calcium-dependent integrin receptor alpha V beta 5 ($\alpha_V\beta_5$) that is expressed on the apical surface of the RPE. Lack of $\alpha_V\beta_5$ function, or absence of MFG-E8, in the RPE results in the loss of the phagocytic burst that occurs following the circadian shedding of the distal POS tips (Nandrot et al., 2004; Nandrot et al., 2007). Further evidence that $\alpha_V\beta_5$ mediates POS binding came from in vitro phagocytosis assays on cultured RPE cells in which function-blocking antibodies against the receptor significantly reduced the number of POS capable of binding to the apical surface of the RPE (Finnemann et al., 1997). The internalization of the POS occurs via a tyrosine-kinase receptor called MerTK, that is also expressed on the apical surface of the RPE. Loss of MerTK function in the RPE, or the absence of the receptor's two ligands, Gas6

and Protein S, diminishes the ability of the cells to engulf bound POS (Bok and Hall, 1971; Edwards and Szamier, 1977; D'Cruz et al., 2000). Humans that have mutations in MerTK develop retinal degeneration (Gal et al., 2000).

Once engulfed, the POS entity (now referred to as a phagosome), relies on the RPE cytoskeleton and its associated motor proteins to transport it along the apical-basal axis such that it encounters degradative organelles, including endosomes and lysosomes, and eventually undergoes degradation (Herman and Steinberg, 1982b; Gibbs et al., 2003; Jiang et al., 2015).

1.3.2 Cytoskeleton

The cytoskeleton of cells is made up of three classes of filaments, which from smallest to biggest, include actin, intermediate filaments, and microtubules. These components provide structural integrity, anchor and transport organelles within the cytoplasm, and give the cell its overall shape. In the case of the RPE, the cytoskeleton is organized such that the cells form a simple epithelium with cobblestone morphology (Bonilha, 2014).

1.3.2.1 Actin Filaments and Myosin Motors

Actin filaments, which have an average diameter of 7 nm, consist of globular actin monomers linked together to form a double helical strand. The assembly of actin filaments begins with a nucleation step in which a complex is formed from 3-4 actin monomers. This actin nucleus then begins to elongate by the addition of actin monomers to both sides. The process continues until the concentration of actin monomers is in equilibrium with that of the actin filament. Although monomers are added to both ends of the actin filament during the assembly, the rate at which these subunits are added is much greater at one end (plus end) relative to the other end (minus end), making the actin polymer a highly dynamic and polarized structure (Svitkina, 2018).

In the RPE, the actin cytoskeleton undergoes significant rearrangement as the cells transition from a growth phase to a differentiated state; during the former, the cells exhibit a fusiform morphology as their actin filaments are arranged into structures known as stress fibers that are present throughout the cytoplasm. As the cells differentiate, the actin filaments become restricted to the cortex of the cytoplasm, adjacent to the plasma membrane, and near the apical junctions. In addition to this cortical actin, the RPE contains numerous actin-rich structures called microvilli which protrude from the apical surface of the RPE and interdigitate the POS in the retina (Turksen and Kalnins, 1987).

The cytoskeletal motors associated with actin are the myosins. These motors consist of heavy chains (usually one or two) and various light chains. Structurally, they are organized into three domains, each of which serves a distinct function. The head domain has ATPase activity allowing the energy from ATP hydrolysis to be used as fuel for motility. The adjacent neck region contains regulatory domains that modulate the activity of the head domain. Lastly, the third region is the tail domain which contains the cargo binding sites that dictate which organelles will be transported on a particular myosin motor (Cope et al., 1996).

One cargo that is heavily dependent on functional myosin activity in the RPE is the POS-derived phagosome. It has been shown that mice lacking myosin 7a exhibit impaired migration of phagosomes from the actin-rich apical region of the RPE, and subsequently develop retinal degradation (Gibbs et al., 2003). Humans with myosin 7A mutations develop Usher syndrome, which is characterized by partial or complete loss of vision and hearing (Gibson et al., 1995; Weil et al., 1995). Once the phagosomes migrate across the actin meshwork, they transition to the microtubule cytoskeleton where their motility becomes mediated by kinesin and dynein motor proteins.

1.3.2.2 Microtubules and Kinesin and Dynein Motors

The microtubules are the largest of the cytoskeletal elements, with an average diameter of 25 nm. They consist of 13 protofilaments surrounding a hollow core; each protofilament is a polypeptide of tubulin dimers composed of an alpha and beta tubulin monomer. Similar to the actin filaments, microtubules are very dynamic and polarized structures; tubulin is removed more readily from the minus end and added to the plus end. Microtubule assembly occurs at organizing centers known as centrosomes, which anchor the minus end of the microtubules, allowing the plus end to extend towards the cell's periphery.

In epithelial cells such as the RPE, the centrosomes localize to the apical region of the cell. Emanating from the centrosomes are horizontally-oriented microtubules as well as vertically-oriented microtubules that extend basally (Musch, 2004). Additionally, microtubules that protrude from the apical surface of the RPE give rise to the primary cilium. Similar to the actin filaments, the microtubules are essential to the transport of organelles, including phagosomes, in the RPE.

In a previous study, it was shown that inhibition of microtubule polymerization using the drug colchicine disrupted the motility of phagosomes in the opossum RPE, resulting in their accumulation in the apical region (Herman and Steinberg, 1982a). These observations underlie the importance of microtubules in delivering phagosomes across the apical-basal axis of the RPE. Phagosomes travel along the microtubules via molecular motors belonging to the kinesin and dynein families of proteins. A kinesin motor consists of a heavy chain and a light chain, each of which has structurally distinct domains. The head domain serves as an ATPase, binding one molecule of ATP and anchoring the motor to the microtubule. The tail domain attaches the cargo to the motor, allowing for movement upon ATP hydrolysis (Goldstein and Yang, 2000). Kinesins are generally considered plus-end-directed motors because they transport their cargo towards the plus-end of a microtubule. In contrast, dyneins are minus-end-directed and therefore move their cargo towards a microtubule's minus end (Goodson et al., 1997). Although

both classes of motors share similar structural domains, the dynein motors are relatively larger in size (Vale, 2003). The loss of function of kinesin light chain 1 in vivo has been shown to impair phagosome degradation by mouse RPE cells as well as contribute to symptoms of a retinal degenerative disease known as age-related macular degeneration (Jiang et al., 2015).

1.4 Retinal Degenerative Diseases

Given the numerous functions the RPE performs to maintain retinal health, insult or injury to this epithelial monolayer is often the primary cause or a major contributor to the development and progression of retinal degenerations (Curcio et al., 1996; Zarbin, 2004; Bhutto and Lutty, 2012). Ultimately, these degenerations result in the loss of photoreceptor cells and therefore partial or complete blindness. Retinal degenerations can be caused by inherited monogenic diseases or complex disorders in which genetic and environmental factors influence the development, progression, and severity of the disease.

1.4.1 Stargardt's Macular Dystrophy

Stargardt's disease was described more than a century ago and encompasses genetically inherited forms of macular degeneration, characterized by lipofuscin accumulation in the macular region of the retina, which then leads to photoreceptor death and subsequently, bilateral vision loss. The disease represents the most common form of inherited macular degeneration, with an incidence rate between 1:8,000 and 1:10,000, and affected individuals may begin to experience symptoms as early as their teen years (Spiteri Cornish et al., 2017).

By the far, the most common form of Stargardt disease is Stargardt 1 (STGD1), a recessively-inherited form that is caused by mutations in the gene *ABCA4* (ATP Binding Cassette Subfamily A Member 4) on chromosome 1 (Allikmets et al., 1997). ABCA4 is a protein expressed in photoreceptor cells and plays an essential role in the visual cycle (see section 1.3.1.1). Similar to other members of the ABC family, this protein utilizes ATP to actively

transport molecules across lipid bilayers. In photoreceptor cells, ABCA4 is found in the disk membranes of the outer segments where it transports a molecule of all-trans retinaldehyde that is covalently bound to phosphatidylethanolamine from the intradiskal lumen to the cytoplasm such that it can be reduced and subsequently relayed to the RPE for recycling (Sun and Nathans, 2000). Although there are currently no treatments for STGD1, gene augmentation, in which the mutant *ABCA4* is repaired or replaced, may become feasible in the near future.

Similar to Stargardt 1 disease, Stargardt 3 (STGD3) is a form of early-onset macular degeneration characterized by the loss of bilateral central vision. STGD3 patients typically begin to experience vision loss as early as childhood or adolescence, which progressively worsens throughout early adulthood. The disease has an autosomal dominant form of inheritance and is caused by mutations in the gene encoding the enzyme elongation of very long chain fatty acids 4 (ELOVL4), which is located on human chromosome 6 (Zhang et al., 2001).

ELOVL4 is the rate-limiting enzyme that catalyzes the synthesis of very long-chain fatty acids (Agbaga et al., 2008). The enzyme is expressed in photoreceptor cells and localizes to the endoplasmic reticulum (ER). STGD3 patients have a 5-base-pair deletion that truncates the C-terminus of ELOVL4 resulting in the loss of the ER retention signal (Edwards et al., 2001; Zhang et al., 2001). Because of the dominant inheritance pattern of the disease, several studies have been conducted to understand the effects of the mutated protein on the wildtype protein. Cell culture models in which the wildtype and mutant protein have been exogenously expressed suggested that while the wildtype protein properly localizes to the ER, it mislocalizes to the cytoplasm in the presence of the mutant protein (Karan et al., 2004). Additional in vitro data suggested that the mutant ELOVL4 protein is non-functional (Logan et al., 2013). In contrast, in vivo data from frog and mammalian photoreceptors show no effect of the mutant protein on the localization of the wildtype protein, as well as no changes in the levels of very long chain fatty acids (Grayson and Molday, 2005; Sommer et al., 2011). Various mouse models, including

knock-in of mutant *Elovl4* and transgenic mutant *ELOVL4*, have implicated RPE pathology as a significant contributor to the degeneration of photoreceptor cells (Karan et al., 2005; Vasireddy et al., 2006).

1.4.2 Age-related Macular Degeneration

In addition to inherited forms of macular degeneration, there are complex diseases that result in vision loss due to a combination of genetic traits and environmental factors. The leading cause of vision loss in the developed world is a complex disease known as age-related macular degeneration (AMD) (Montezuma et al., 2007). Similar to other forms of macular degeneration, AMD is characterized by central vision loss with accumulation of yellow sub-RPE deposits called drusen, which consist of lipids and proteins. A subtype of AMD, known as dry AMD, presents with drusen, which increase in size and number as the disease progresses, followed by photoreceptor and RPE degeneration. A more severe form of the disease is called wet AMD, in which blood vessels from the choroid begin to invade the subretinal space and grow towards the macula. These abnormal blood vessels are leaky in nature, and therefore have a tendency to leak fluid that results in damage to the macula. Ironically, only the more severe and wet form of AMD has treatments currently available in the clinic; patients with wet AMD can receive injections of antibodies against vascular endothelial growth factor (VEGF), a protein that contributes to the growth of new blood vessels. Efforts to develop new treatments for AMD have focused on animal and cell culture models that test the contribution of genetic disease-susceptibility loci to AMD pathology.

There have been several genes shown to be linked to AMD using genome-wide association studies. One gene that confers a high risk is complement factor H (*CFH*) (Edwards et al., 2005; Haines et al., 2005; Klein et al., 2005), which encodes a negative regulator of the complement pathway, a component of the innate immune system that functions to activate

phagocytic cells which are then able to clear microbes and damaged cells. A genetic haplotype that includes amino acid substitutions at positions 62 and 402 (I62V and Y402H, respectively) of the CFH polypeptide is thought to account for approximately 50% of the attributable risk for AMD (Hageman et al., 2005). This haplotype has been shown previously in cell-free systems to exhibit decreased binding affinity for by-products of oxidative stress, including oxidized phospholipids and malondialdehyde (Weismann et al., 2011; Shaw et al., 2012). Such by-products of oxidative stress are reported to disrupt the permeability and, therefore, barrier function of endothelial and epithelial cells, including the RPE. While understanding the cellular mechanisms by which CFH, a protein synthesized by the RPE in the retina (Kim et al., 2009b; Ding et al., 2015), contributes to AMD pathology may lead to effective therapeutic treatments, cell replacement strategies may offer promising remedies to replace damaged RPE cells in the retina and potential halt the progression of AMD and other forms of retinal degeneration.

1.5 Sources of Human RPE Cells

Cell culture models allow the experimenter to test hypotheses in relations to the basic cell biology of the RPE as well as pathogenesis of retinal diseases under controlled and well-defined conditions. Furthermore, RPE cultures in vitro can be harvested for the purpose of cell transplantation into animal models of retinal degeneration and, potentially in the near future, into human patients. The current sources of human RPE cells include immortalized cell lines, primary cultures from human donor eyes, and those derived from pluripotent stem cells.

1.5.1 Stem Cell-Derived RPE

1.5.1.1 Pluripotent stem cells

Pluripotent stem cells have revolutionized the field of biomedical sciences due to their ability to become any cell type in the body. This allowed them to be used for establishing disease-in-a-dish models, which potentially could shed light on cellular mechanisms of certain

diseases, and for in vivo transplantation to replace damaged or lost cells of a particular tissue (Israel et al., 2012; Singh et al., 2013b). Historically, pluripotent stem cells were acquired from the inner cell mass of a blastocyst, a structure found in the early developmental stages of a human embryo (Thomson et al., 1998). Because these cells were isolated from human fetal tissue, many ethical topics surround their use for biomedical research. More recently, pluripotent stem cells can be induced by reprogramming differentiated cells using expression vectors that exogenously express master regulatory transcription factors that are necessary for maintaining pluripotency in embryonic stem cells (Takahashi et al., 2007). These induced pluripotent stem cells (iPSCs) are the likely candidates for producing cells for transplantation purposes since they can be derived from the patient's own cells; this circumvents the need for immunosuppression which would otherwise be necessary if the cells are derived from embryonic stem cell lines (Kamao et al., 2014; Mandai et al., 2017).

1.5.1.2 iPSC-derived RPE

iPSCs have been shown to differentiate into RPE both spontaneously and via lineage-directed methods, with the latter method being more efficient and relatively less time-consuming (Buchholz et al., 2009; Buchholz et al., 2013). From a differentiation standpoint, RPE cells can be easily identifiable due to their pigmentation and cobblestone appearance. Once isolated and purified from a heterogeneous culture of differentiating iPSCs, these RPE cells can form a polarized epithelial monolayer that expresses RPE-specific proteins, and perform RPE-specific functions including the phagocytosis of photoreceptor outer segment disk membranes (Idelson et al., 2009; Liao et al., 2010). One important characteristic of iPSC-derived RPE cells is that, unlike the immortalized RPE cell lines, they are capable of establishing tight junctions that create a selectively-permeable barrier; this is evident by a high transepithelial resistance across the monolayer. The major drawback of these cells, however, is that their use in culture is limited to the number of passages they underwent since their derivation. A previous study has shown

that iPSC-derived RPE cells that reach beyond their fourth passage in vitro begin to lose their RPE qualities, and instead acquire a mesenchymal phenotype (Singh et al., 2013a).

In Chapter 5, we performed functional characterization of iPSC-derived RPE cells and demonstrated that the cells possess many of the properties of their in vivo counterparts. Importantly, and in relevance to the clinical application of these cells, we demonstrated that iPSC-derived RPE cells injected into murine retinas are capable of integrating into the host RPE monolayer and can partially rescue photoreceptor degeneration in a mouse model of retinal degeneration.

1.5.2 Immortalized RPE Cell Lines

There are several immortalized human RPE cell lines currently being used in the laboratory. The immortalization of some lines, including ARPE-19 and D407, occurred spontaneously (Davis et al., 1995; Dunn et al., 1996), while others such as hTERT-RPE1 were immortalized by exogenously expressing human telomerase. By far, the most commonly used cell line is ARPE-19, which was derived from primary RPE cells isolated from a 19-year-old male donor approximately two decades ago (Dunn et al., 1996).

Upon its derivation, the ARPE-19 cell line exhibited many features of in vivo RPE cells, including pigmentation, polygonal morphology, and expression of RPE-specific proteins (Dunn et al., 1996). However, after numerous passages in culture, the cells have lost many of their RPE characteristics, acquiring a fibroblastic, rather than epithelial, morphology. Interestingly, ARPE-19 cells still retain the ability to phagocytize isolate photoreceptor outer segments, albeit with significantly slower kinetics than primary cultures. Many protocols have been published describing methods to differentiate ARPE-19 cells such that they reacquire the characteristics of their in vivo counterparts, however, these methods have proven to be quite time consuming, often requiring more than 2 months (Ahmado et al., 2011; Samuel et al., 2017). Given how often

this cell line is used to study RPE cell biology, it is imperative that the cells be properly differentiated such that meaningful inferences can be made from their utilization. To that end, we developed a method to rapidly differentiate ARPE-19 cells and demonstrated that the cells have many features of a polarized RPE; this method is described in Chapter 6.

1.6 The Present Studies

In this dissertation, I have conducted a series of studies investigating critical aspects of the RPE that are relevant to disease, including cellular morphology, cytoskeleton arrangement, and organelle motility. These aspects are of particular importance for one of the primary functions of the RPE, the phagocytosis of photoreceptor outer segments. In Chapters two and three of this dissertation, I presented two methods which allowed me to test the phagocytic function of the RPE, and in particular, the kinetics of the process, using in vitro cell culture models. The method outlined in Chapter two relies on immunocytochemistry to monitor the degradation of POS-derived phagosomes, while the method outlined in Chapter three utilizes state-of-the-art spinning disk confocal microscopy to track the motility of phagosomes inside live RPE cells.

During the process of phagocytosis, the RPE must bind, ingest, and degrade photoreceptor outer segments that travel through the cytoplasm in organelles known as phagosomes. Because these phagosomes must interact with degradative organelles in the cell, it is essential that they are trafficked properly on molecular motors travelling on cytoskeletal elements, including actin filaments and microtubules. In Chapter four of this dissertation, I presented data underscoring of the importance of proper phagosome motility whereby defective trafficking of phagosomes delayed their degradation by RPE cells that phagocytized mutant photoreceptor outer segments derived from the retinas of a mouse model of STDG3, a human retinal degenerative disease with early-onset vision loss. Moreover, I demonstrated that the

defect in phagosome motility is partially due to abnormal association with the microtubule-based motor, dynein.

The importance of the RPE aspects mentioned above warrants cell culture models of human RPE cells that closely resemble their in vivo counterparts in order to provide meaningful inferences about RPE biology and pathology. Chapters five and six of this dissertation describe the derivation of such models from human induced pluripotent stem cells as well as an immortalized human RPE cell line, respectively. In particular, the RPE derived from induced pluripotent stem cells were shown, once extensively characterized in vitro, to partially rescue photoreceptor degeneration in a mouse model where the RPE's phagocytic function is compromised. The transplantation of extensively-characterized RPE cells into patients suffering from RPE dysfunction and retinal degeneration is a promising type of therapy for certain blinding diseases.

Hence, the body of work described in this dissertation highlights important aspects of the RPE that are essential for maintaining cellular health. When these are compromised, they can contribute to RPE dysfunction, retinal degeneration, and ultimately, blindness.

Chapter 2

Cell Culture Analysis of the Phagocytosis of Photoreceptor Outer Segments by Primary Mouse RPE Cells

2.1 Introduction

The retinal pigment epithelium (RPE) is situated between the light-sensitive photoreceptor cells, and the fenestrated choriocapillaris (Strauss, 2005).This single monolayer of cells performs numerous functions that are essential for the health of the retina, including the phagocytosis of photoreceptor outer segment (POS) disk membranes (Young and Bok, 1969). This phagocytosis allows for the catabolic phase of the renewal of the disk membranes (Young, 1967), and requires intimate contact between the RPE and POSs (Williams and Fisher, 1987). The apical surface of the RPE is decorated with proteins, including integrin alpha V beta 5 and Mer, receptors that have been shown to participate in the binding and internalization of the tips of the POSs by RPE cells, respectively (Lin and Clegg, 1998; D'Cruz et al., 2000). Once internalized, the POS phagosomes travel on molecular motors bound to cytoskeletal elements, including actin filaments and microtubules (Gibbs et al., 2003; Jiang et al., 2015), which mediate their fusion with degradative organelles such as endosomes and lysosomes (Bosch et al., 1993b; Wavre-Shapton et al., 2014).

Phagocytosis of the POS disk membranes shed by photoreceptor cells occurs on a daily cycle (LaVail, 1976). In the mouse retina, a single RPE cell serves up to 200 photoreceptor cells (Volland et al., 2015). This process represents a heavy metabolic load on the RPE, which it must sustain throughout the lifetime of the animal. Defects or inefficiencies in this process can lead to the generation of indigestible material that aggregates as lipofuscin and sub-RPE deposits, leading to RPE pathogenesis and age-related visual impairment, including age-related macular degeneration (AMD) (Hogan, 1972; Feeney, 1973; Brunk and Terman, 2002; Rakoczy

et al., 2002; Sparrow and Boulton, 2005; Bowes Rickman et al., 2013; Wavre-Shapton et al., 2013). A primary step in understanding the basis of impaired POS phagocytosis is to identify whether it is due to defects in the photoreceptor cells or in the RPE cells. Defects in the RPE cells could impair ingestion (Duncan et al., 2003; Nandrot et al., 2004) or degradation (Rakoczy et al., 2002; Jiang et al., 2015). Likewise, defects in the photoreceptor cells could have the same result, by making the POS disks less palatable (Radu et al., 2011; Esteve-Rudd et al., 2018).

2.2 Results

In this chapter, we provide a detailed description of a pulse-chase assay that can be used to analyze POS phagocytosis, using purified mouse POSs and primary cultures of mouse RPE cells. With this assay, and employing different permutations of mutant and control photoreceptor and RPE cells, it is possible to isolate the cause of the mutant phenotype.

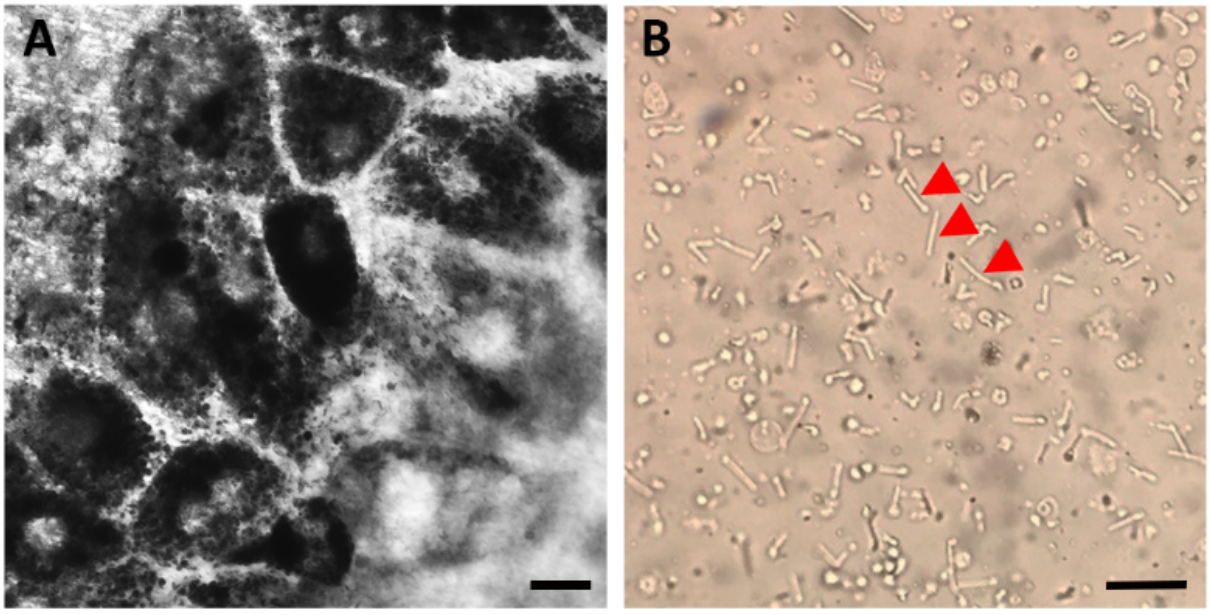

Figure 2.1: Isolation of RPE, and purification of POSs from murine eyes. (A) Primary RPE cells cultured on Transwell inserts for 7 days display RPE-like morphology and pigmentation. (B) POSs purified from mouse retinas have a rod-like structure. A few of the POSs are indicated by red arrows. Scale bars: (A) and (B), 10 μm.

Mouse RPE cells are isolated from eyecups and plated on Transwell inserts to establish primary cultures (Gibbs et al., 2003; Gibbs and Williams, 2003) (Figure 2.1A). The RPE cultures are then pulsed with POSs (Figure 2.1B) purified from mouse retinas for a defined length of time. Following the pulse, excess and unbound POSs are removed by washing, and the cells are either fixed immediately, or given a chase period to internalize bound POSs and degrade ingested phagosomes. Dual-immunofluorescence labeling is then used to distinguish between surface-bound and internalized POSs (Esteve-Rudd et al., 2014) (Figure 2.2). In this assay, we identify POS phagosomes by immunolabeling for opsin, which is abundant in the POS disk membranes, but is not expressed by the RPE. The opsin immunofluorescence signal can be used to quantify the POSs, and a comparison of the signal after the pulse and following the chase provides a measure of the kinetics of POS binding and degradation by the RPE.

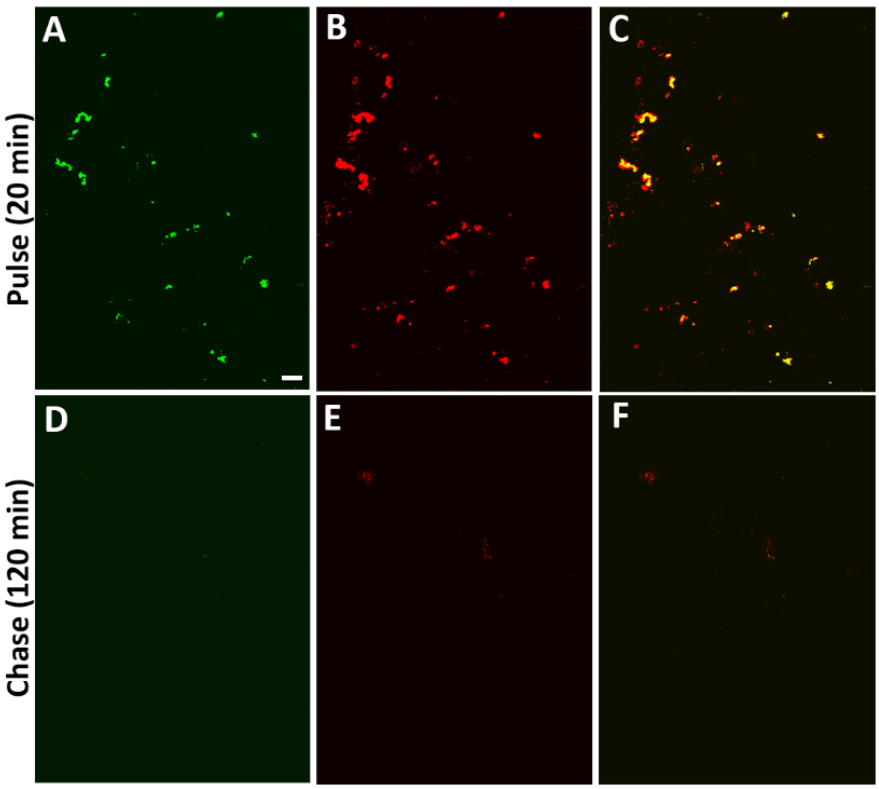

Figure 2.2: Dual-labeling of opsin following a pulse-chase phagocytosis assay. Primary mouse RPE cells were incubated with mouse POSs for 20 min, and fixed immediately (pulse, A-C), or allowed a chase period for 120 min and then fixed (chase, D-F). Opsin labeling was performed

prior to (A, D) and following cell permeabilization (B, E). In the merged panels (C, F), POSs bound to the surface of RPE cells appear yellow due to their exposure to the two different fluorophore-conjugated antibodies (green and red), whereas internalized POSs only appear red. After the pulse, POSs can be seen on both the outside and inside of the RPE cells, while after the chase, the majority of the POSs are on the inside. The reduced number of POSs in the chase compared with the pulse is due to the degradation of POSs by the RPE cells. Scale bar: (A), 10 μm (all panels in figure are of the same magnification).

2.3 Methods and Results

2.3.1 Isolation of Primary Mouse RPE

Mouse pups between the age of postnatal day (P) 10-15 were sacrificed by cervical dislocation. The eyes were enucleated and collected in Medium A (1 ml per eye) consisting of Dulbecco's Modified Eagle Medium (DMEM) with 4.5 g/L glucose, 1X nonessential amino acids (NEAA), and 1 mM sodium pyruvate. The medium was then removed, and the eyes were incubated in a 2% dispase solution (1 ml per 2 eyes) at 37 °C for 45 min. The dispase solution was then removed completely, and the eyes were washed 2 times in Medium B (same as Medium A with 10% FBS, 1X Pen/Strep, and 20 mM HEPES).

Using an upright dissection microscope, the anterior portions of the eyes, including the lens and the iris, were removed by pulling apart the cornea. The resulting eyecups were then collected in Medium A and incubated at 37 °C for 20 min to detach the retina from the RPE layer. Following the removal of the retina, sheets of RPE were gently scraped from the underlying Bruch's membrane and collected in Medium C (same as Medium A with 10% FBS and 1X Pen/Strep). The suspension was centrifuged at 150 x *g* for 1 min at RT, and the cells were then washed 3 times with Medium C. Sheets of RPE were then triturated by gentle pipetting to produce small clusters consisting of 5-10 cells before being plated on Transwell inserts at a concentration 50,000 cells.cm^{-2} in Medium C. Cultures were maintained in a humidified incubator at 37 °C with 5% CO_2 for 3-7 days.

2.3.2 Isolation of Mouse Photoreceptor Outer Segments

Adult mice were dark-adapted overnight before being sacrificed, under dim red light, by cervical dislocation following a brief exposure to isoflurane. The eyeballs were partially pulled out of the eye socket using curved forceps without complete detachment, and an incision was made across the eye, releasing the lens in the process. The retinas were then squeezed out of the eye and collected on ice in a glass homogenizer containing 750 µl Ringer solution (pH 7.4), which consisted of 130 mM NaCl, 3.6 mM KCl, 2.4 mM $MgCl_2$, 1.2 mM $CaCl_2$, 10 mM HEPES, and 0.02 mM EDTA. The POSs were then released by gently homogenizing the retinas with a glass pestle, followed by a brief centrifugation (100 x *g* for 1 min at RT) to pellet large debris. The supernatant was then collected and loaded, using a blunt-ended pipette tip, onto a non-continuous (8/10/15%) OptiPrep gradient inside a 4-ml polycarbonate Sorvall tube. The gradients were then centrifuged at 12,000 x *g* for 20 min at 4 °C using a swinging-bucket rotor with the following settings: Acceleration = 4, Deceleration = 0. The POSs were collected from the 10/15% interface of the gradient, as they were easily identifiable due to the pink/orange hue, and diluted with Ringer solution at 1:3 (v/v) ratio before being centrifuged at 10,000 x *g* for 10 min at 4 °C. The POS were resuspended in DMEM and their density was determined by counting them on a hemocytometer.

2.3.3 Phagocytosis of Photoreceptor Outer Segments

FBS was added to POSs suspended in DMEM at a final concentration of 10%, and mixed gently by pipetting. Mouse primary RPE cells cultured on Transwell inserts were incubated with the POSs (1-5 x 10^7 POSs/ml) in 100-µl of DMEM with FBS at 37 °C for 20 min. After this incubation period, the POS suspension was removed from the Transwell inserts, and the cells were washed 3 times with DPBS-CM to remove unbound POSs. Some inserts were fixed with 4% formaldehyde for 10 min at RT, while others were returned to the 37 °C incubator

for 2 h with fresh Medium C; the former constitute the pulse while the latter consist the chase. Following fixation, the cells were incubated with blocking buffer (1% BSA in DPBS-CM) for 30 min at RT. To label surface-bound POSs, the cells were incubated with mouse-anti-opsin (4D2) diluted in blocking buffer for 10 min at RT, washed 3x5 min with blocking buffer, and labeled with Alexa Fluor 488 nm-conjugated goat-anti-mouse secondary antibodies for 30 min at RT. The cells were then washed 3x5 min with blocking buffer, permeabilized with 50% ethanol in DPBS-CM for 5 min at RT, and washed 3x5 min with blocking buffer.

To label all POSs, including internalized POS-derived phagosomes, the cells were incubated with 4D2 mouse-anti-opsin, and labeled with Alexa Fluor 594 nm-conjugated goat-anti-mouse, each for 1 h at RT. The Transwell membranes of the inserts were excised using a surgical blade and mounted on microscopy slides using Fluoro-Gel with DAPI. The POSs were imaged on an Olympus confocal microscope (IX 81) using a 60x oil objective.

Chapter 3

Live-Cell Imaging of Phagosome Motility in Primary Mouse RPE Cells

3.1 Introduction

The retinal pigment epithelium (RPE) is a post-mitotic epithelial monolayer of cuboidal cells situated between the light-sensitive photoreceptors and the choriocapillaris (Bok, 1993). The RPE performs numerous functions vital to the health of photoreceptors and thus to healthy vision. These functions include recycling of retinoids during the visual cycle, transport of nutrients from the blood to the photoreceptors, and secretion of growth factors, such as vascular endothelial growth factor (VEGF) and pigment epithelial-derived factor (PEDF) (Strauss, 2005). One of the most critical functions performed by the RPE is the phagocytosis of photoreceptor outer segment (POS) tips (Young and Bok, 1969), an event that occurs on a daily cycle (LaVail, 1976).

The RPE is a professional phagocyte, internalizing and degrading approximately 10% of each photoreceptor outer segment on a daily basis. Phagosomes containing POS membranes move from the apical region of the RPE towards the basal region (Herman and Steinberg, 1982b; Gibbs et al., 2003), fusing with degradative organelles such as endosomes and lysosomes along the way (Bosch et al., 1993a; Wavre-Shapton et al., 2014). By-products that are not completely degraded tend to form constituents of aggregates, such as lipofuscin or sub-RPE deposits, common features associated with macular degeneration (Brunk and Terman, 2002). Given the movement of phagosomes from the apical region, their motility is closely related with their degradation. In an early study, it was shown that colchicine, which disrupts microtubules, inhibited the translocation of phagosomes from the apical region (Herman and Steinberg, 1982b). More recently, the importance of actin-based motility was demonstrated in mice lacking MYO7A, an unconventional myosin. In those mice, phagosomes were retained longer in the apical region of the RPE, and were degraded more slowly (Gibbs et al., 2003). In

the present report, we describe the use of live-cell imaging, using spinning disk confocal microscopy, to study the intracellular trafficking of POS-containing phagosomes within primary mouse RPE cells.

3.2 Results

Figure 3A depicts a schematic diagram of the protocol used for live-cell imaging. We used C57BL/6J mice for both the RPE cells and the POSs. Cultured RPE cells were incubated with 1-5 x10^6 fluorescently-labeled POSs in growth medium with 10 mM HEPES for 20 min at 37 ºC, washed extensively with growth medium, and then immediately imaged for a maximum of 1 h, using an Ultraview Spinning Disk Confocal Microscope system with a Zeiss Axiovert photomicroscope, including an environment chamber. Movies were acquired at 3 frames per second with the Volocity software (PerkinElmer), using a 63x oil immersion objective and a Hamamatsu EM-CCD camera (see Movie S1). Trajectories of phagosomes were analyzed using the Volocity software (Figure 3B).

Not all phagosomes were moving at a given time, however, the paths of those that were moving typically followed relatively straight lines, with back and forth movements along these lines. This motility is consistent with movements along microtubules, as cargos of plus- and minus-end directed microtubule motors. The paths can be analyzed to assess a variety of phagosome motility parameters. Speed and distance traveled represent two basic parameters. From analysis of the paths of phagosomes that traveled at least 3 μm in a 24-second interval, we found a mean speed of 1.2±0.1 μm/s and a mean total distance traveled of 11.3±1.9 μm, during the 24-second interval. This speed is typical of transport by microtubule motors (Okada et al., 1995). Transport along actin filaments by myosins is typically many fold slower (Boal, 2012), suggesting that the observed motility was dominated by the microtubule motors, kinesin and dynein.

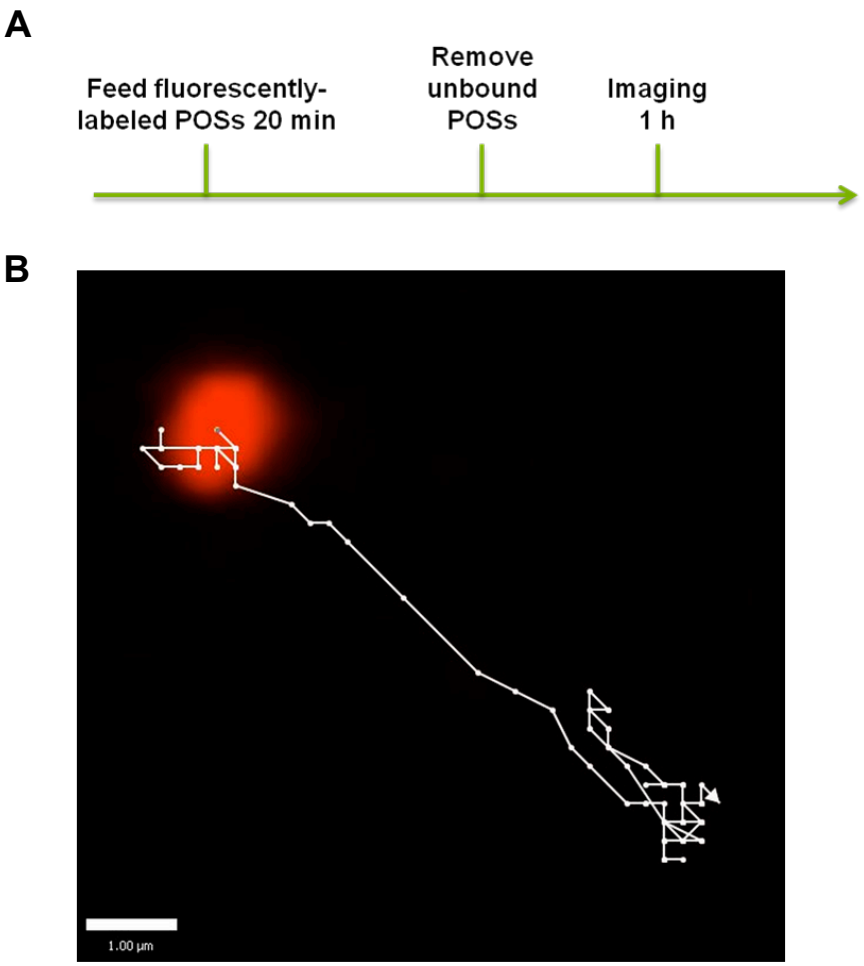

Figure 3: Method for monitoring phagocytosis of photoreceptor outer segments in live RPE. (A) Scheme of phagocytosis assay for live cultures of RPE. (B) Magnified view of a fluorescently-labeled phagosome and its trajectory inside a live RPE cell. Scale Bar: (B), 1 µm.

3.3 Materials and Methods

3.3.1 Isolation and Culture of Primary Mouse RPE

Primary mouse RPE were isolated as previously described (Gibbs et al. 2003). Intact eyes were enucleated from P10-P15 mice and washed 3-4 times by inversion with growth medium (Dulbecco's modified Eagle's medium (DMEM) with 4.5 g/L glucose, L-glutamine, and sodium pyruvate). The eyes were then incubated in a 2% dispase solution for 45 min at 37 ºC. Following removal of the enzyme solution, the eyes were washed 3 times with growth medium containing 10% fetal bovine serum (FBS) and 20 mM HEPES. The eyes were dissected into

eyecups by making an incision along the ora serrata to remove the cornea, iris, lens, and ciliary body. Eyecups were then incubated in growth medium for 20 min at 37 ºC, as this facilitates the separation of the RPE from the retina and Bruch's membrane. Sheets of RPE were gently scraped from Bruch's membrane and collected in growth medium with 10% FBS. The sheets were then washed 3 times with growth medium and twice with calcium- and magnesium-free Hank's Balanced Salt Solution (HBSS). The cells were then briefly and gently triturated and plated on Lab-Tek chambered coverglass. Live-cell imaging experiments were carried out on 3-7 day old cultures.

3.3.2 Isolation and Labeling of Mouse POSs

Mouse POSs were isolated as previously described (Gibbs et al. 2003). Mouse retinas were collected under dim red light and homogenized in Ringer's solution (130 mM NaCl, 3.6 mM KCl, 2.4 mM $MgCl_2$, 1.2 mM $CaCl_2$, 10 mM HEPES, and 0.02 mM EDTA). The homogenate was cleared by centrifugation for 30 s at 100 *g*, and then the supernatant was layered on top of a discontinuous Optiprep 8%-10%-15% step gradient in Ringer's solution and spun at 12,000 *g* for 20 min at 4 ºC. POSs were collected at the 10%/15% interface and diluted 3 times with Ringer's solution. POSs were then pelleted by spinning the solution at 10,300 *g* for 10 min at 4 ºC. The POSs were then labeled by incubation with 0.1 mg Texas Red-X, succinimidyl ester or 5% (v/v) Alexa Fluor 488 carboxylic acid, succinimidyl ester, mixed isomers in 1 mL 0.1M $NaHCO_3$, pH 8.3 for 1 h at 4 ºC. POSs were then washed with Ringer's solution, resuspended in RPE growth medium, and counted using a haemocytometer to determine the yield.

3.4 Discussion

Fluorescently-labeled POS phagosomes can be monitored in live RPE cells, using spinning disk confocal microscopy. Their motility can be determined by tracking their trajectories, thus providing a sensitive, real-time measurement of a critical parameter of RPE health – one, which we are finding in other studies, feeds directly into the efficiency of

phagosome degradation, and the propensity for the accumulation of debris and consequent activation of downstream events, such as inflammation and oxidative stress.

Chapter 4

Defective Phagosome Motility and Degradation in Cell Non-Autonomous RPE Pathogenesis of a Dominant Macular Degeneration

4.1 Introduction

Autosomal dominant Stargardt macular dystrophy 3 (STGD3) results in early loss of central vision from photoreceptor degeneration. It is caused by single allelic mutations in the *elongation of very long-chain fatty acids 4* (*ELOVL4*) gene (Edwards et al., 2001; Zhang et al., 2001). This gene encodes a transmembrane enzyme that catalyzes the condensation reaction in the elongation of very long chain saturated (VLC-FA) and polyunsaturated fatty acids (VLC-PUFA) greater than 26 carbons (Agbaga et al., 2008). STGD3-associated mutations generate truncated forms of the ELOVL4 protein that lack the endoplasmic reticulum (ER) retention signal present at the C-terminus of the protein (Bernstein et al., 2001; Zhang et al., 2001; Maugeri et al., 2004).

Studies have attempted to identify how this defect leads to the death of the photoreceptor cells in dominant Stargardt disease. Cell culture studies suggested that mutant ELOVL4 interacts with wild-type (WT) ELOVL4, such that the WT protein is mislocalized from the ER, and lacks enzymatic activity (Logan et al., 2013). However, in frog and mammalian photoreceptors that expressed mutant and WT *ELOVL4*, the WT ELOVL4 protein appeared to be localized normally (Grayson and Molday, 2005; Sommer et al., 2011; Agbaga et al., 2014; Kuny et al., 2015). Moreover, the retinas of transgenic mice, expressing mutant human *ELOVL4,* the TG(mut*ELOVL4*)2 line, which closely resembles human STGD3 (Karan et al., 2005), contain WT levels of VLC-PUFA, indicating that the mutant ELOVL4 does not affect the function of the WT protein (Mandal et al., 2014).

Mouse models that include the knock-in of a mutant *Elovl4*, to generate *Elovl4*$^{+/mut}$, as well as the TG(mut*ELOVL4*)2 mice, show RPE pathology preceding photoreceptor cell death (Karan et al., 2005; Vasireddy et al., 2006; Vasireddy et al., 2009; Kuny et al., 2015). As in other forms of macular degeneration, including STGD1 (Weng et al., 1999) and age-related macular degeneration (AMD) (Ambati et al., 2013), RPE pathology in STGD3 appears to be a significant, if not the main contributor to photoreceptor cell degeneration (Karan et al., 2005; Kuny et al., 2015).

Cell non-autonomous toxicity has widespread importance for neurodegenerations, although the underlying cellular mechanisms are largely unknown. They have been reported to contribute to diseases, such as Alzheimer's, Parkinson's, and Huntington's Disease, as well as Amyotrophic Lateral Sclerosis, in which neuronal damage is promoted by mutant gene expression in neighboring cell types (Ilieva et al., 2009). In the case of retinal degeneration in STGD3, the cell non-autonomous pathway appears to be unusually complex, with the involvement of an additional step. The RPE does not express *ELOVL4* (Agbaga et al., 2008; Mandal et al., 2014), suggesting that its contribution to photoreceptor degeneration in STGD3 stems from RPE pathogenesis that was originally introduced from the photoreceptors themselves.

Here, we explored the first cell non-autonomous step in STGD3: how mutant ELOVL4 in the photoreceptors may lead to RPE pathology. We focused on a major function of the RPE, involving the phagocytosis of the distal POS disks (Young and Bok, 1969; Williams and Fisher, 1987), which, in mammals, amounts to 10% of the POS disks each day (Young, 1967). Each RPE cell serves many photoreceptors (more than 200 in mouse) (Volland et al., 2015), so that disk membrane degradation represents a heavy metabolic load. We demonstrate that POSs of *ELOVL4*-mutant photoreceptors contain mislocalized mutant ELOVL4 protein, and that phagosomes of these POSs are degraded more slowly by the RPE. We present evidence that

the presence of ELOVL4 protein in phagosomes affects their association with RAB7A and their recruitment of cytoplasmic dynein, resulting in impaired motility, which underlies their retarded degradation. Our findings have major implications for understanding phagocytosis by demonstrating the importance of the content of ingested material on phagosome motility, and by indicating that impaired phagosome motility, in an otherwise normal cell, appears sufficient to retard degradation.

4.2 Results

4.2.1 Photoreceptor Degeneration and Localization of WT and Mutant ELOVL4

Our line of transgenic mice, expressing mutant human *ELOVL4*, originates from the TG(mut*ELOVL4*)2 line (referred to as simply TG2 hereafter), as described previously (Karan et al., 2005). At 21 days old (P21), no photoreceptor loss was evident, but by P70 it is quite significant (Figure 4.1A-D). Quantification of the number of photoreceptor nuclei in the outer nuclear layer showed that at P45 and at P70, ~20% and ~50%, respectively, of the photoreceptors had been lost in the TG2 retinas (Figure 4.1E).

By qPCR, we determined the expression of the mutant transgene to be three times that of WT *Elovl4* in the TG2 line. Using an antibody that was raised against an ELOVL4 N-terminal antigen, and appears to label both WT and mutant ELOVL4 (Figure 4.2), we found that the POSs were labeled in TG2 but not in WT retinal sections (Figure 4.1F), indicating that the mutant ELOVL4 protein is dislocalized to the outer segment.

To investigate mutant ELOVL4 localization further, we generated a plasmid construct containing a FLAG-tagged cDNA of human *ELOVL4* with the same 5-bp deletion as in the TG2 transgene (and as observed in STGD3 patients). The construct was electroporated into the photoreceptors of WT mice. FLAG antibody labeling showed the presence of the mutant ELOVL4 in the POSs. By contrast, electroporation of a construct containing FLAG-tagged WT

ELOVL4 resulted in inner segment but not outer segment labeling (Figure 4.1H). These results are consonant with findings from transgenic frog retinas (Agbaga et al., 2014).

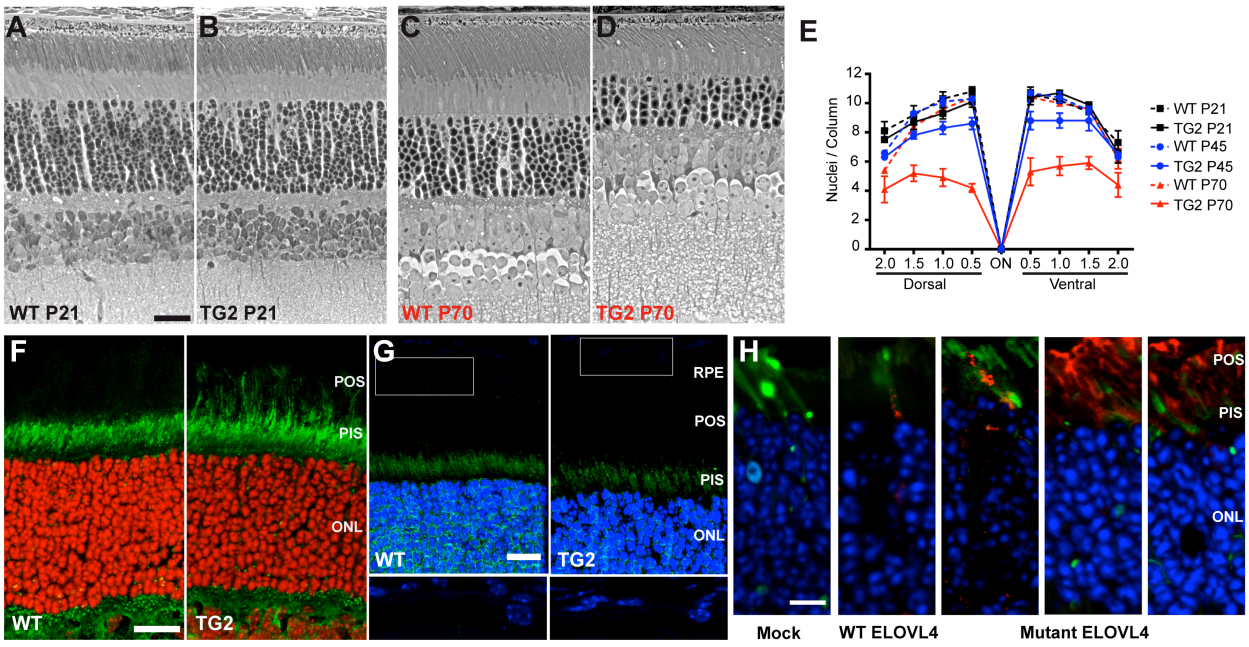

Figure 4.1: Retinal degeneration and localization of ELOVL4. (A-D) Phase-contrast images of semi-thin sections from P21 or P70 WT (A, C) and TG2 (B, D) retinas. Mutant TG2 retinas were similar in overall morphology to WT retinas at P21, but the photoreceptor cells have undergone markedly significant degeneration by P70, as can be observed by the loss of photoreceptor nuclei in the ONL. (E) Graph of the number of photoreceptor nuclei per column in the ONL, quantified at 0.5-mm intervals from the optic nerve. Some photoreceptor cell loss in TG2 retinas was observed at P45; by P70 it was more severe. (F, G) Retinal sections from P21 WT and TG2 mice immunolabeled with antibodies against the N-terminal (F) or C-terminal (G) region of ELOVL4 (green). The N-terminal antibody recognizes both WT and mutant ELOVL4, but the the C-terminal antibody recognizes only WT ELOVL4. POSs are labeled in the TG2 retinal section by the former (F), but not the latter (G). Nuclei were counterstained with DAPI (shown as red or blue). (H) Retinal sections from mice whose photoreceptors were electroporated with Dendra2 (green) and FLAG-tagged WT or mutant human ELOVL4 plasmids. The sections were labeled with a FLAG antibody (red). Mock retinas were electroporated with Dendra2 only. The WT FLAG-ELOVL4 protein is localized primarily to the PIS. The mutant FLAG-ELOVL4 protein was observed mostly in the POS, with some presence in the PIS (mutant ELOVL4 still contains the N-terminal ER localization signal, but it has lost the C-terminal ER retention signal). POS, photoreceptor outer segment; PIS, photoreceptor inner segment; ONL, outer nuclear layer; OPL, outer plexiform layer; ON, optic nerve; Ad5, Adenovirus Type 5; GFP, green fluorescent protein. Scale bars represent 10 μm in (A), (F) and (H), and 15 μm in (C).

Labeling of retinal sections with an ELOVL4 antibody raised against a C-terminal epitope, which does not recognize the truncated mutant protein, also indicated that the WT protein was absent from the POSs of TG2 retinas. Labeling of the WT protein was comparable between TG2 and WT retinas, in agreement with a previous report (Mandal et al., 2014). It was present mainly in the inner segment, but also with suggestion of label in the outer nuclear and outer plexiform layers (Figure 4.1G), as reported previously (Grayson and Molday, 2005; Agbaga et al., 2008; Kuny et al., 2015). These results indicate that the localization of the TG2 protein to the POS does not significantly affect the localization of the WT protein.

WT ELOVL4 is not detectable in the RPE (Figure 4.1G). However, a consequence of mutant ELOVL4 dislocalization to the POSs is that phagosomes within the TG2 RPE should contain mutant ELOVL4. These phagosomes could be detected with the N-terminal ELOVL4 antibody (Figure 4.3).

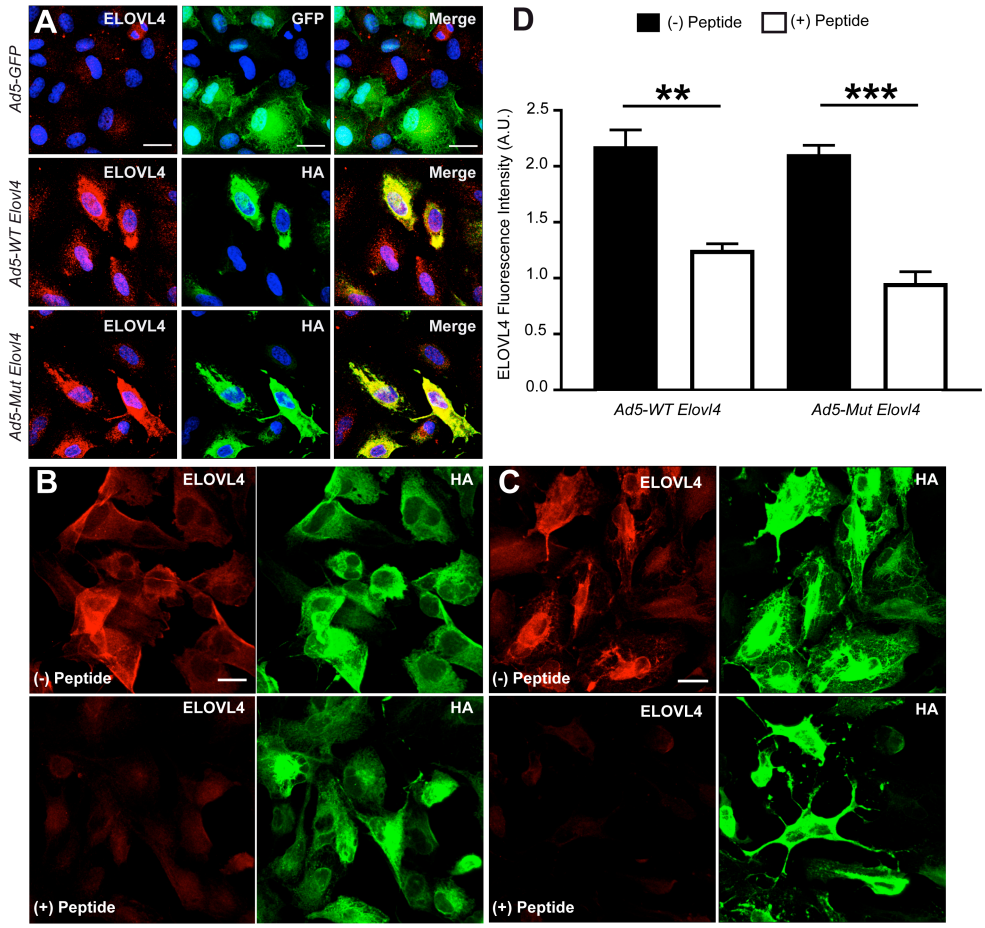

Figure 4.2: Detection of WT and Mutant ELOVL4 by N-terminal ELOVL4 antibody. (A) ARPE-19 cells were transduced with Adenovirus Type 5 containing cDNA for GFP, HA-tagged WT or HA-tagged mutant (5-bp deletion) mouse *Elovl4*, and then labeled with the same N-terminal ELOVL4 antibody, used to immunolabel retinal sections, as in Figure 4.1F. The anti-ELOVL4 shows relatively weak labeling in cells that were not transduced or transduced with GFP (top row), and very bright labeling in cells that were transduced with either HA-WT-ELOVL4 (middle row) or HA-mutant-ELOVL4 (bottom row). Moreover, immunolabeling by an HA tag antibody colocalizes with labeling by the ELOVL4 antibody. (B, C) To test specificity of the anti-ELOVL4, the experiment above was repeated and the immunolabeling for WT (B) and mutant (C) ELOVL4 was performed in the presence or absence of the immunizing peptide. Following 1 h preincubation with the immunizing peptide (25:1 ratio of peptide to antibody), the ELOVL4 immunolabel is significantly dimmer, even in cells that are expressing high amounts of either WT or mutant ELOVL4, as indicated by the HA immunolabel. (D) Quantification of mean ELOVL4 fluorescence intensity from three randomly-selected regions of ARPE19 cultures transduced with either WT or mutant ELOVL4 and immunolabeled with anti-ELOVL4 in the presence or absence of the immunizing peptide. The presence of the immunizing peptide reduces the ELOVL4 immunolabel intensity by approximately 50% in cells transduced with either WT or mutant *Elovl4*. Scale bars in (A-C) represent 20 µm. The error bars in (D) represent the +/- S.E.M.

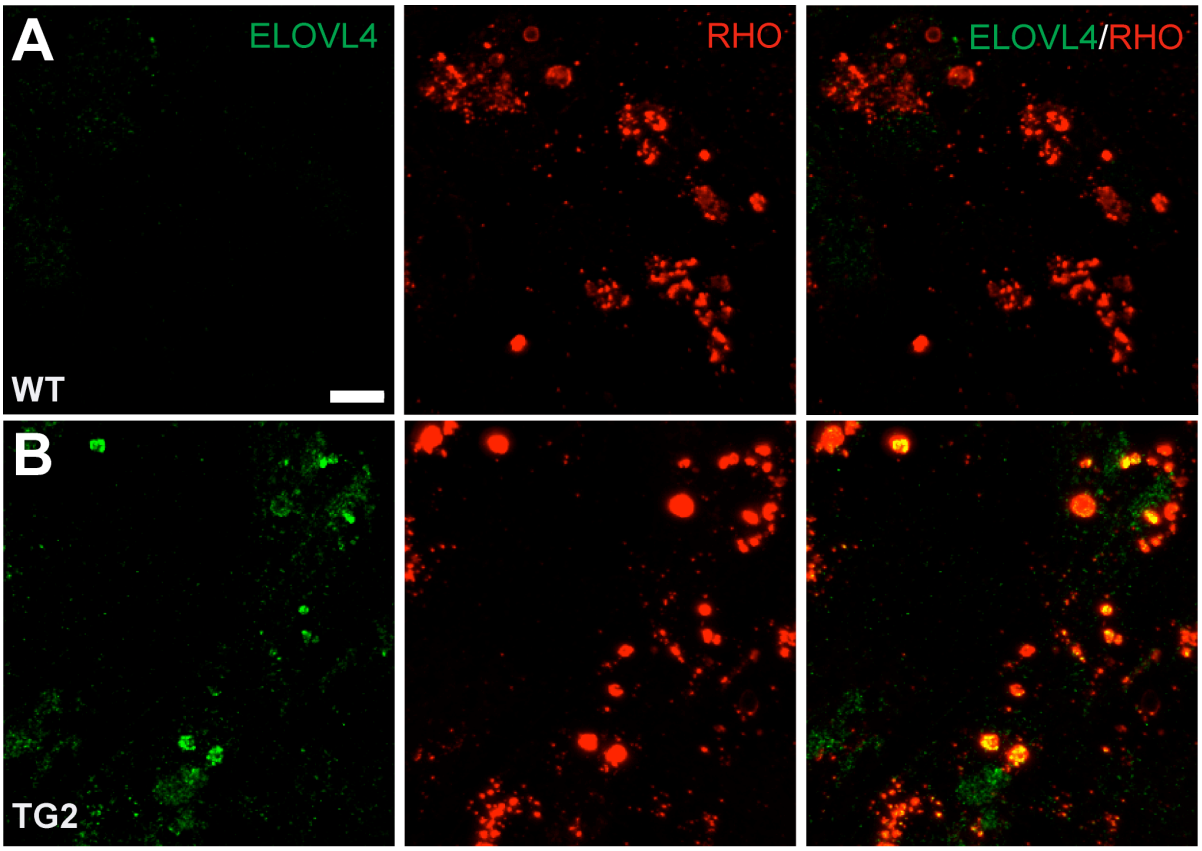

Figure 4.3: Detection of ELOVL4 in TG2 phagosomes. Immunolabeling of WT primary mouse RPE cells fed WT (A) or TG2 (B) POSs, with antibodies against the N-terminal region of ELOVL4 (green) or against RHO (red). ELOVL4 is detected in RHO-positive phagosomes from TG2 POSs, but not from WT POSs. Scale bar represents 10 μm.

4.2.2 Delayed Degradation of Phagosomes from TG2 Outer Segments

By electron microscopy, we observed previously that the RPE of TG2 retinas accumulate membranous debris and lipid droplets over time (Karan et al., 2005), suggestive of a defect in POS degradation. To test whether such a defect underlies the pathology of TG2 retinas, we analyzed the rate of degradation in young mouse retinas, showing no pathology or degeneration. First, we imaged phagosomes in the RPE of P21 mice at 0.5 h post light onset, the peak of phagocytosis in mice, and at 3 h after light onset, when the number of phagosomes in the RPE of WT retinas has been significantly reduced due to degradation (Figure 4.4A-D) (Gibbs et al., 2003; Sethna et al., 2016). The number of POS phagosomes in TG2 retinas was

comparable to that in WT retinas at 0.5 h, indicating that the rate and timing of ingestion appear to be normal. However, at 3 h after light onset, the number is significantly greater in TG2 retinas, indicating only a minor decrease from 0.5 h after light onset (Figure 4.4E), and suggesting either defective degradation or additional ingestion. Given that the POS length was unchanged between the two time-points, our results support the former.

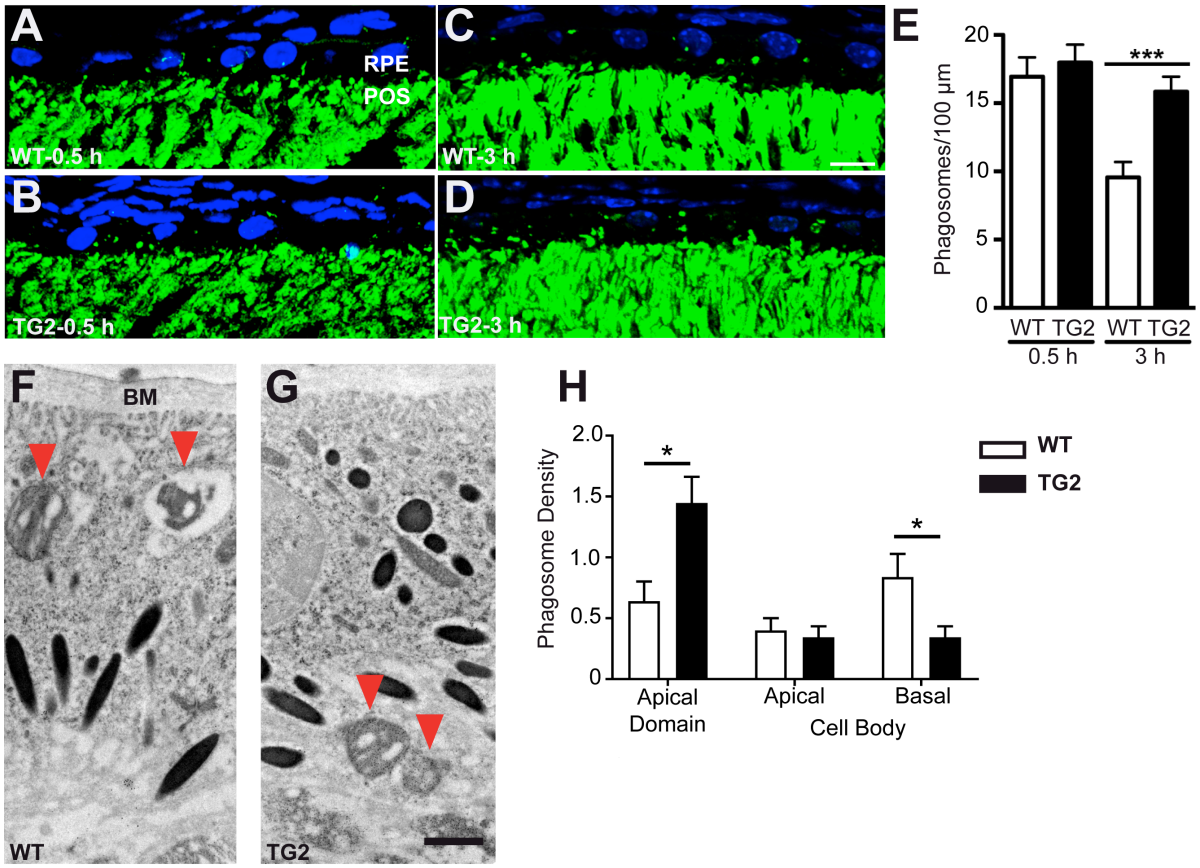

Figure 4.4: Degradation of POS phagosomes in WT and mutant mouse RPE in vivo. (A-D) Immunofluorescence images of RHO labeling (green) in WT (A, C) and TG2 (B, D) retinal sections from P21 mice sacrificed 0.5 h (A, B) and 3 h (C, D) post light onset. POS phagosomes can be seen as green particles in the RPE layer. The nuclei are counterstained with DAPI (blue). (E) Quantification of POS phagosomes per 100 µm of the RPE layer in WT and TG2 retinas showed no significant difference at 0.5 h post light onset, but significantly more POS phagosomes remained in TG2 RPE at 3 h post light onset, indicating impaired phagosome degradation. (F, G) ImmunoEMs of WT (F) and TG2 (G) retinas from P28 mice showing POS phagosomes (immunogold-labeled with RHO antibodies, and indicated by red arrowheads) inside the RPE at 1.5 h post light onset. (H) Quantification of phagosome density (mean number of phagosomes per 55 μm^2 of sectioned RPE) in different regions of the RPE. Bar graph shows data from the apical and cell body domains of the RPE; these domains border each other at the level of the junctional complexes. The cell body domain was divided further into apical and basal

halves. The data show that more TG2 than WT POS phagosomes were in the apical domain, while more WT than TG2 phagosomes were in the basal half of the cell body. BM, Bruch's membrane. Scale bars in (C) and (G) represent 10 μm and 1 μm, respectively. Error bars in (E) and (H) represent +/-S.E.M.

We also examined POS phagosome degradation, using an in vitro pulse-chase assay with primary cultures of RPE cells from WT mice, an approach that enabled us to examine acute effects in the RPE due to the presence of mutant ELOVL4 in the POSs. We purified POSs from the retinas of WT and TG2 littermates (Figure 4.5A), fed them to the WT primary mouse RPE cells for 10 min, and washed the cells extensively to remove unbound POSs. The cells were then fixed either immediately (pulse), or after an additional 2-h period (chase). Rod opsin (RHO) double immunolabeling (before and after cell permeabilization) was then performed to differentiate between POSs bound to the surface of the RPE and POSs ingested by the RPE (Figure 4.5B). The number of surface-bound POSs was not significantly different between WT and TG2 after the pulse and chase period (Figure 4.5C). Furthermore, the number of ingested POSs was also not significantly different after the pulse (Figure 4.5D, left). Thus, the binding and ingestion of TG2 POSs appeared to be normal. However, a significant difference in the number of POSs was observed after the 2-h chase period, at which point, the RPE cells fed WT POSs had degraded approximately 40% of their ingested POS phagosomes, whereas the RPE cells fed TG2 POSs showed no significant decrease in their POS phagosome content (Figure 4.5D, right). This result indicates that WT primary mouse RPE cells do not degrade phagosomes originating from TG2 POSs as efficiently as phagosomes from WT POSs.

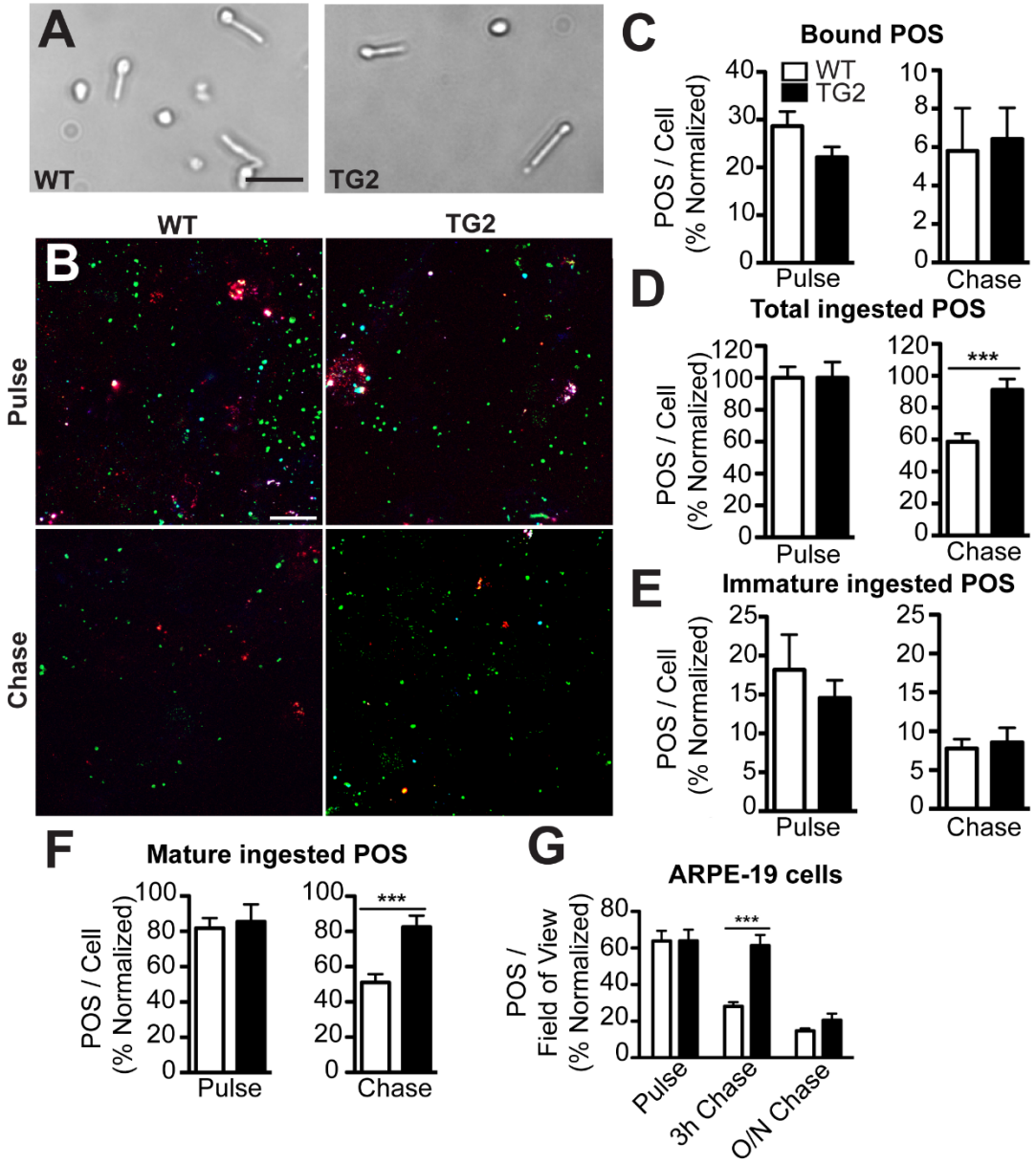

Figure 4.5: Impaired degradation of mutant ELOVL4 POSs by WT RPE cultures. (A) Brightfield images of WT and TG2 POSs isolated from respective retinas. (B) RHO labeling of WT primary mouse RPE cells, fed either WT or TG2 POSs, immediately following the pulse or following a chase period. The labeling was performed before and after cell permeabilization to distinguish between surface-bound POSs (white or red) and internalized phagosomes. Additionally, the immature phagosomes (cyan) were identified by labeling with a RHO mAb that binds the C-terminus (1D4) and RHO pAb01, while the mature phagosomes (green) were identified by labeling with RHO pAb01 only. (C-F) Quantification of the POSs. POSs fed to primary mouse RPE and labeled with RHO pAb01, showed that there was no significant difference between the number of bound POSs after the pulse and chase (C), but there were more total ingested TG2 POSs following the chase compared with WT POSs (D). When the total POSs were further defined as immature (labeled with mAb1D4) vs mature (labeled with pAb01 but not mAb1D4), the number of immature ingested POSs was not found to be statistically significant between WT and TG2 POSs (E), whereas the cells fed TG2 POSs had more mature ingested POSs following the chase (F). (G) The impaired POS degradation phenotype was also observed in human

ARPE-19 cells, which after a 3-h chase period, had more (bound + ingested) TG2 POSs than ARPE-19 cells fed WT POSs. Scale bars in (A) and (B) represent 20 μm and 10 μm, respectively. Error bars in (C-G) represent +/- S.E.M.

Newly-formed POS phagosomes are labeled by antibodies against both the N- and C-termini of RHO. However, RHO mAb1D4, which recognizes a C-terminal epitope, is lost quickly as phagosomes begin to mature, so that it is a specific marker for immature phagosomes (Esteve-Rudd et al., 2014; Wavre-Shapton et al., 2014). Using mAb1D4, our results showed that the number of immature WT and TG2 phagosomes was similar (Figure 4.5E). The slower degradation rate was evident only with TG2 phagosomes that were more mature (Figure 4.5F), indicating that initial phagosome maturation proceeds normally.

We also tested whether this phenotype could be replicated in human RPE cells using the ARPE-19 immortalized cell line. ARPE-19 cells were challenged with either WT or TG2 POSs for 4 h, washed extensively, and fixed immediately or after a 3-h or 16-h chase period. ARPE-19 cells showed a decrease in phagosomes between the pulse and 3-h chase period when fed WT POSs. In contrast, the phagosome content was not significantly different between the pulse and 3-h chase period when the cells were fed TG2 POSs (Figure 4.5G). This result confirms that the delay in degradation of TG2 phagosomes, observed in mouse primary RPE cells, can be phenocopied in these human RPE cells. Interestingly, the numbers of phagosomes in ARPE-19 cells fed WT and TG2 POSs were similar after the 16-h chase period, indicating that the degradation of phagosomes from TG2 POSs is not completely inhibited, but occurs at a slower rate than that of phagosomes from WT POSs.

4.2.3 TG2 POS Phagosome Trafficking

Phagosome maturation and degradation is associated with an apical-to-basal migration through the RPE (Herman and Steinberg, 1982b). In previous studies, we have found that POS

phagosome degradation is affected by molecular motor function in the RPE. Mutations in the actin-based motor, myosin-7a (Gibbs et al., 2003), and the microtubule-based motor, kinesin-1 (Jiang et al., 2015), lead to impaired POS phagosome motility, slower basal migration, and less efficient degradation by the RPE. We therefore tested whether impaired phagosome motility and migration might be a contributor to the delayed degradation of TG2 POS phagosomes.

Using electron microscopy to gauge the distribution of phagosomes in the RPE of WT and TG2 retinas, we found that at 1.5 h after light onset, the majority of TG2 phagosomes were in the apical region of the RPE, while significantly more WT phagosomes were localized basally in the RPE, near Bruch's membrane (Figure 4.4F-H). These results suggest that TG2 phagosomes progress more slowly along the apical-basal axis of the RPE, thereby resulting in their delayed degradation.

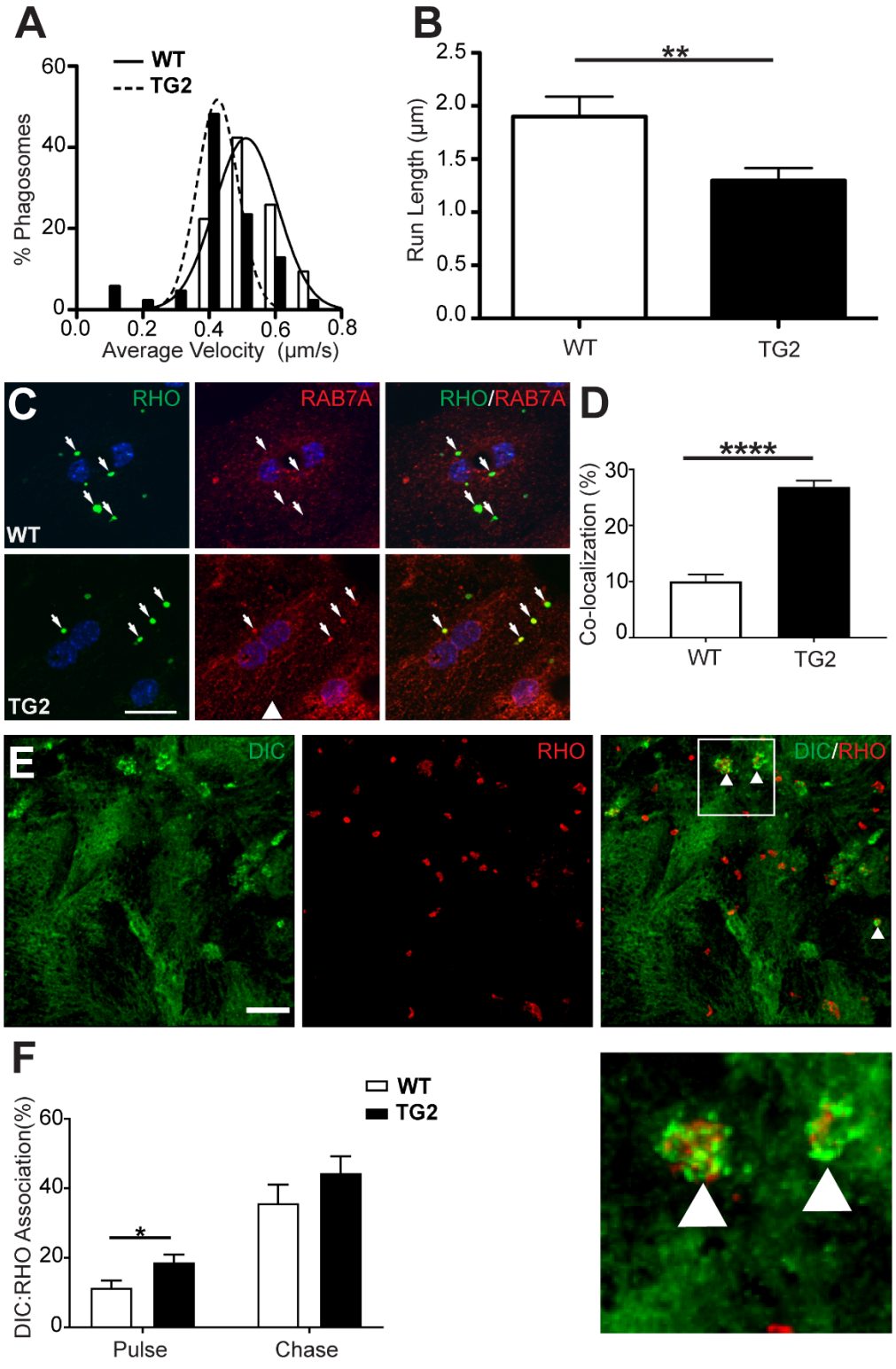

Figure 4.6: Impaired motility of TG2 phagosomes in WT primary mouse RPE cells. (A, B) Live-cell analysis of the tracks of phagosomes (85 per condition), from either WT or TG2 POSs, showed that TG2 phagosomes had a lower mean velocity (A) and shorter mean run length (B)

than their WT counterparts. (C) Immunolabeling of RHO (green) and the endosomal marker RAB7A (red) in WT primary mouse RPE cells, fed either WT or TG2 POSs. (D) Quantification of the number of RHO-positive phagosomes co-localized with RAB7A showed that more phagosomes, derived from TG2 POSs relative to WT POSs, had RAB7A associated with them after a 1-h chase period. (E) Immunofluorescence of cytoplasmic dynein intermediate chain (DIC, green) and RHO (red) in WT primary mouse RPE cells fed POSs after a 1-h chase. White arrowheads in the merged panel indicate phagosomes associated with DIC immunolabeling, shown at higher magnification below. (F) Quantification of the proportion of WT or TG2 POS phagosomes in WT primary mouse RPE cells that were associated with DIC immunolabel, after a 20-min pulse and a 1-h chase. Scale bars in (C) and (E) represent 20 μm and 5 μm, respectively. Error bars in (B, D, and F) represent +/- S.E.M.

Next, we used live-cell imaging of WT and TG2 phagosomes in WT primary RPE cultures. Analysis of phagosome motility tracks (Movie S2) revealed that TG2 phagosomes had a significantly slower average velocity than WT phagosomes. The majority (78%) of WT phagosomes exhibited average velocities between 0.4 and 0.8 μm/s, whereas only 39% of TG2 phagosomes exhibited average velocities in this range (Figure 4.6A). We also analyzed the distance phagosomes traveled between pauses (i.e. instantaneous velocity $\leq$ 0.1 μm/s), and defined this parameter as run length (Figure 4.7). Previously, we had observed that this motility parameter was compromised, together with phagosome degradation rate, in RPE lacking a kinesin-1 light chain (Jiang et al., 2015). Analysis revealed that TG2 phagosomes have a significantly shorter mean run length relative to WT phagosomes (1.3 μm vs. 1.9 μm, respectively) (Figure 4.6B). Taken together, these results suggest that TG2 phagosomes have impaired motility in live RPE cells, as indicated by the lower mean velocity, and by movements that are less productive, as indicated by the shorter run lengths. Note that this defect can be attributed specifically to the POS phagosomes, since the RPE cells were WT, in which the motor protein function, as well as the motility of organelles, such as endolysosomes, should be normal.

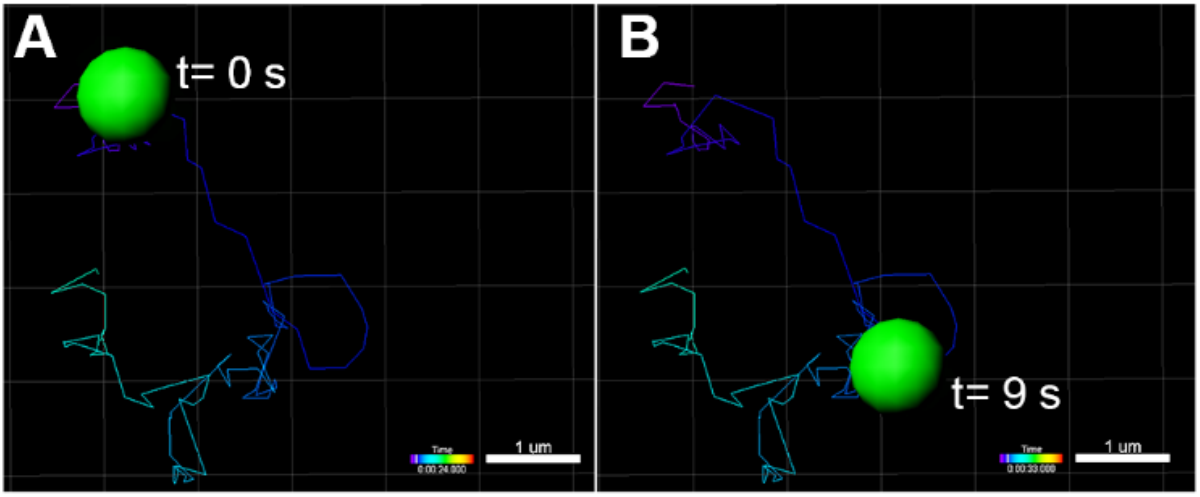

Figure 4.7: Tracking and analysis of phagosome motility. (A, B) Snapshot images from Movie S2 at two different timepoints that are 9 seconds apart. Motility analysis revealed that the phagosome migrated a distance of approximately 3.5 μm during this 9-second interval. Scale bars in (A) and (B) represent 1 μm.

4.2.4 RAB7A and Dynein Motor Association with TG2 POS Phagosomes

We focused on the phagosomes themselves to identify characteristics that might underlie their defective motility. We tested whether the ELOVL4-containing mutant phagosomes showed abnormal association with motor protein linkers. Although we detected no significant difference between WT and TG2 phagosomes in their association with RAB5, there was a marked difference in RAB7A association. WT primary mouse RPE cells were challenged with WT or TG2 POSs for 20 min, and, following a 1-h chase period, were fixed and labeled with antibodies against RHO (mAb4D2) and RAB7A (Figure 4.6C). A co-localization analysis was performed to evaluate the association of WT and TG2 phagosomes (mAb4D2-labeled) with RAB7A. We found that approximately 27% of the TG2 phagosomes, but only 10% of WT phagosomes were also labeled with RAB7A antibodies (Figure 4.6D). These results suggest that phagosomes, derived from TG2 POSs, more readily sequester RAB7A, which may alter

their association with motor proteins, and subsequently interfere with their motility, thereby contributing to the slower rate of degradation.

To test for altered motor protein recruitment to these mutant phagosomes, we evaluated their association with dynein. After feeding WT or TG2 POSs to WT RPE cells, we quantified the proportion of POS phagosomes, labeled with anti-RHO, that were also labeled with antibodies against cytoplasmic dynein intermediate chain (DIC) (Figure 4.6E). The mean proportion of TG2 POS phagosomes that were associated with DIC was higher than that of WT POS phagosomes (Figure 4.6F). These results implicate increased sequestration of RAB7A in abnormal linkage of TG2 phagosomes to the dynein motor protein, which may affect the balance between dynein and kinesin motors, thus contributing to impaired motility of these organelles.

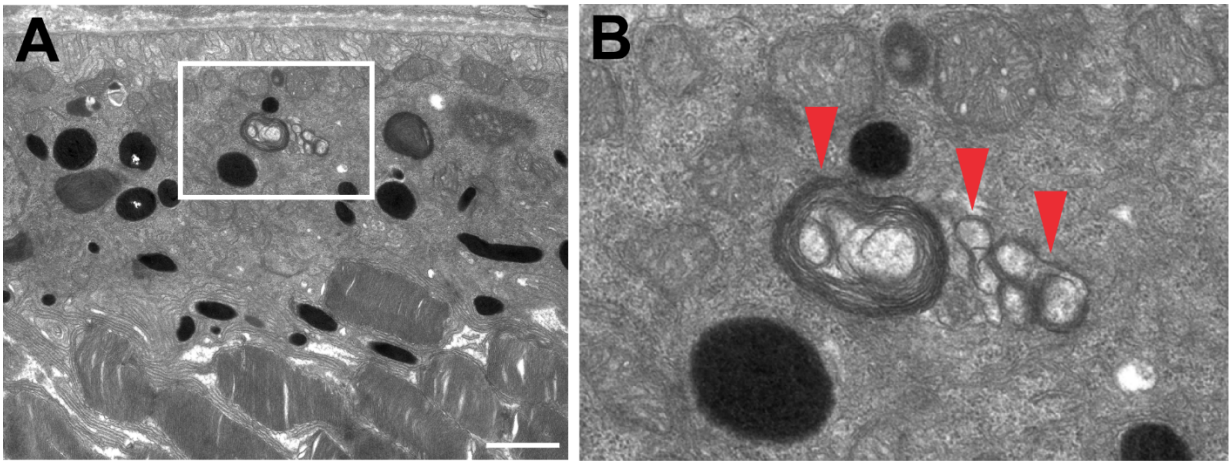

Figure 4.8: Membranous debris in RPE of young TG2 mice. (A) Electron micrograph of retina from a TG2 animal (P21) showing membranous debris in the RPE. (B) An enlarged view of the region delineated by the white box in (A) with red arrows pointing to a cluster of these abnormal membranous structures. The scale bar in (A) represents 0.5 μm.

4.2.5 Pathogenesis and Degeneration

In older TG2 and *Elovl4*$^{+/mut}$ knock-in mice, membranous debris and vacuoles are evident in the RPE (Karan et al., 2005; Vasireddy et al., 2006; Vasireddy et al., 2009; Kuny et al., 2015), consistent with inefficient POS phagosome clearance over time. Here, we examined

the RPE in young TG2 mice, to see if we could identify any early pathological changes. By electron microscopy, we observed clusters of membrane that looked like abnormal phagosomes, in the RPE of P21 TG2 mice (Figure 4.8). At this age, we also noted changes that

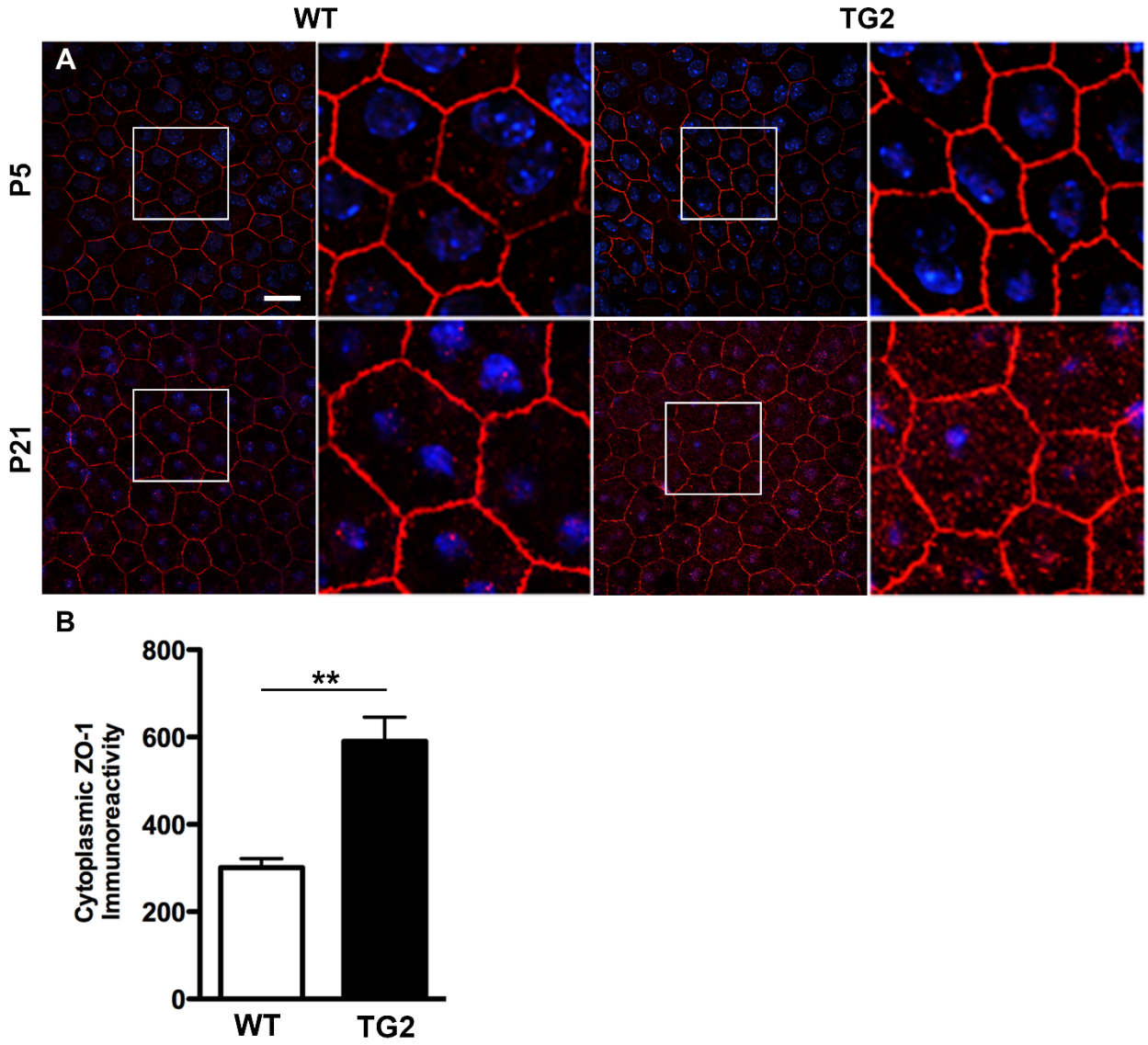

Figure 4.9: Loss of ZO-1 junctional localization in TG2 RPE. (A) Immunolabeling of the tight junctional protein ZO-1 in RPE flatmounts from WT and TG2 animals at P5 and P21. ZO-1 labeling was similar between WT and TG2 animals at P5, whereas significantly more cytoplasmic ZO-1 was observed in TG2 RPE at P21. Enlarged views of regions delineated by white boxes in (A) are to the right of each corresponding panel. (B) Quantification of cytoplasmic ZO-1 immunoreactivity showed significantly more cytoplasmic ZO-1 in the RPE of P21 TG2 animals compared with age-matched WT littermates. The scale bar in (A) represents 10 μm. The error bars in (B) represent the +/- S.E.M.

we suspect are secondary changes, and are indicative of a general decline in RPE health. Some of the tight junction protein, zona occludens-1 (ZO-1), had lost its junctional localization, with an increase in immunoreactivity evident throughout the cytosol of TG2 RPE cells (Figure 4.9). This change is likely to lead to a decrease in epithelial barrier function, due to a breakdown in the intercellular junctions between RPE cells. Second, in older animals (P70), we observed a marked increase in oxidative stress in the RPE in vivo (Figure 4.10). Labeling for the oxidative stress marker, 4-HNE, was also increased in WT primary mouse RPE cells that were incubated with TG2 POSs (Figure 4.11).

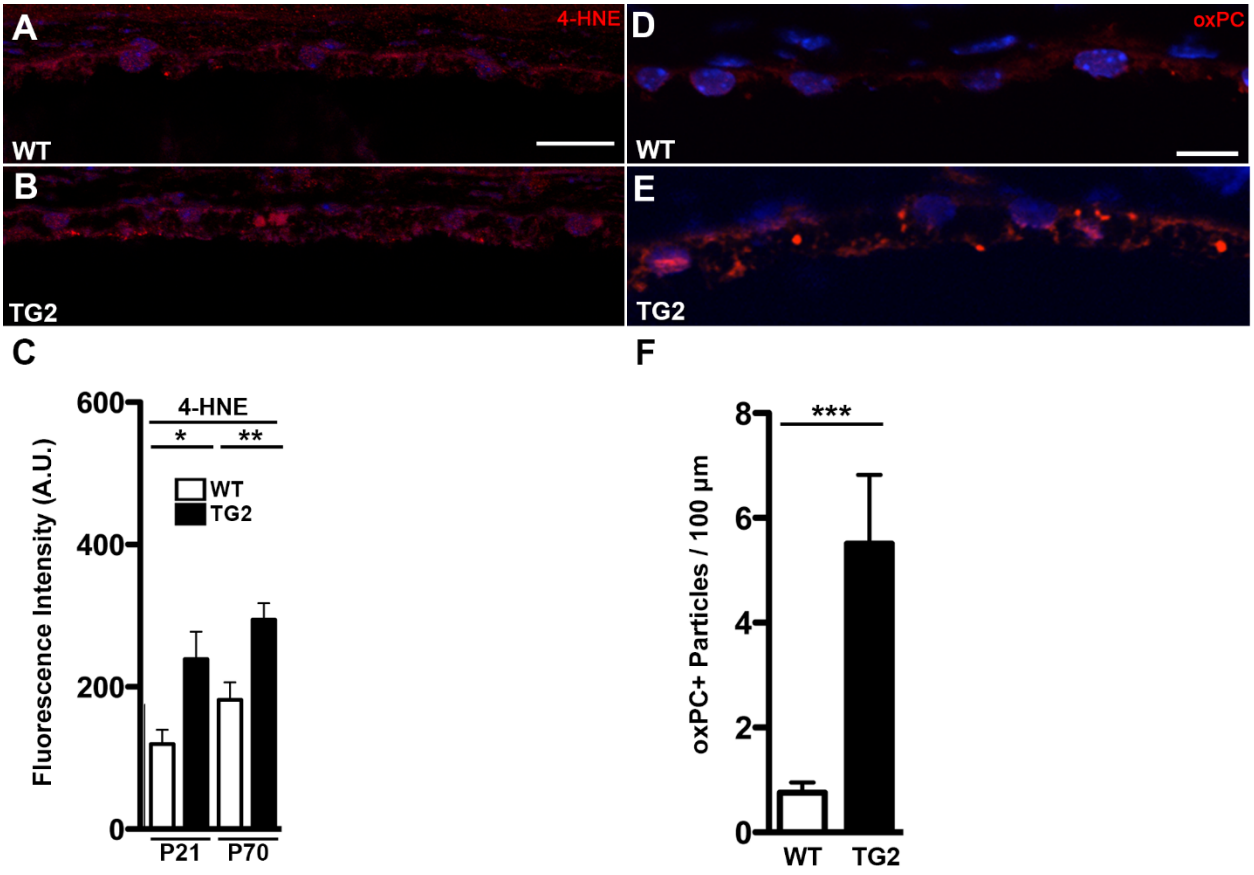

Figure 4.10: Increased oxidative stress in TG2 RPE**.** (A-C) Immunolabeling of retinal sections from WT (A) and TG2 (B) P70 mice for the oxidative stress marker 4-HNE (A and B). (C) Quantification of the fluorescence intensity from the immunolabeling revealed that TG2 RPE from both P21 and P70 mice have significantly more 4-HNE relative to WT RPE of age-matched littermates. (D, E) Immunolabeling of retinal sections from WT (D) and TG2 (E) P70 mice for oxidized phosphotidylcholine. (F) Quantification of the number of oxPC-positive particles revealed more oxidized phosphotidylcholine in P70 TG2 RPE compared with WT RPE of age-

matched littermates. Nuclei were counterstained with DAPI (blue). 4-HNE, 4-Hydroxynonenal; oxPC, oxidized phosphotidylcholine. The scale bars in (A) and (D) represent 10 μm. Error bars in (C) and (F) represent +/- S.E.M.

These abnormalities in the RPE appear to be symptoms of RPE pathogenesis, resulting from cell stress evoked by inefficient degradation of POS phagosomes, and likely contribute to the initiation of the second cell non-autonomous step, which negatively affects the health of the neural retina, leading to photoreceptor degeneration in TG2 mice. At the time that photoreceptor cell loss is first detected, around P45 (Figure 4.1E), perturbed retinal homeostasis is evident by the invasion of microglia into the subretinal space (Figure 4.12).

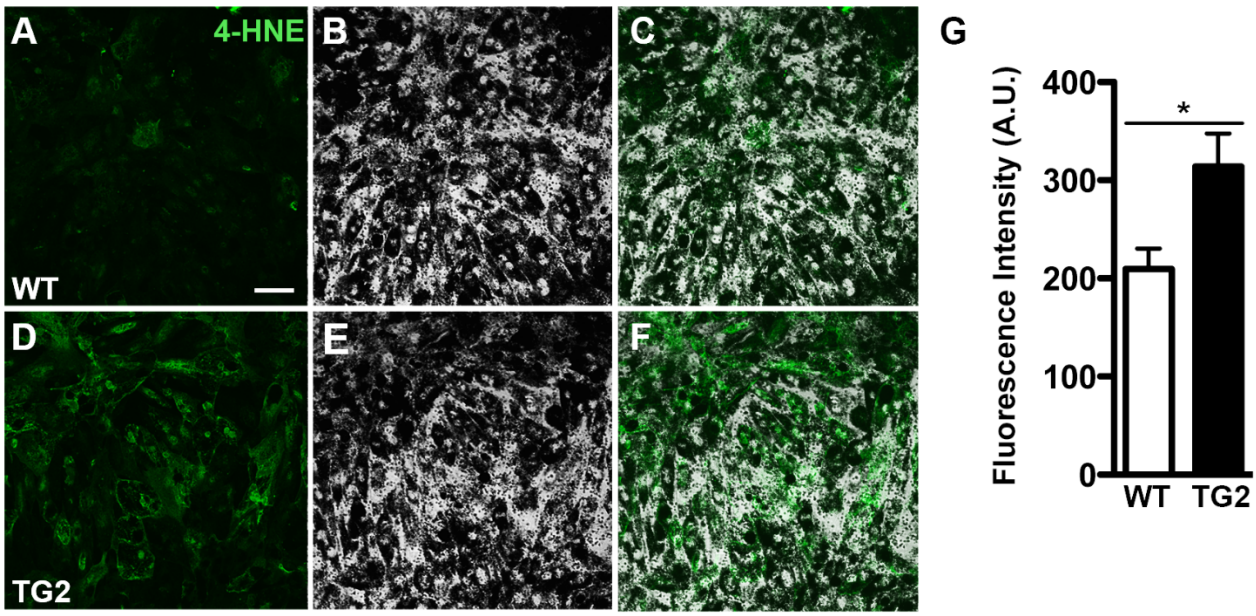

Figure 4.11: Increased oxidative stress in WT RPE fed TG2 POSs. (A-F) Primary cultures of WT RPE were incubated with WT (A-C) or TG2 (D-F) POSs for 2 h, and immunolabeled for the oxidative stress marker, 4-HNE. Phase contrast micrographs (B, E), merged with the immunofluorescence signal of 4-HNE (A, D), are shown in panels (C) and (F). (G) Quantification of the 4-HNE fluorescence signal showed that RPE cells fed TG2 POSs had significantly more 4-HNE adducts relative to those fed WT POSs. Scale bar in (A) represents 10 μm. Error bars in (G) represent +/- S.E.M.

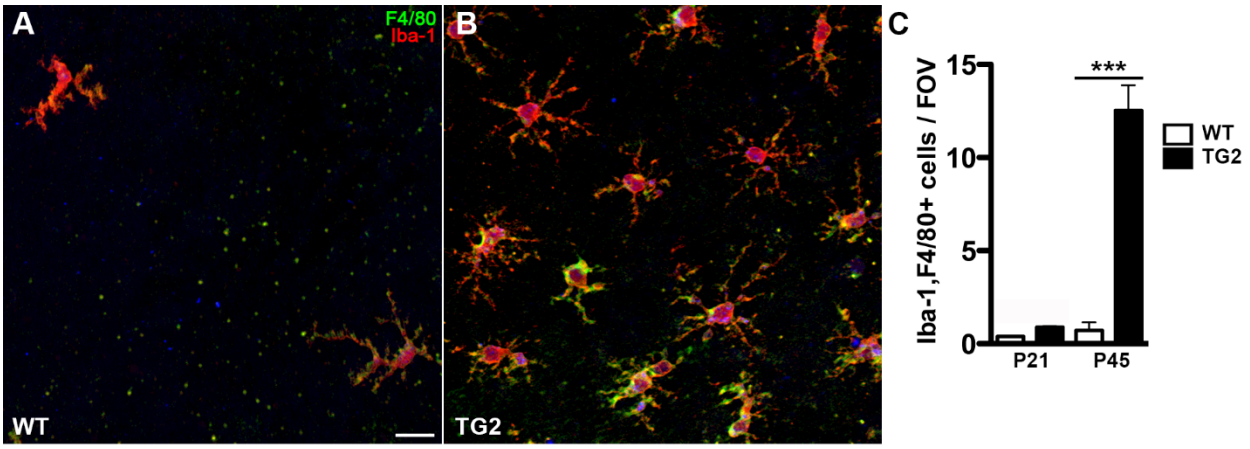

Figure 4.12: Activated microglia in the retina of TG2 mice. (A, B) Images of retinal RPE/Choroid flatmounts, corresponding to the central region of P45 WT (A) and TG2 (B) mice, immunolabeled with antibodies against F4/80 and Iba-1, as markers for microglia. Note the significantly higher number of subretinal, activated microglial cells in the RPE/Choroid flatmounts from TG2 mice (B). The presence of the activated microglia in the subretinal space was observed in retinal sections. The microglia adhere to the apical surface of the RPE during the preparation of a flatmount, so that they are retained even though the neural retina has been removed. (C) Quantification of subretinal microglial cells positive for Iba-1 and F4/80 immunolabeling in RPE/Choroid wholemounts of P21 and P45 WT and TG2 mice (ANOVA with Tukey's post-hoc test, ***, $P < 0.0001$. n=3 animals /group at P21 and n=5 animals/group at P45). FOV, field of view. Scale bar in (A) represents 10 μm. Error bars in (C) represent +/- S.E.M.

4.3 Materials and Methods

4.3.1 Mice

Animal use followed National Institutes of Health guidelines under an approved protocol. Mice were kept on a 12 h light/dark cycle under 10–50 lux of fluorescent lighting during the light cycle. Transgenic mice were generated on C57BL/6J genetic background (JAX) by inserting the *STGD3* allele of the human *ELOVL4* gene into the mouse genome, under the interphotoreceptor retinoid-binding protein (*IRBP*) promoter, as described previously (Karan et al., 2005).

4.3.2 Isolation and Culture of Primary RPE Cells

Primary cultures of RPE isolated from 10- to 15-day-old WT mice were prepared as described previously (Gibbs et al., 2003; Gibbs and Williams, 2003). Cells were then plated on

Transwell inserts (6.5 mm) with polyester membranes (Corning, Corning, NY) for phagocytosis assays, or on glass-bottom slides (MatTek, Ashland, MA) for live-cell imaging experiments. Cells were maintained in DMEM with high glucose, 10% fetal bovine serum (FBS), 2.5 mM L-glutamine, non-essential amino acids and antibiotics (Invitrogen) for 7-10 days for phagocytosis assays, or for 3 days for live-cell imaging experiments.

4.3.3 Culture and Transduction of ARPE19 Cells

ARPE19 cells were grown at 37 ºC with 5% CO_2 in DMEM-F12 with 10% FBS, 1 mM penicillin/streptomycin (Life Technologies, Carlsbad, CA) and glutamine (Life Technologies). Cells were plated on glass coverslips, and used for phagocytosis assays when confluent. For transduction experiments, the cells were incubated with Adenovirus Type 5 (Ad5) particles containing GFP, WT Elovl4, or mutant Elovl4 (generous gift from Drs Martin-Paul Agbaga and Robert E. Anderson, Dean McGee Eye Institute) for 24 h. They were then fixed with 4% formaldehyde in 0.1 M phosphate buffer for 10 min at room temperature (RT), and immunolabeled with anti-ELOVL4 (Abcam; ab14922) and anti-HA (Abcam). The ELOVL4 antibody was raised against an N-terminal epitope (amino acids 2-22 of human ELOVL4) and reacts with both human and mouse ELOVL4. For peptide competition, the immunizing peptide (Thermo Scientific) was preincubated with the ELOVL4 antibody for 1 h at RT before the antibody was applied to the cells.

4.3.4 POS Phagocytosis in Cell Culture

4.3.4.1 Purification of POSs

Mouse POSs were isolated from dark-adapted, 3- to 4-week-old WT and TG2 mice on a C57BL/6J background, as described previously (Jiang et al., 2015), with minor modifications. Briefly, POSs were isolated using a discontinuous OptiPrep 8%-10%-15% step gradient in Ringer's solution (130 mM NaCl, 3.6 mM KCl, 2.4 mM $MgCl_2$, 1.2 mM $CaCl_2$, 10 mM HEPES,

adjusted to pH 7.4 with KOH, 0.02 mM EDTA). Retinas were vortexed for 4 x 10 s, followed by a 1000 rpm centrifugation for 30 s at 4°C in a Sorvall HB-4 rotor, loaded on top of the OptiPrep gradient and centrifuged for 20 min at 12,000 *g*. POSs were collected at the 10%-15% interface and diluted 3 times with Ringer's solution. POSs were counted on a hemocytometer and their concentration was adjusted to 1-5 x10^7 POSs/ml. For live-cell imaging, POSs were isolated from 3- to 4-week-old WT and TG2 mice on a RHO-EGFP background, following the method described above.

4.3.4.2 Rate of POS Degradation

The ability of primary cultures of WT RPE cells to digest POSs was determined, as described previously (Diemer et al., 2008; Esteve-Rudd et al., 2014). Briefly, equivalent amounts of purified POSs from WT or TG2 mice were fed to RPE cells grown on Transwell inserts, and incubated for 10 min at 37 °C and 5% CO_2. Unbound POSs were then removed by extensive washing. Some cultures were fixed and processed for RHO immunofluorescence (pulse time point) while others were chased for 2 h, and then processed for immunofluorescence. The number of bound and ingested POSs were identified and distinguished from each other as described previously (Esteve-Rudd et al., 2014), and determined by counting immunofluorescent bodies ≥ 1 µm in diameter. Briefly, cells were washed 3 times in PBS and blocked in blocking buffer (PBS containing 1% goat serum) and labeled with RHO rabbit polyclonal antibody (pAb01) (Boesze-Battaglia et al., 1997; Liu et al., 1999), followed by an Alexa 568-nm conjugated goat anti-rabbit antibody (Molecular Probes, USA) for 1 h. Cells were then washed 3 times in PBS and permeabilized with 50% ethanol for 5 min at RT. After permeabilization, cells were incubated for 1 h with a combination of pAb01 and a mouse monoclonal antibody against the C-terminal portion of RHO (1D4 antibody, Millipore, USA), followed by a 30 min incubation with anti-rabbit IgG Alexa 488-nm and anti-mouse IgG Alexa-647 conjugated secondary antibodies (Life Technologies, USA). The Transwell filters

were excised and mounted with FLUORO-GEL with DAPI or Tris buffer (Electron Microscopy Sciences, USA).

4.3.5 Immunofluorescence of Cultured RPE Cells

WT RPE cells were incubated with either WT or TG2 POSs for 20 min, washed extensively to remove unbound POSs, chased for 1 h, and then fixed with 4% formaldehyde in 0.1 M phosphate buffer for 10 min at RT before being processed for immunofluorescence. After fixation, cells were blocked in 5% normal goat serum (NGS), 1% bovine serum albumin (BSA) in PBS with 0.25% Triton X-100 for 1 h at RT. Cells were then incubated for 1 h at RT with primary antibodies against RHO (monoclonal 4D2, Millipore, Temecula, CA) and RAB7A (Cell Signaling Technology) or ELOVL4 (Abcam ab14922). Finally, cells were incubated with Alexa Fluor-conjugated secondary antibodies for 1 h at RT, washed, and mounted with DAPI. Quantitative co-localization of POS-opsin and RAB7A immunolabelings was evaluated using FluoView FV1000 software (Olympus). For motor protein association, WT RPE cells were used in a phagocytosis assay, as described above, fixed with ice-cold methanol for 10 min at -20 °C, and processed for immunofluorescence using primary antibodies against RHO (pAb01) and DIC (Millipore, Temecula, CA), followed by incubation with the appropriate Alexa Fluor-conjugated secondary antibodies for 1 h at RT. RHO-DIC association was quantified by measuring co-localization of the immunofluorescent signals as well as clustering of DIC around RHO-positive phagosomes.

4.3.6 Live-Cell Imaging of Cultured RPE Cells

POSs from RHO-EGFP mice that were crossed with the TG2 line were purified, and fed to cultures of WT primary mouse RPE cells for 20 min. Following this pulse, phagosomes were imaged using an UltraVIEW Spinning Disk Confocal Microscope system with a Zeiss Axiovert photomicroscope including an environment chamber. A 63x oil objective with a Numerical

Aperture of 1.46 was used, and movies were taken using a Hamamatsu 5.0.2 camera. Movies were acquired with the Volocity software and processed using the Volocity and Imaris software. RPE cells grown on glass-bottom dishes were imaged at 37 °C. Movies were taken after feeding cells with POSs for 20 min and washing away unbound POSs. 90-second movies at 2.9 frames per second from 12 – 15 fields of view per condition were recorded. The experiment was repeated 3 times.

4.3.7 Immunofluorescence of Retinal Tissue

For the quantification of phagosomes in vivo, WT and TG2 mice were kept under the same light cycle. They were euthanized 0.5 h and 3 h (± 15 min) after light onset and eyes were fixed in 4% formaldehyde in 0.1 M phosphate buffer. Eyecups were incubated in sucrose (15, 20 and 30% each for 1 h at least), embedded in OCT and frozen at -80 °C until use. 10-µm cryosections were cut along the entire dorso-ventral axis, and immunolabeled with RHO pAb01. RHO-positive particles ≥ 1 µm in diameter within the RPE were counted in dorsal and ventral areas of 3 non-consecutive sections of at least 3 mice from each genotype.

For immunolocalization of ELOVL4, and the assessment of oxidative stress adducts and microglial markers, in retinal sections, eyecups were processed as above. Then, 12-µm sections were cut, and quenched for 15 min in 50 mM ammonium chloride. Sections were blocked in 5 % NGS or normal donkey serum (NDS), 1% BSA in PBS with 0.25% Triton X-100 for 1 h at RT. They were incubated with primary antibodies against RHO (mAb4D2 or pAb01), ELOVL4 (Abcam ab14922 (N-terminal), or a rabbit pAb (C-terminal) that was kindly provided by Dr Martin-Paul Agbaga (Agbaga et al., 2008), 4-hydroxynonenal (4-HNE) (Alpha diagnostic International, San Antonio, TX), oxidized phosphtidylcholine (oxPC) (Sigma-Aldrich, St. Louis, MO), or F4/80 (AbD Serotec, Raleigh, NC) at 4 °C overnight in blocking buffer, and finally with corresponding secondary antibodies conjugated to Alexa Fluor fluorophores for 1 h at RT.

Sections were imaged on an FV1000 confocal microscope. Quantitative analysis was performed on images taken under identical settings, and 16-bit single optical slices were analyzed on ImageJ. Negative controls, in which incubation with the primary antibody was omitted, were processed in parallel in each case. The labeling of retinal sections with ELOVL4 antibodies was repeated a minimum of 4 times with sections from different WT or mutant mice.

4.3.8 Electroporation of Human *ELOVL4* cDNA into Murine Retinas

A plasmid containing cDNA of WT human *ELOVL4* (with N-terminal FLAG tag) was purchased from GeneCopoeia. PCR-mediated site-directed mutagenesis was performed to create the 5-bp deletion (delAACTT at 790-794) that is found in the STGD3 allele. A 4 μg/μl DNA solution, containing either a WT or mutant plasmid, together with a Dendra2-expressing construct, was injected into the subretinal space of P2 Crl:CD1 (ICR) mice with a FemtoJet® 4i system (Eppendorf), and electroporated with an ECM 830 Square Wave electroporation system (BTX). The animals were euthanized at P14, and the eyes were processed as above. To detect FLAG-ELOVL4, 14-μm sections were immunolabeled with FLAG antibodies (Cell Signaling) and imaged on an FV1000 confocal microscope (Olympus).

4.3.9 Light Microscopy

Eyes were removed and immersion-fixed in 2% formaldehyde, 2.5% glutaraldehyde in 0.1 M cacodylate buffer. Eyecups were processed for embedment in an Epon-Araldite mixture as described elsewhere (Volland et al., 2015). Semi-thin sections (0.7 mm) were obtained along the entire dorso-ventral axis, passing through the optic nerve head, and stained with 1% toluidine blue in 1% Sodium borate. Nuclei from 4 properly aligned rows of photoreceptors were counted at 0.5-mm intervals along the section.

4.3.10 Electron Microscopy

Mouse eyes were enucleated 1.5 h post light onset, and fixed with 4% formaldehyde and 0.2% glutaraldehyde in 0.1 M sodium cacodylate buffer at 4 °C. Eyecups were prepared as mentioned above. Samples were washed in 0.1 M sodium cacodylate buffer, gradually dehydrated with increasing levels of ethanol solutions (30-90%), and infiltrated with, and embedded in LR-white resin. Ultrathin sections (70 nm) were collected on formvar-coated nickel mesh grids, and treated with 0.1% glycine, blocked in 2% BSA, and incubated with RHO mAb4D2 in 0.1 M phosphate buffer over night at 4 ^{o}C. Grids were then washed in 0.1 M phosphate buffer, and incubated with a 12-nm gold secondary antibody (Jackson Immuno Research Labs, West Grove, PA). Contrast stain with 5% uranyl acetate in ethanol was performed for 5 min. Samples were imaged with a JEM 1200-EX (JEOL) at 80 kV at magnifications of 10,000-30,000x. Immunolabeled phagosomes were counted and assigned to one of three locations in the RPE: microvilli, apical, or basal region.

4.3.11 Statistical Analyses

Statistical analysis was performed on GraphPad Prism 5 (La Jolla, CA). Two-tailed Student *t*-tests were used to test the probability of no significant difference between mutant and control samples. To test for three or more groups, we performed one-way ANOVA followed by Tukey's *post-hoc* test. A chi-square test was used to analyze the colocalization of RHO and RAB7A.

4.4 Discussion

Mechanisms underlying retinal degeneration due to dominant mutations in *ELOVL4* have remained a puzzle, despite numerous cell culture and mouse model studies. As for most other forms of macular degeneration, RPE pathogenesis has been implicated (Karan et al., 2005; Kuny et al., 2015). However, the RPE does not express ELOVL4 (Agbaga et al., 2008; Mandal et al., 2014) (Figure 4.1G). In the present study, we describe cellular mechanisms that account

for RPE pathogenesis. Our results indicate that mutant ELOVL4 protein localizes abnormally to the outer segments of photoreceptor cells, and passes to the RPE cells, in phagosomes, as a result of the normal daily process of phagocytosis. We found that the ELOVL4-containing phagosomes are degraded less efficiently by the RPE cells, thus introducing toxicity to these professional phagocytes. We propose that observed defects in phagosome motility contribute to the retarded phagosome degradation, and that the impaired motility is possibly due to abnormal sequestration of RAB7A, which alters the association of the phagosome with the dynein motor protein (Lebrand et al., 2002; Rai et al., 2016).

Cell non-autonomous effects are common in neurodegenerations (Ilieva et al., 2009). However, the pathogenesis associated with STGD3 maculopathy is highly unusual due to two cell non-autonomous effects. The toxicity introduced to the RPE by phagocytosis of ELOVL4-containing POS disk membranes represents the first of the two. The subsequent effects on the neural retina, including photoreceptor cell loss, due to RPE pathology represents the second. There are some similarities with STGD1 maculopathy, which is also characterized by RPE defects, and ensuing photoreceptor cell loss. STGD1 is caused by recessive mutations in *ABCA4* (Allikmets et al., 1997). However, unlike *ELOVL4*, *ABCA4* is expressed by the RPE as well as the photoreceptor cells, and the in vivo RPE pathogenesis of STGD1 appears to be largely cell autonomous (Lenis et al., 2018).

How does the presence of ELOVL4 protein alter the disk membranes, so that POS phagosomes interact differently with RAB7A, and are degraded more slowly by WT RPE? The C-terminal truncated mutant ELOVL4, as expressed in TG2, has lost its ER retention motif, but it still contains a normal catalytic region, suggesting that its presence in the TG2 disk membranes might result in additional very long chain fatty acids. On the other hand, no difference in levels of retinal VLC-PUFAs was detected between WT and TG2 retinas (Mandal et al., 2014), and tests of the mutant ELOVL4 enzyme detected no activity (Logan et al., 2013), suggesting that the

POS membranes may be affected solely by the abnormal presence of the mutant (transmembrane) protein. Indeed, the presence of mutant ELOVL4 protein in the POSs appears capable of altering disk membrane organization of the POSs, if at a high enough concentration. In a transgenic mouse line that expresses mutant *ELOVL4* at 60% higher levels than that in the TG2 line, the disks are not stacked normally and appear disorganized, in contrast to the disk membranes in the TG2 mice, which appear normal by electron microscopy (Karan et al., 2005).

In the TG2 mice, a defect in the POS membranes became evident once the membranes had been ingested by the RPE. The altered behavior of the TG2 POS phagosomes, as described here, emphasizes that the content of a phagosome can have a significant effect on the ability of a phagosome to associate with proteins that influence its maturation, including motor-linking proteins and thus the motor proteins themselves. Initially, the outer membrane of a phagosome comes from the plasma membrane of the phagocyte. However, phagosomes, including POS phagosomes (Wavre-Shapton et al., 2014), undergo a series of fusion-fission events with endolysosomes as they mature, resulting in drastic remodeling of the phagosomal membrane and contents (Vieira et al., 2002). Particularly, when the ingested material contains a high concentration of membranes, as in the case of a POS phagosome, the observed membrane coalescence (Young, 1971) is likely to involve a mixing of membranes that results in an outer membrane that contains components of the ingested membrane. The content of a membrane affects motor protein association (Klopfenstein et al., 2002; Nelson et al., 2014; Rai et al., 2016). For example, increased cholesterol in the membrane of motor protein cargoes has been shown to increase RAB7 association, which results in more dynein and less kinesin activity (Lebrand et al., 2002). RAB7 interacts with the cholesterol sensor, ORP1L (Rocha et al., 2009), and was found recently to associate with cholesterol and dynein in microdomains on the surface of latex bead phagosomes (Rai et al., 2016). Understanding the molecular perturbation

in the membrane of POS phagosomes from TG2 mice is likely to further our understanding of molecular motor linkage and regulation.

The importance of phagosome motility for degradation was suggested from studies illustrating mislocalized and immature POS phagosomes in the opossum RPE after intraocular treatment with colchicine, which inhibits microtubule polymerization (Herman and Steinberg, 1982a). Subsequently, impairment of POS phagosome motility and degradation was found in the RPE of mice lacking the actin motor protein, myosin-7a (Gibbs et al., 2003), or the light chain of the microtubule motor protein, kinesin-1 (Jiang et al., 2015). However, phagosome degradation is likely dependent upon the motility of other organelles, especially endolysosomes (Desjardins et al., 1994), so that the specific impact of impaired phagosome motility on phagosome degradation cannot be determined by altering motility throughout the RPE cell. In the present cell culture studies, where mutant TG2 POSs were fed to WT RPE cells, we were able to pinpoint the motility defect specifically to the phagosome organelle, and thus demonstrate the importance of the motility of the phagosome *per se*.

Chapter 5

Differentiation of RPE Cells from Integration-free iPS Cells and Their Cell Biological Characterization

5.1 Introduction

The retinal pigment epithelium (RPE) is a monolayer of cells that provides essential roles for the function and viability of the photoreceptor cells (Sparrow et al., 2010). Age-related macular degeneration (AMD) is a widespread and common disease among the elderly, leading to irreversible loss of central vision. The death of macular photoreceptors has been suggested to be secondary to the degeneration of the RPE (Curcio et al., 1996; Zarbin, 2004; Anderson et al., 2010; Bhutto and Lutty, 2012). Therefore, one promising form of treatment for AMD is the transplantation of healthy RPE cells into the retinas of human patients to restore lost functions, and potentially halt or reverse the progression of the disease.

Pluripotent stem cells, including both human embryonic stem cells (ESCs) and human induced pluripotent stem cells (iPSCs) can provide a renewable source of human RPE cells, which are potentially amenable for studying normal and disease mechanisms in culture, and for intraocular transplantation for disease treatment. Patient-derived iPSC-RPE offer disease modeling and testing of pharmacologically-active compounds, in addition to autologous transplantation, without the need for immunosuppression (Mandai et al., 2017). Originally, iPSCs were generated by exogenous expression of the factors described by Yamanaka's group (OCT4, SOX2, KLF4, and c-MYC) from retroviral vectors, thus resulting in genome integration (Takahashi et al., 2007). To circumvent the risks of genome integration, several non-integrating methods are now being used to induce pluripotency in mammalian cells, including non-integrating episomal vectors (Yu et al., 2009), delivery of RNA (Warren et al., 2010) and proteins (Kim et al., 2009a), and use of small molecule compounds (Hou et al., 2013). Once reprogrammed to pluripotency, the iPSCs can spontaneously differentiate along the neural

lineage, and, further, to RPE cells, which are readily discernible due to their pigmentation and cobblestone appearance (Kawasaki et al., 2002; Buchholz et al., 2009). Several laboratories have now published protocols for the differentiation of human ESCs or iPSCs to RPE cells, using more directed approaches so as to increase the yield of RPE cells (Idelson et al., 2009; Buchholz et al., 2013; Gong et al., 2015; Maruotti et al., 2015). Taken together, the current technology allows for the generation of patient-specific iPSCs that are free of integrated reprogramming genes, and can subsequently be used to generate the quantities of functional RPE cells necessary for transplantation purposes.

This paper reports the use of a non-integrating approach to generate iPSCs for the generation of RPE cells under GMP-compatible practices. We have performed in vitro characterization of the iPSC-RPE to test whether they express RPE-specific genes and proteins. Importantly, we have also tested for the first time whether RPE cells, derived from any type of stem cell, possess normal cytoskeletal organization, organelle motility, and phagosome ingestion with degradation kinetics, thus detailing critical cellular functions of the RPE in relation to RPE dystrophy. The importance of these tests, which includes live-cell imaging analysis, has been emphasized by recent studies showing that defects in intracellular motility lead to RPE pathogenesis like that in AMD (Jiang et al., 2015), potentially the most significant target disease of RPE transplantation. We have also tested these iPSC-RPE in vivo, using mouse models, to determine whether the cells can integrate into a recipient tissue, and rescue a function lost by the host retina. Our results show that iPSCs, generated with a non-integrating method, can serve as a renewable source of functional RPE cells, which can be used for detailed cell biological analyses of pathogenicity in vitro, as well as for transplantation in treatment of retinal diseases.

5.2 Results

5.2.1 RNA-Based Reprogramming of Fibroblasts into iPSCs

Mechanical (i.e. scalpel) and enzymatic (i.e. collagenase) methods were used to isolate fibroblasts from human dermal tissue obtained via skin biopsy. The identity of fibroblasts was confirmed by immunolabeling for FSP-1 (Figure 5.1A), and for vimentin (Figure 5.1B). Immunolabeling revealed that ≥ 95% of the cells expressed both FSP-1 and vimentin. The fibroblasts could be cultured and propagated using xeno-free conditions; they remained stable in culture for at least 5 passages.

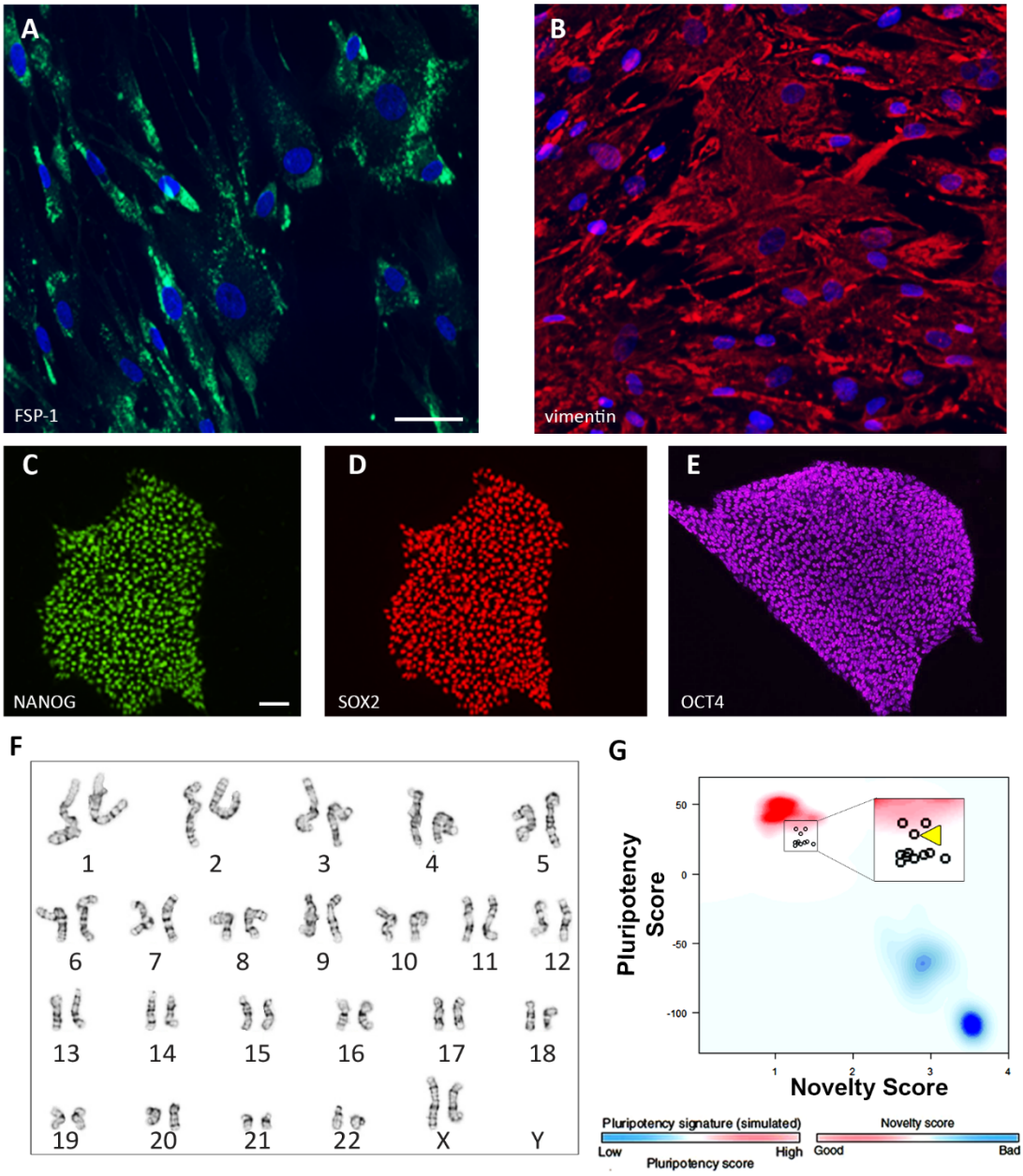

Figure 5.1: Reprogramming of human fibroblasts into induced pluripotent stem cells. (A, B) Fibroblast cells immunolabeled with antibodies against FSP-1 (A, green), or vimentin (B, red). DAPI (blue) was used to counterstain the nuclei. (C-E) iPSCs immunolabeled with antibodies against NANOG (C), SOX2 (D), and OCT4 (E). Expression of these proteins indicates the identity of iPSCs derived from fibroblast reprogramming. (F) Normal karyotype of an iPSC line determined by G-banding. (G) Results from PluriTest assay show that our iPSCs have a pluripotent signature (high pluripotency score and low novelty score), and cluster with well-characterized *bona fide* iPSC and ESC lines (red background hint; iPSC line 2 is indicated by a yellow arrowhead in the magnified panel) and not with partially differentiated pluripotent cells or somatic tissue (blue background hint). Scale bars: (A) and (B), 50 μm; (C-E), 20 μm. Abbreviations: FSP-1, fibroblast-specific protein-1.

To generate iPSCs, using a non-integrating method, we transfected the fibroblasts with the VEE RNA vector (Yoshioka et al., 2013), which induces exogenous expression of pluripotency markers, including OCT4, KLF4, SOX2, and GLIS1. Following puromycin selection, cells were replated and cultured on Matrigel for 3-4 weeks, when the formation of iPSC colonies was evident. The identity of iPSCs was confirmed by immunolabeling for pluripotency markers, including NANOG, SOX2, and OCT4 (Figure 5.1C-E). Normal karyotype was shown by G-banding (Figure 5.1F). Additionally, the iPSCs were capable of generating cells from all 3 embryonic germ layers in a bioinformatics assay for pluripotency, PluriTest (Figure 5.1G).

5.2.2 Differentiation and Characterization of iPSC-RPE

To derive RPE cells, colonies of iPSCs (Figure 5.2A) were transferred as suspension cultures in low-adherent dishes to generate EBs (Figure 5.2B). After 2 weeks in culture, Activin A, TGFB1, and FGF2 were added to the medium for a period of 2 weeks. Following the removal of these growth factors, we observed the appearance of pigmented EBs in as early as 4 weeks (Figure 5.2C). The pigmented regions (Figure 5.2D) of the EBs were dissected and plated as adherent cultures in RPE medium. The pigmented regions adhered as a large mass from which pigmented cells began to proliferate and migrate near the periphery (Figure 5.2E). The pigmented cells were enzymatically passaged and cultured until confluent monolayers of pigmented cells with cobblestone morphology appeared (Figure 5.2F and 5.3A-B).

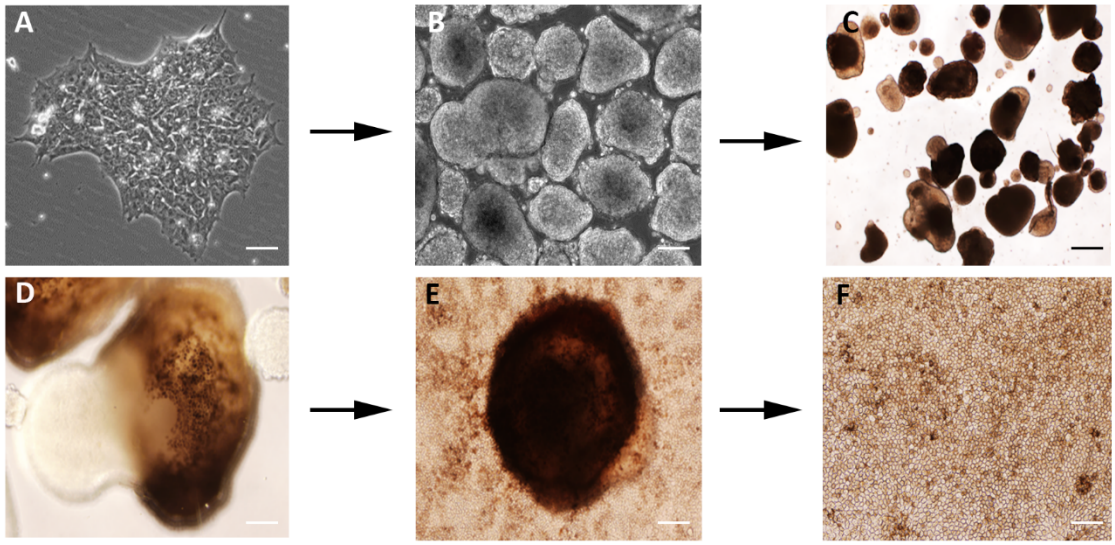

Figure 5.2: Differentiation of iPSCs into retinal pigment epithelial cells. The differentiation process begins with colonies of iPSCs plated initially on Matrigel (A) and subsequently detached to be cultured as EBs in suspension, and in the presence of NIC for two weeks (B). (C, D) The EBs became pigmented following a 2-week exposure to Activin A, TGFB1, and FGF2. The pigmented regions in the EBs were mechanically dissected and plated in RPE medium (E) giving rise to a monolayer of pigmented cells with a cobblestone appearance that can be further purified and expanded (F). Scale bars: (A) and (B), 20 µm; (C), 50 µm; (D), 10 µm; (E), 100 µm; (F), 50 µm. Abbreviations: iPSCs, induced pluripotent stem cells; RPE, retinal pigment epithelium; EBs, embryoid bodies; NIC, nicotinamide; TGFB1, transforming growth factor beta 1; FGF2, fibroblast growth factor 2.

Pigmented cells were derived from 3 individual iPSC lines, which, by western blotting, were confirmed to express the RPE-specific protein, RPE65 (Figure 5.4A). Additionally, after 2-3 months in culture, RPE cells from multiple iPSC lines showed robust expression of RPE genes, including *RPE65, MERTK,* and *BEST1*, by semi-quantitative RT-PCR (Figure 5.4B). By immunocytochemistry, these pigmented cells showed expression of RPE signature proteins, such as BEST1, RPE65, and MITF (Figure 5.4C-E), and no detectable expression of the pluripotency marker OCT4 (Figure 5.4F). Taken together, these results indicate that the pigmented cuboidal cells that were derived from our integration-free iPSCs have expression characteristics of RPE cells.

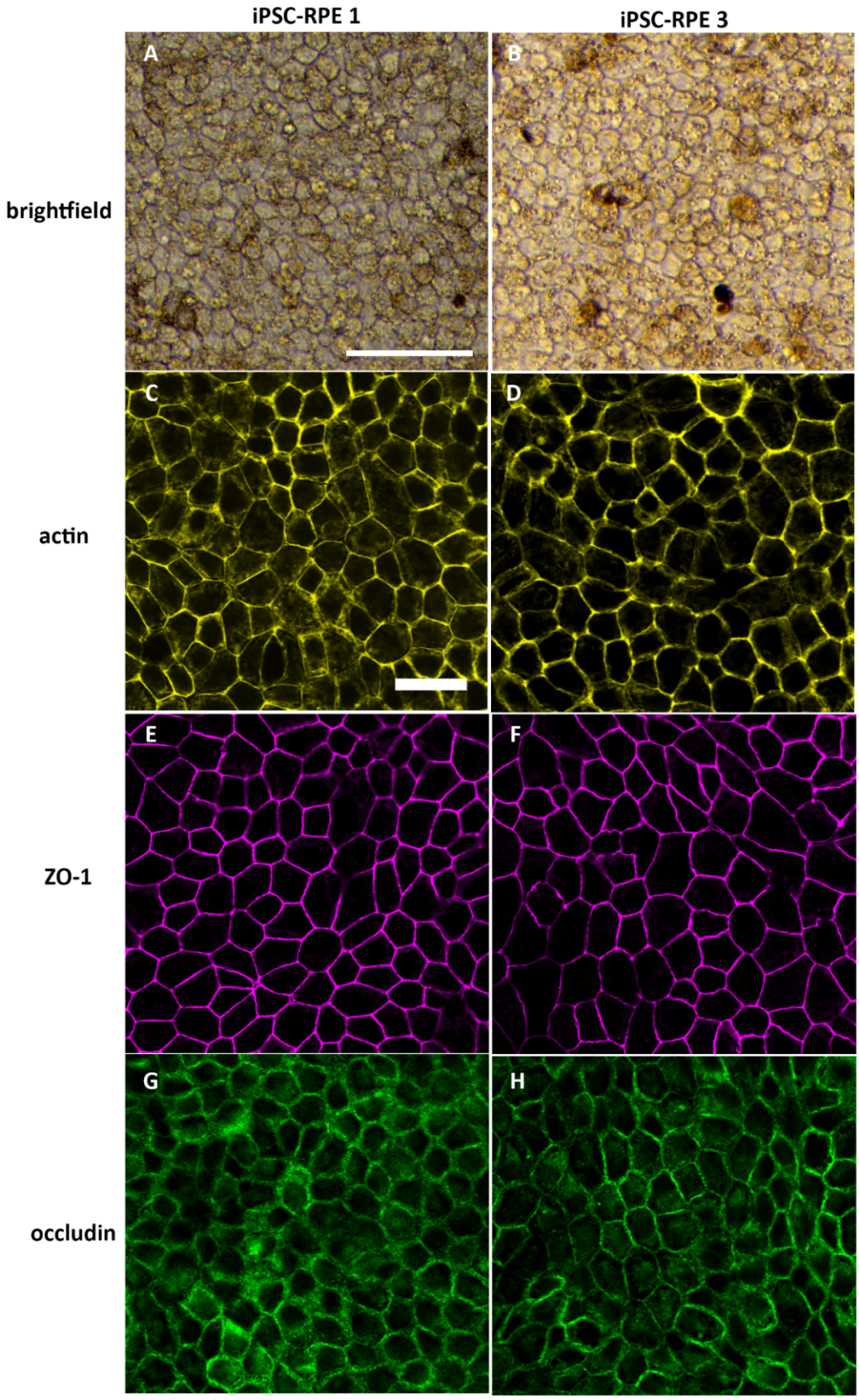
iPSC-RPE 1
iPSC-RPE 3
brightfield
actin
ZO-1
occludin
A
B
C
D
E
F
G
H

Figure 5.3: (A, B) Brightfield micrographs of iPSC-RPE 1 (A) and iPSC-RPE 3 (B), illustrating the pigmentation and cobblestone morphology of the cells. (C, D) Phalloidin labeling of iPSC-RPE 1 (C) and iPSC-RPE 3 (D), illustrating the cortical arrangement of actin filaments in the cells. (E-H) Immunofluorescence micrographs, illustrating expression of the tight junction proteins, ZO-1 (E, F) and occludin (G, H), in iPSC-RPE 1 and 3. Scale bars: (A) and (B), 60 μm; (C-H), 20 μm.

5.2.3 Phagocytosis of Photoreceptor Outer Segments by iPSC-RPE

One of the primary functions of the RPE is the phagocytosis of distal tips of POS disk membranes (Young and Bok, 1969). Defects in this process have been shown to cause photoreceptor degeneration (Bok and Hall, 1971), with defects in the degradation phase linked to RPE pathogenesis (Rakoczy et al., 2002; Jiang et al., 2015). The initial process of phagocytosis by the RPE involves binding followed by ingestion of POS membranes, two events in which integrin $\alpha_V\beta_5$ and MERTK receptors have been shown to participate in, respectively (Lin and Clegg, 1998; D'Cruz et al., 2000). While RPE cells derived from stem cells have been shown to phagocytose POS membranes, previously (Liao et al., 2010), here we have explored this function more extensively.

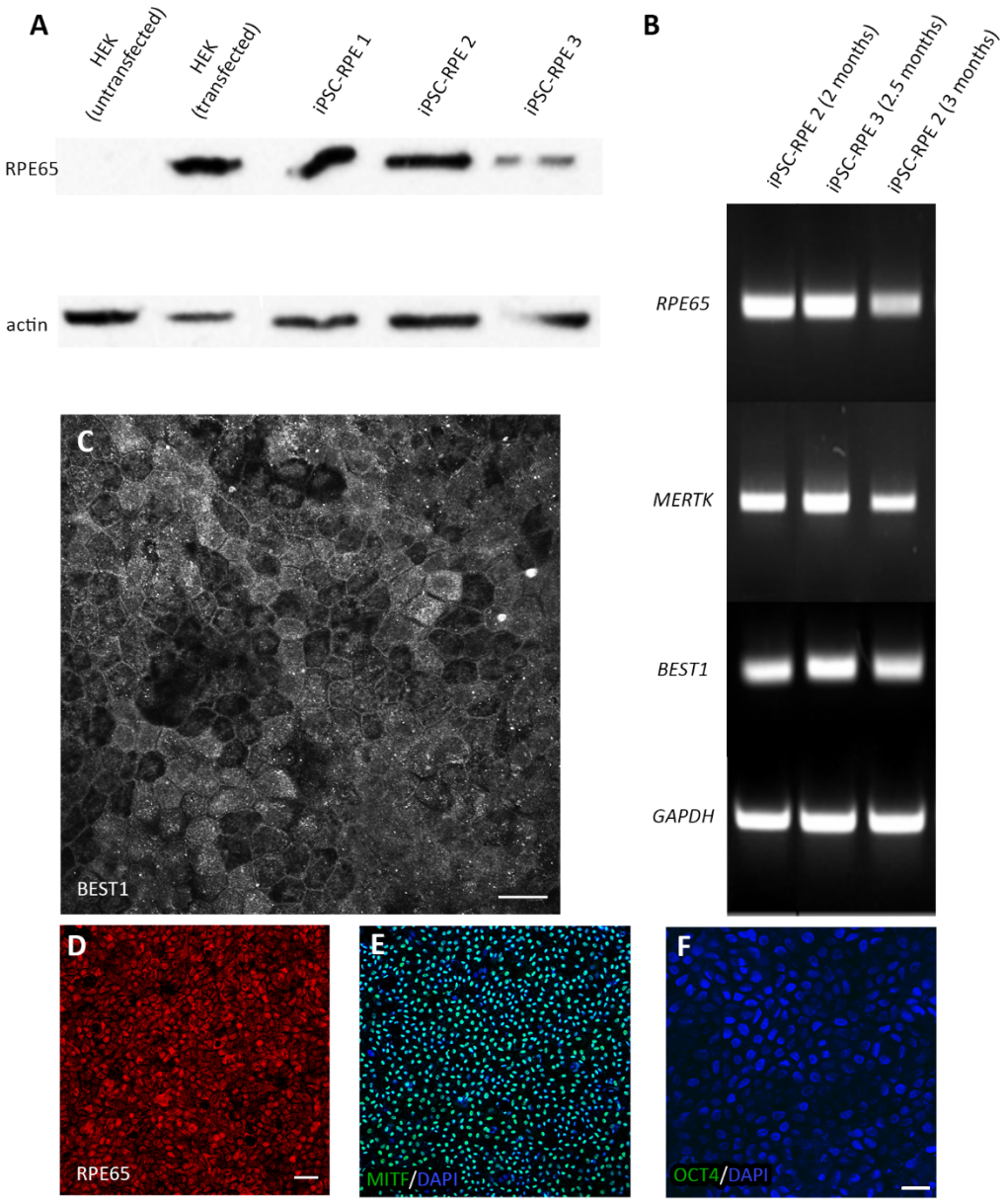

Figure 5.4: Specific protein and gene expression profiling of iPSC-derived RPE cells. (A) Expression of RPE65 by 2.5-3-month cultures of RPE cells from 3 different iPSC lines, indicated by an immunolabeled western blot. Actin was used as a loading control. (B) Expression of *RPE65, MERTK,* and *BEST1* genes in iPSC-RPE cultured for 2-3 months, detected by RT-PCR. GAPDH was used as a loading control. (C-E) Expression of the RPE-specific proteins, BEST1 (C), RPE65 (D), and MITF (E), indicated by immunofluorescence. (F) The iPSC-RPE cells showed no expression of the pluripotency marker OCT4; nuclei are labeled with DAPI. Scale bars: (C), 20 μm; (D-E), 50 μm; (F), 20 μm Abbreviations: HEK, human embryonic kidney cells; RT-PCR, reverse transcription-polymerase chain reaction; MERTK, MER proto-oncogene, tyrosine kinase; BEST1, bestrophin 1; GAPDH, glyceraldehyde-3-phosphate dehydrogenase; MITF, microphthalmia-associated transcription factor.

We first tested whether our iPSC-RPE cells expressed these receptors at their surface. Immunocytochemistry confirmed the expression of integrin $\alpha_V\beta_5$ (Figure 5.5A) and MERTK (Figure 5.5B), which colocalized at the surface of the iPSC-RPE (Figure 5.5C). To test the phagocytic function in our iPSC-RPE, we cultured the cells on laminin-coated Transwell inserts, and challenged them with porcine POSs for 2 h to allow for sufficient time for binding and ingestion to occur. Following the challenge, and after extensive washes to remove unbound POSs, some cultures were allowed additional time (2 h or 5 h) to degrade the POSs they had ingested. Using a double immunolabeling strategy for RHO, a protein abundant in the ROSs but not expressed by the RPE (Figure 5.5D), we first labeled ROSs bound to the surface of the RPE cells (Figure 5.5E), and

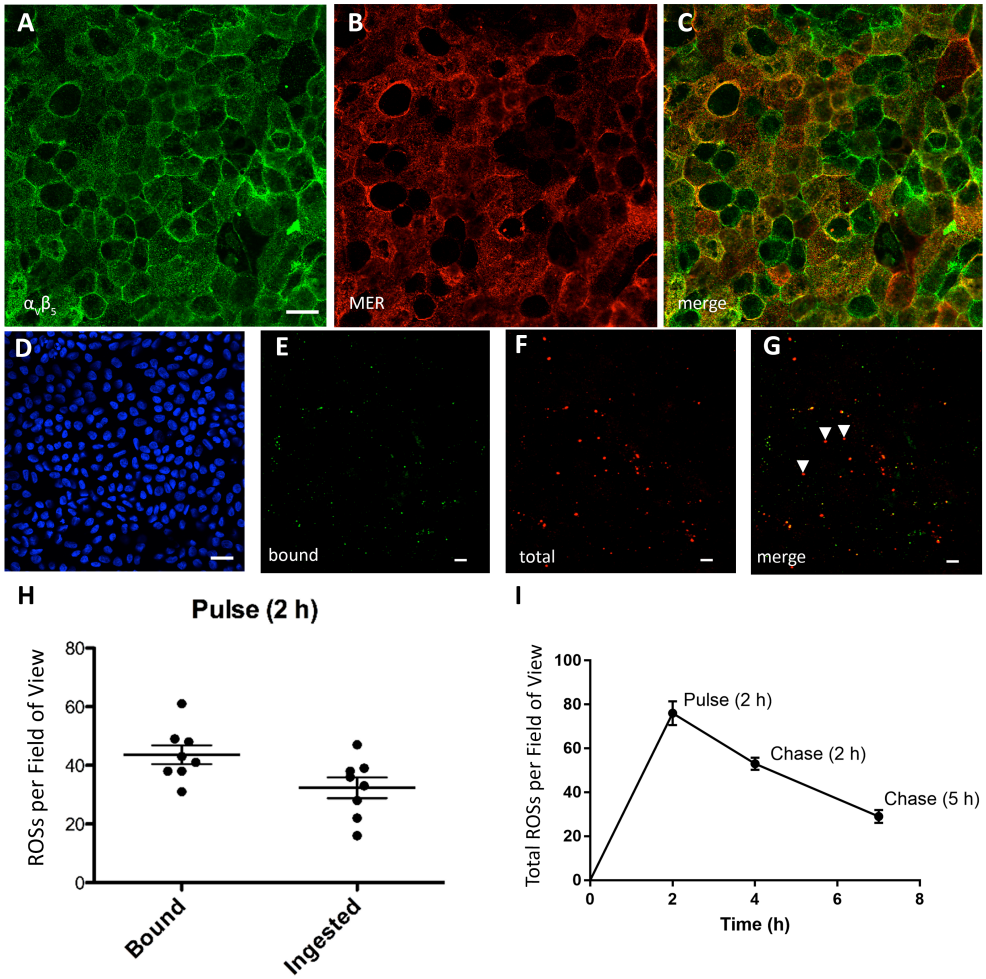

Figure 5.5: Phagocytosis of photoreceptor outer segments by iPSC-RPE in vitro. Immunofluorescence labeling of iPSC-RPE cells for integrin $\alpha_v\beta_5$ (A), and MERTK (B). These receptors are responsible for the binding and internalization of POSs, respectively, and are present on the apical surface. The image in (C) shows a merge of A and B. The ability of iPSC-RPE cells to phagocytize POSs was tested in vitro by challenging the cells with POSs isolated from porcine retinas. (D) Micrograph of iPSC-RPE cells that have not been exposed to POSs and labeled with RHO antibody. Nuclei are counterstained with DAPI. (E) A representative image of bound ROSs, labeled with an antibody against RHO and a green secondary antibody, *prior to* cell permeabilization. (F) A representative image of all (internalized and bound) ROSs labeled with the same RHO antibody, but with a red secondary antibody, *following* cell permeabilization. (G) When merged, the surface-bound ROSs appear yellow while internalized ROSs appear red. A few internalized ROSs are indicated by white arrowheads. (H) Quantification of bound and ingested ROSs was performed using the ImageJ software to count RHO-positive particles with diameters greater than 0.5 microns. (I) Total ROSs per field of view were quantified after the 2h-pulse, and after a 2h- and 5h-chase. Phagosome counts were obtained from 6-8 individual fields of view, with each field containing ≥100 cells. The data in (H) and (I) represent the mean ± SD. Scale bars: (A) and (D), 20 μm; (E-G), 5 μm.

then, after permeabilization of the cells, we labeled all ROSs (bound and ingested) (Figure 5.5F). Thus, we were able to discriminate between bound and ingested ROSs (Figure 5.5G). We found that when the iPSC-RPE were cultured on laminin-coated Transwell inserts (to achieve a polarized monolayer of cells), approximately 60% of the ROSs were bound to the surface of the cells while approximately 40% had been internalized at the end of a 2 h challenge (Figure 5.5H). When given additional time (chase) after the POS challenge, the iPSC-RPE cells were able to degrade more than 50% of the total ROS phagosomes during a 5-h chase period (Figures 5.5I and 5.6).

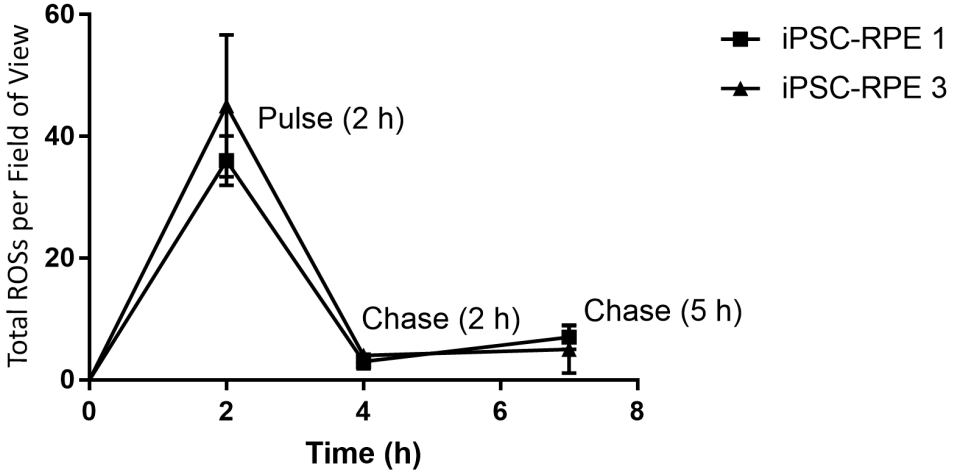

Figure 5.6: Quantification of phagocytosis in iPSC-RPE 1 and 3 exposed to porcine POSs for 2 h (pulse), washed extensively to remove unbound POSs, and then allowed either a 2 h or 5 h chase period to ingest and degrade the POSs. The graph shows the total number of ROSs quantified from confluent fields of view after the pulse and the two separate chase periods. Data represent means ± SD.

These results demonstrate that GMP-compatible iPSC-RPE cells are capable of binding, internalizing, and subsequently degrading ROSs. The rate of ROS phagosome degradation was much faster than that reported for human RPE cells from immortalized cell lines; no significant degradation of opsin was detected in human d407 cells until more than 8 h after the removal of unbound POSs (Finnemann et al., 2002).

5.2.4 Organelle Trafficking in Live iPSC-RPE

Normal trafficking of organelles is essential for the function of RPE cells (Toops et al., 2015), and is a sensitive measure of the polarized organization of their cytoskeleton, as well as their metabolic health. In particular, the process of POS phagocytosis relies on the trafficking of POS-derived phagosomes, and their interaction with degradative organelles such as endolysosomes for POS clearance (Bosch et al., 1993a; Wavre-Shapton et al., 2014). When this trafficking is perturbed, RPE health becomes compromised, with the development of AMD-like pathogenesis (Gibbs et al., 2003; Jiang et al., 2015).

Prior to examining organelle trafficking in our iPSC-RPE cultures, we used immunofluorescence confocal microscopy to evaluate the organization of the microtubules. This organization is a sensitive indicator of epithelial cell polarization. In addition, the microtubules serve as essential cytoskeletal elements for trafficking POS phagosomes and endolysosomes in the RPE (Herman and Steinberg, 1982b; Jiang et al., 2015). Transverse sections of alpha tubulin immunolabeling, at different depths in the cell body (Figures 5.7A and 5.8), show microtubules that (a) in the apical region, extended in the plane of the section, indicating a horizontal orientation, and (b) in the basal region, appeared more punctate, indicating a vertical

orientation, most concentrated adjacent to the plasma membrane. Additionally, the staining revealed primary cilia, indicated by white arrowheads in z-plane views under Figure 5.7A, emanating from the apical surface of the iPSC-RPE cells. This organization of microtubules is consistent with that observed in other polarized epithelial cells (Bacallao et al., 1989; Bre et al., 1990; Gilbert et al., 1991; Meads and Schroer, 1995).

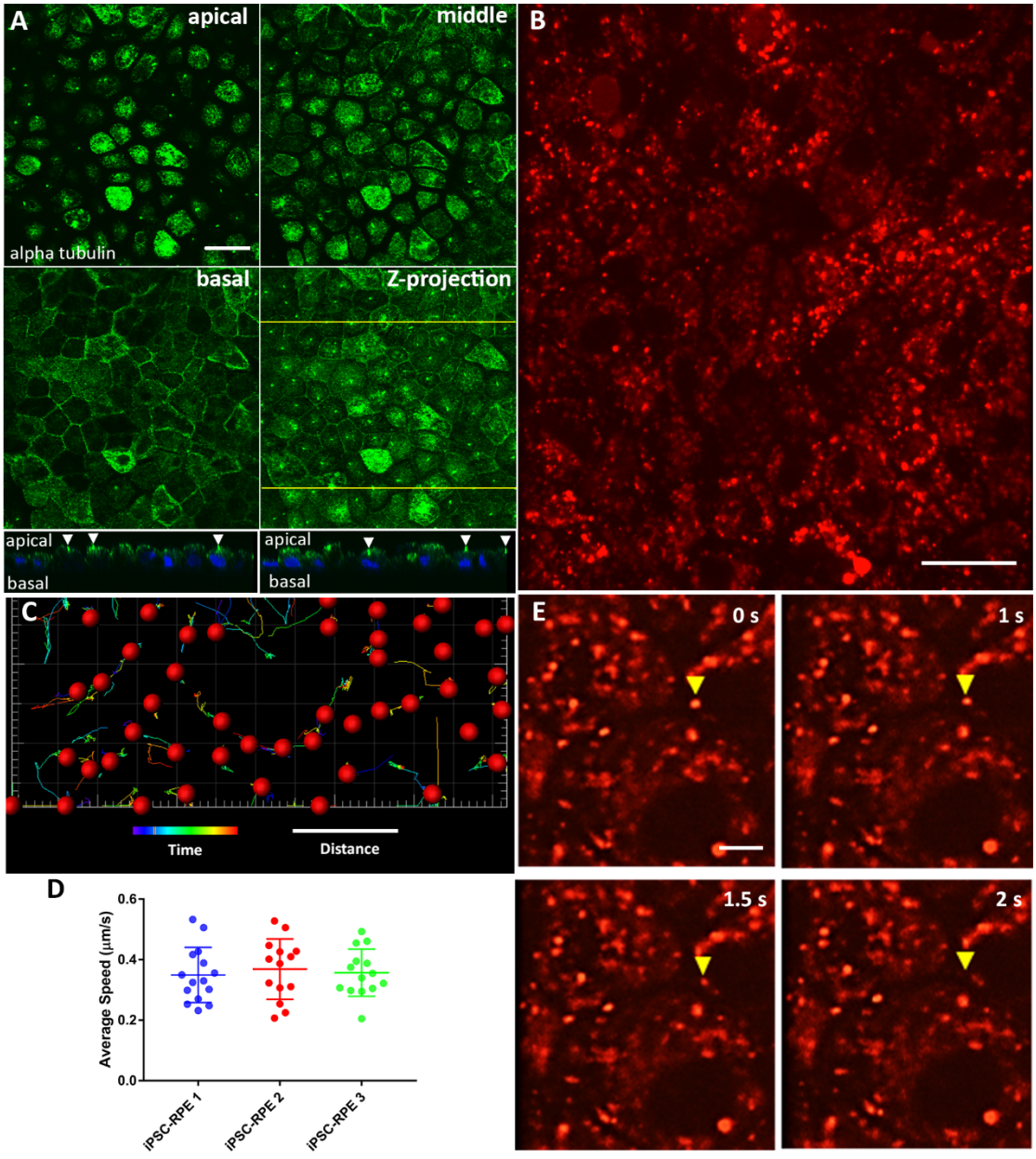

Figure 5.7: Microtubule organization and trafficking of endolysosomes in iPSC-RPE. (A) Microtubule organization in the iPSC-RPE cell bodies illustrated by immunostaining of alpha tubulin. Single-plane confocal microscopy images (2-μm apart) represent the apical and basal regions of the cell bodies, plus one plane in between (middle). The apical region of the cells is dominated by horizontal microtubules while the basal region is dominated by vertical microtubules. A z-projection of the three panels is shown in the fourth panel. Below, are images in two z-planes at the yellow lines in the z-projection image; they show primary cilia (indicated by white arrowheads) emanating from the apical surface of the RPE cells. (B) A still image from a movie of iPSC-RPE cells that were incubated with red LysoTracker to label endolysosomes (see Movie S3). (C, D) Trajectory and movement analysis of a population of endolysosomes, using a spots and tracks analysis (Imaris), following movie acquisition over a 25-sec interval. The tracks represent the trajectories of the organelles, while their colors are indicative of how far (in terms of time) they are with respect to the 25-sec movie, with cool colors being closer to the beginning of the movie, and hot colors being closer to the end of the movie. (E) Time-lapse images from a movie showing vertical movement of a labeled organelle (yellow arrowhead). Each panel represents the same z-plane at different times. The organelle moves out of the plane after 2 seconds, indicating that it is traversing different z-planes. Scale bars: (A) and (B), 20 μm; (C), 25 sec (Time), 5 μm (Distance); (E), 5 μm.

To evaluate the trafficking of organelles in our iPSC-RPE cultures, we incubated the cells with LysoTracker, which labels acidic organelles such as endosomes and lysosomes, and used high-speed spinning disk confocal microscopy to perform live-cell imaging (Figure 5.7B; Movie S3). Following movie acquisition, the tracks of labeled organelles were analyzed during a 20-40-second time interval (Figure 5.7C). We found that the average speed of labeled organelles ranged from 0.2 to 0.5 μm/s, and this range was similar among RPE cells derived from the three independent iPSC lines (Figure 5.7D). Similar speeds have been observed for LAMP2-positive organelles in polarized primary cultures of porcine RPE (Toops et al., 2014), and they represent a range consistent with microtubule transport. Interestingly, many of these labeled organelles can be seen moving in and out of the x-y-plane, suggesting vertical motility along the z-axis (Figure 5.7E), consistent with the presence of vertical microtubules, which are a hallmark of well-polarized epithelial cells.

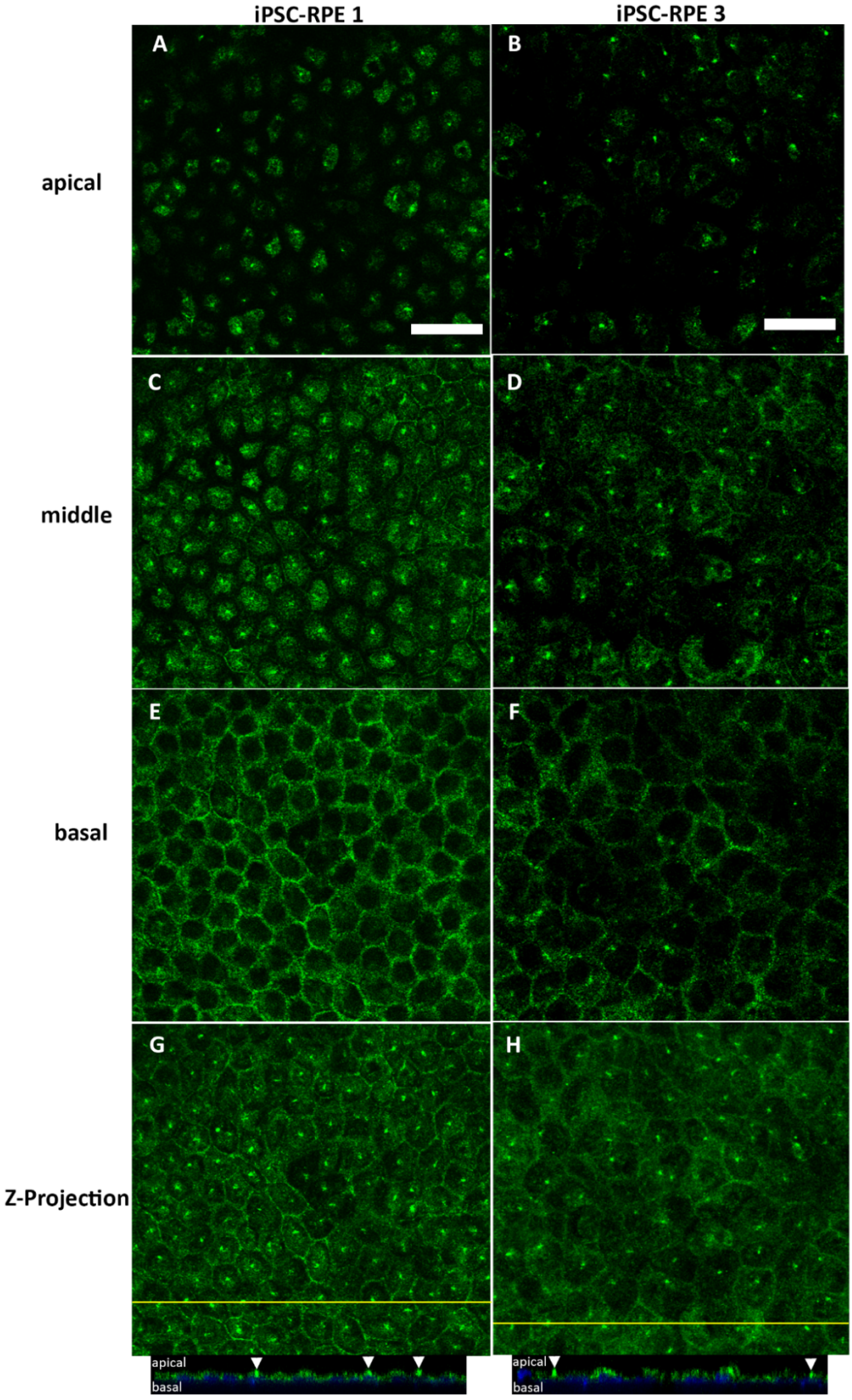
iPSC-RPE 1
iPSC-RPE 3
apical
middle
basal
Z-Projection
A
B
C
D
E
F
G
H
apical
basal
apical
basal

Figure 5.8: Alpha tubulin labeling in iPSC-RPE 1 (A, C, E, and G) and iPSC-RPE 3 (B, D, F, and H) showing the arrangement of microtubules in an apical region (A, B), middle region (C, D), and basal region (E, F) of the cells. The apical region is dominated by horizontally-oriented microtubules whereas the basal region consists mainly of vertically-oriented microtubules. Panels (G) and (H) show z-projections; z-planes at the locations of the yellow lines illustrate the presence of primary cilia (indicated by white arrowheads) on the apical surface of the iPSC-RPE cells. Scale bars in (A-H), 20 μm.

5.2.5 Transepithelial Resistance

The RPE is situated between the photoreceptors and the choriocapillaris, thereby serving as a blood-retinal barrier (Rizzolo, 2007). To perform such a function, the RPE forms tight junctions near its apical surface to tightly regulate the flux of ions, molecules, and fluid between the inner retina and the blood supply (Rahner et al., 2004). To test whether our iPSC-RPE expressed the proteins necessary to form these tight junctions, we cultured the cells on laminin-coated Transwell inserts and performed immunocytochemistry to examine the expression of tight junction proteins, including ZO-1, occludin, and claudin19. The immunostaining revealed that the cells, which have proper cortical arrangement of actin filaments (Figures 5.9A and 5.3C-D), expressed the three tight junction proteins, with normal localization at the plasma membrane (Figures 5.9B-D and 5.3E-H).

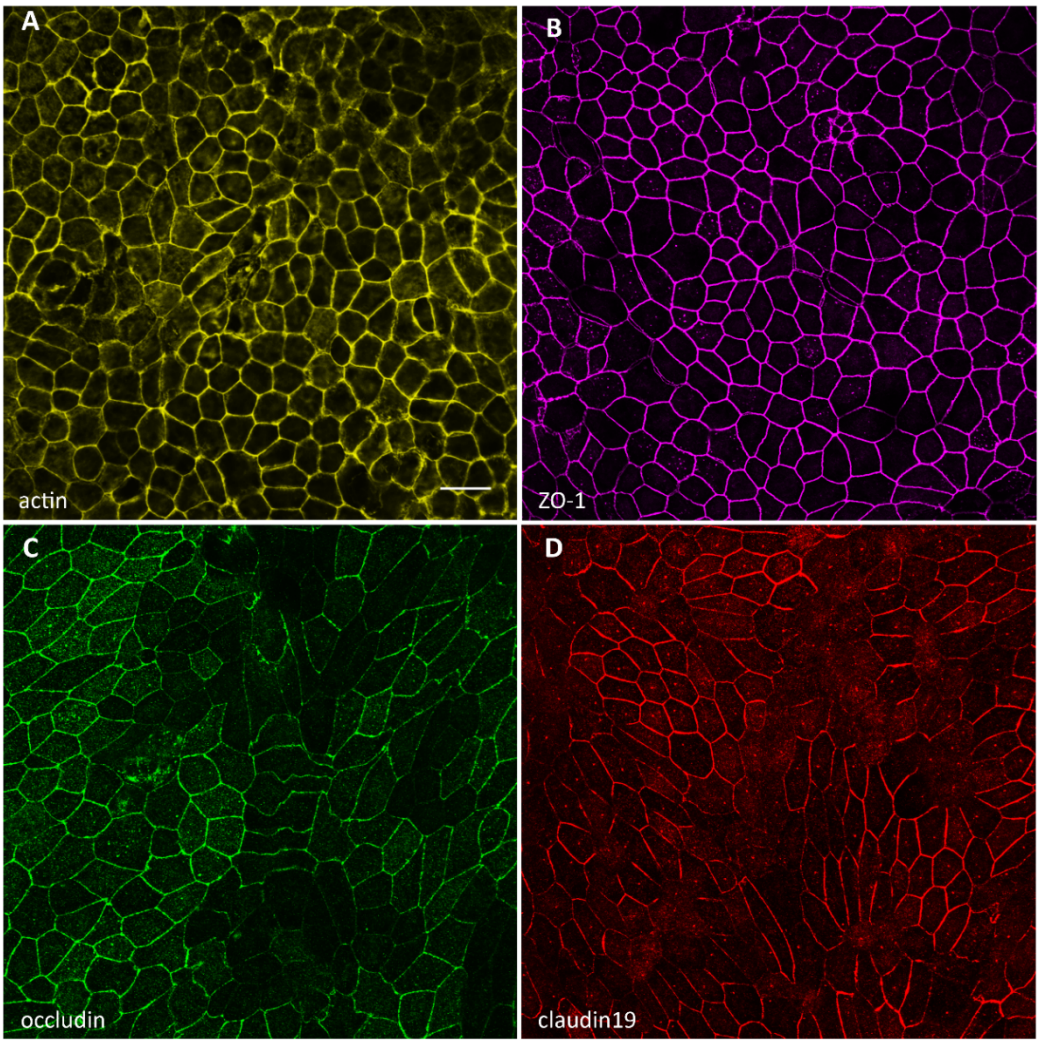
A
actin
B
ZO-1
C
occludin
D
claudin19

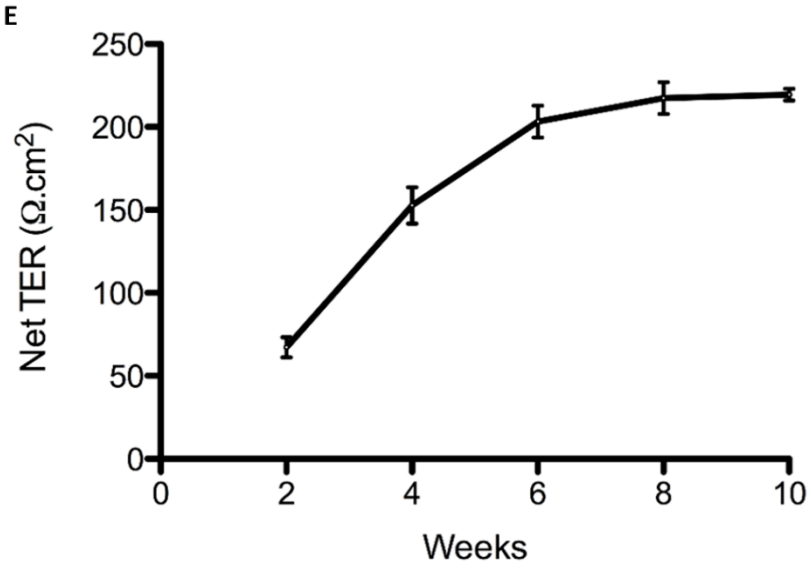
E
Net TER (Ω.cm²)
250
200
150
100
50
0
0
2
4
6
8
10
Weeks

Figure 5.9: Tight junction proteins and the transepithelial resistance of iPSC-RPE. RPE cells were cultured on laminin-coated Transwell inserts. (A) Phalloidin labeling demonstrates the cortical arrangement of actin filaments in iPSC-RPE. (B-D) Immunostaining of the iPSC-RPE revealed surface expression of the tight junction proteins, ZO-1 (B), occludin (C), and claudin19 (D). (E) To assess the barrier function of the iPSC-RPE, the resistance across monolayers of cells cultured on laminin-coated Transwell inserts was measured at two-week intervals, following initiation of the cultures. The net TER was determined by subtracting the resistance across a laminin-coated Transwell insert lacking cells, and multiplying by the surface area of the insert (0.33 cm^2). The net TER of the iPSC-RPE cells steadily increased between weeks 2 and 8, until it reached a maximal value of just above 200 $\Omega.cm^2$. Resistance recordings were made from four individual cultures. The error bars in E represent the mean ± the SEM. Scale bars: (A-D), 20 μm. Abbreviations: ZO-1, zonula occludens-1; TER, transepithelial resistance.

The resistance across the RPE layer provides a measure of the function of the tight junctions. To measure the TER, we cultured our iPSC-RPE cells on laminin-coated Transwell inserts, and made recordings at 2-week intervals. We observed a steady increase in the TER until it reached a maximal level of slightly above 200 $\Omega.cm^2$, by 8 weeks of culture (Figure 5.9E). This value is consistent with the reported net TER of human RPE in vivo, which ranges from 150 $\Omega.cm^2$ to 200 $\Omega.cm^2$ (Quinn and Miller, 1992; Sonoda et al., 2009; Ferrer et al., 2014). Collectively, the expression of tight junction proteins and the measured TER indicate that the iPSC-RPE cells are capable of establishing an appropriate epithelial barrier in vitro.

5.2.6 Integration of Human iPSC-RPE into the Murine RPE in vivo

Transplantation of healthy and functional RPE cells has the potential of treating an eye with diseased or dysfunctional RPE. To test for integration of iPSC-RPE cells into an RPE layer in vivo, we injected suspensions of RPE cells into the subretinal space of albino mouse eyes (Figure 5.10A). After various intervals, retinal cryosections were obtained, and fluorescently labeled with RHO antibodies and phalloidin for f-actin. Images of phase contrast merged with RHO and actin fluorescence revealed that the injected pigmented iPSC-RPE cells, delineated by the phalloidin labeling for actin, had integrated into the host retina, and were situated apical to the outer segments of the photoreceptors, marked by the RHO labeling (Figure 5.10B-E).

Additionally, the pigmented iPSC-RPE cells also contained phagosomes, derived from ingested ROSs, suggesting that the integrated cells were capable of performing phagocytosis (Figure 5.10B).

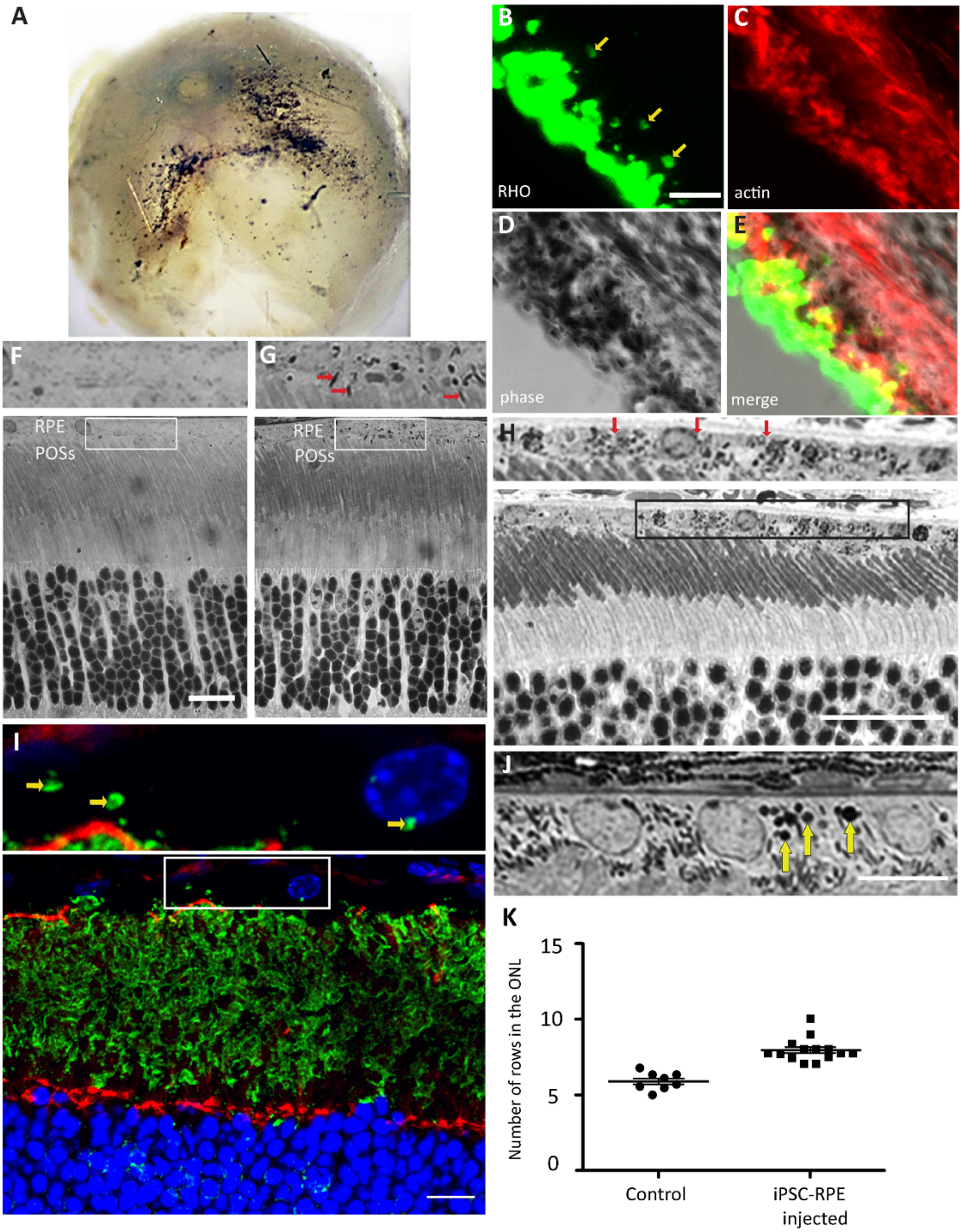

Figure 5.10: Transplantation of human iPSC-RPE into murine eyes. (A-H) Injection of pigmented human iPSC-RPE into the subretinal space of albino mouse eyes. In the examples illustrated, injections were performed at P14. (A) Posterior segment of a whole eye, 28 days after injection, showing evidence of pigment. (B-D) Thick retinal cryosection, 28 days after injection, labeled with anti-RHO (B), and phalloidin (C), and shown under phase contrast (D). (E) Merge of RHO and actin labeling, together with phase contrast imaging. RHO labels ROSs, as well as phagosomes in the RPE (yellow arrows in B; inner retina is lower left). Phalloidin labeling of f-actin delineates the apical RPE. Pigmentation in the RPE cells is evident by the phase contrast imaging. Pigmented RPE cells are therefore evident in the RPE layer, adjacent to the labeled ROSs, and contain ROS phagosomes. (F-H) Retinal semi-thin sections from a P40 non-injected albino mouse (control) (F), and from albino mice fixed 28 days (G), or 205 days (H) after injection. The boxed regions in the lower panels are shown at higher magnification in the upper panels. iPSC-RPE cells are identifiable by the presence of melanosomes in the apical processes (red arrows in G), adjacent to the tips of the POSs, in addition to the cell body. Pigmented iPSC-RPE cells (red arrows in H), remain integrated in the retina, 200 days post injection. (I-K) Injection of pigmented human iPSC-RPE into the subretinal space of *Mertk*$^{-/-}$ mouse eyes. In the examples illustrated, injections were performed at P10, and retinas were examined 27 days after injection, at P37. (I) Fluorescence micrograph of retinal section labeled with anti-RHO (green) and phalloidin (red). Nuclei were counterstained with DAPI. Yellow arrows in enlarged region (above) indicate RHO-positive phagosomes in transplanted iPSC-RPE cells. (J) Micrograph of toluidine blue-stained semi-thin section (yellow arrows indicate ROS phagosomes). (K) Quantification of photoreceptor nuclei in semi-thin sections of the central retina. For the data illustrated, injections were made with PBS (control) or iPSC-RPE cells (p = 0.0001) at P10, and sections were obtained 27 days later, at P37. For reference, the central region of a 1-2 month old WT retina contains ~10 rows of photoreceptor nuclei (e.g. (F)). Scale bars: (B-E), 5 μm; (F-H), 20 μm; (I) and (J), 10 μm.

Light microscopy on semi-thin sections from injected eyes confirmed the presence of melanosome-containing cells that were absent in non-injected eyes (Figure 5.10F, G). Following the longest interval post-injection that we tested, 205 days, these pigmented cells remained detectable in the retinas of injected albino eyes (Figure 5.10H). It is important to note that the melanosomes were evident in the apical processes of the RPE cells, in addition to the cell body (Figure 5.10G; red arrows). Localization to the apical processes, and with an orientation that is approximately parallel to that of the POSs, has been shown to require the molecular motor, myosin-7a, in mouse (Liu et al., 1998; Gibbs et al., 2004) and human (Gibbs et al., 2010) RPE, and demonstrates that the melanosomes are endogenous to the RPE cells. An alternative explanation for the presence of melanosomes in the RPE is that albino host cells ingested debris from the injected pigmented cells. While such ingestion can happen, it results in

the retention of the melanosomes only within vacuoles in the RPE (Engelhardt et al., 2012). These results confirm that a suspension of iPSC-RPE can be targeted to the outer retina, where the cells are capable of integrating into the host tissue, and can remain stable for a significant period of time after the injection procedure.

5.2.7 In vivo Rescue of Retinal Degeneration by iPSC-RPE

RPE dysfunction or pathology has been indicated in numerous forms of retinal degeneration, including retinitis pigmentosa, Best disease, Stargardt's disease, and AMD. It is therefore appealing to use iPSC-derived RPE for autologous transplantations to rescue RPE functions lost in some of these degenerative diseases. In our in vivo studies, we used the *Mertk* $^{-/-}$ mouse as a model of retinal degeneration, with RPE dysfunction, and tested whether our iPSC-RPE could rescue the inherent phagocytosis deficiency of the RPE.

We injected suspensions of 50,000 iPSC-RPE cells into the subretinal space of *Mertk* $^{-/-}$ mice at age P10, long before retinal degeneration has been observed to occur in this model. The animals were sacrificed 27 days post injection, and thick cryosections and semi-thin Epon sections were obtained from the retinas. The cryosections were stained with phalloidin to identify the apical region of the RPE, and an antibody against RHO to identify phagosomes of ROSs phagocytized by the RPE. In the semi-thin sections, phagosomes were identified by heavy staining with toluidine blue. MERTK functions in the ingestion of POSs by the RPE, so that the *Mertk* $^{-/-}$ RPE lacks phagosomes (Duncan et al., 2003), and the presence of numerous phagosomes in the RPE layer is an indicator of transplanted functional iPSC-RPE. Figure 5.10I shows phagosomes that have been identified by RHO immunolabeling. Figure 5.10J shows a cluster of toluidine blue-stained phagosomes (yellow arrows) in a semi-thin section of the RPE layer. The semi-thin sections were also used to quantify the number of rows of photoreceptor nuclei in the outer nuclear layer (ONL) of the central retina, near the injection site. This quantification showed that *Mertk* $^{-/-}$ mice injected with iPSC-RPE cells had more rows of nuclei

in the ONL, relative to non-injected mice (Figure 5.10K). Overall, these results demonstrate the ability of iPSC-RPE to rescue a lost function of the RPE, in vivo, and partial rescue of photoreceptor degeneration, in a mouse model of inherited retinal degeneration.

5.3 Materials and Methods

5.3.1 GMP Facility

Fibroblast derivation, iPSC generation, and RPE differentiation were performed in a GMP-compatible facility at the UCLA David Geffen School of Medicine as described (Karumbayaram et al., 2012). All cells used in this study were handled by qualified personnel. GMP-compatible protocols and procedures were followed. The facility and equipment, were routinely cleaned, calibrated, and monitored rigorously by contract vendors. All materials used were qualified according to the supplier certificate of analysis. Inventory records, and generation and distribution of materials, were documented.

5.3.2 Derivation of Fibroblasts

Pieces of skin biopsy (1 mm^2) were incubated with 1 mg/ml AOF Collagenase A (Worthington Biochemical; LS00415) for 1 h. Released cells were washed twice and plated on dishes, coated with CellStart™ (Gibco; A1014201), in Fibrogro™ medium (EMD Millipore; SCM037). Once confluent, the cells were passaged using TrypLE™ Select (Invitrogen; 12563-011), and their purity was determined by the proportion of cells expressing fibroblast cell markers. The cells were stable in culture for at least 5 passages.

5.3.3 Generation and Maintenance of iPSCs

The non-integrating vector used of reprogramming of fibroblasts to iPSCs was the modified, non-infectious, self-replicating Venezuelan Equine Encephalitis (VEE) virus RNA replicon RNA system from EMD Millipore (Cat # SCR550). This synthetic polycistronic RNA replicon has all four reprogramming factors on a single RNA strand, thereby eliminating the

need to transfect multiple individual mRNA, and increasing the reprogramming efficiency over DNA- and protein-based reprogramming methods. Briefly, fibroblasts were transfected with the vector, and selected with puromycin for 9-11 days in the presence of B18R protein (EMD Millipore; GF156). Removal of the B18R protein mediates the elimination of the RNA replicon system from the cultures. Selected cells were passaged onto Matrigel (BD; 354277) and allowed to grow for 3-4 weeks, during which time, iPSC colonies began to form. These colonies were picked and passaged to establish individual iPSC lines, which were subsequently maintained in culture under feeder-free conditions, using a 1:1 formulation of TeSR2 medium (Stem Cell Technologies; 05860) and NutriStem® medium (Stemgent; 01-0005). A bioinformatics assay for pluripotency, PluriTest, was performed by Cedars-Sinai. Karyotyping was performed by Cell Line Genetics.

5.3.4 Differentiation of iPSCs into RPE

RPE cells were differentiated from iPSCs, with modifications of a previously described method (Idelson et al., 2009). The iPSCs were cultured for 2 weeks as embryoid bodies (EBs), suspended in low-adherent dishes in basal medium, containing Dulbecco's Modified Eagle Medium: Nutrient Mixture F-12 (DMEM/F12; Invitrogen; 11330-032), supplemented with 14% xeno-free knockout serum (Invitrogen; 12618-013), 0.1 mM non-essential amino acids (NEAA) (Invitrogen; 11140-050), 2 mM GlutaMax™ (Invitrogen; 35050-061), and 10 mM nicotinamide (Sigma-Aldrich; N0636). The medium was changed every other day. Growth factors, including Activin A (140 ng/ml; Peprotech; 120-14P), transforming growth factor beta 1 (TGFB1; 2.5 ng/ml; Peprotech; AF-100-21C), and fibroblast growth factor 2 (FGF2; 20 ng/ml; Peprotech; 100-18B) were then added to the basal medium, and the EBs were allowed to grow and differentiate for an additional 2 weeks. The EBs were then returned to basal medium until pigmentation became evident. The pigmented regions in the EBs were separated by scalpel dissection, and plated as adherent cultures in RPE medium: DMEM/F12 with 5% fetal bovine

serum (FBS) (Omega Scientific; FB-12), 4% normal human AB serum (Innovative Research; IPLA-SERAB-HI), triiodothyronine (0.02 ng/ml; Sigma-Aldrich; T6397), hydrocortisone (0.02 µg/ml; Sigma-Aldrich; H0888), taurine (0.25 mg/ml; Sigma-Aldrich; T0625), 10 mM nicotinamide, 0.1 mM NEAA, 1X N1 (Sigma-Aldrich; N6530), 1X B27 (Invitrogen; A14867-01), 0.1 mM β-mercaptoethanol (Sigma-Aldrich; M3148), and GlutaMax™. Pigmented cells were passaged, following gentle collection with medium after 5-min TrypLE™ treatment. For the following analyses, RPE cells were cultured in RPE medium (as above, but lacking B27 and β-mercaptoethanol, and containing MEM alpha (Invitrogen; 32561-037) with 1% FBS), at 37 °C, and in 5% CO_2. For all experiments, iPSC-RPE cells were passaged 1-4 times beyond their derivation from the pigmented EBs, and unless otherwise stated, the results in the figures were obtained from iPSC-RPE line 2.

5.3.5 Immunocytochemistry

iPSC-RPE cells were seeded ($1.66 \times 10^5.cm^{-2}$) on Transwell inserts (Corning; 3470) or 12-mm glass coverslips, coated with laminin (Thermo Fisher; 23017015), and cultured for 6-8 weeks. Cultures were washed twice with phosphate-buffered saline (PBS), fixed with 4% formaldehyde in PBS for 10 min, washed with PBS, permeabilized with 0.25% Triton X-100, and then blocked with 4% bovine serum albumin (BSA) or 10% Normal Goat Serum (NGS) (Invitrogen; 50-062Z) in PBS for 1 h. They were immunolabeled for 1 h at room temperature in PBS, containing 1% BSA or 10% NGS, and antibodies against the following proteins: SOX2 (Santa Cruz Biotechnology; sc-17320), NANOG (EMD Millipore; AB9220), OCT4 (Cell Signaling Technology; #2840), fibroblast-specific protein-1 (FSP-1) (EMD Millipore; ABF32), vimentin (Abcam; ab92547), RPE65 (Abcam; ab67042), microphthalmia-associated transcription factor (MITF) (Abcam; ab20663), bestrophin 1 (BEST1) (Abcam; ab2182), zona occludens-1 (ZO-1) (Life Technology; 40-2200), occludin (Abcam; ab31721), claudin19 (Novus Biologicals; H00149461-M02), rhodopsin (RHO) (RHO pAb01 (Boesze-Battaglia et al., 1997; Liu et al.,

1999)), integrin $\alpha_V\beta_5$ (Abcam; ab24694), and MER proto-oncogene, tyrosine kinase (MERTK) (Novus Biologicals; NB110-57199). Following primary antibody incubation, cultures were washed 3 x 5 min, and incubated with Alexa Fluor-conjugated secondary antibodies (Invitrogen) for 1 h at room temperature, in the dark. Cultures were washed 3 x 5 min with PBS. Membranes of Transwell inserts were excised and mounted onto frosted microscope slides using Fluoro-Gel II mounting medium with 4, 6- diamino-2-phenylindole (DAPI) (Electron Microscopy Sciences; 17985-50) to counterstain the nuclei. Images were acquired with an Olympus FluoView 1000 confocal microscope, or a Zeiss Axiovert 200 M microscope.

5.3.6 Phagocytosis of Photoreceptor Outer Segments

Porcine eyes were obtained from a local slaughterhouse for the purification of photoreceptor outer segments (POSs), following a method used previously for bovine POS purification (Azarian et al., 1995). Briefly, retinas were isolated and homogenized under dim red light. The homogenate was then loaded onto a continuous (27%-50%) sucrose gradient to purify the POSs, which contain outer segments from rods (ROSs) and cones (COSs). The POSs were frozen in DMEM with 2.5% sucrose at -80 °C. For phagocytosis assays, the POSs were thawed at room temperature and incubated with iPSC-RPE on laminin-coated Transwell inserts (10 POSs/cell) for 2 h. After the POS challenge, cells were washed with PBS, containing 0.9 mM calcium and 0.49 mM magnesium (PBS-CM), and immediately processed for immunofluorescence (pulse), or incubated further before processing for immunofluorescence (chase).

A double immunofluorescence labeling strategy, using an antibody against RHO, was used to distinguish between ROSs bound to the surface of the iPSC-RPE cells and ROSs that have been internalized, as described (Gibbs and Williams, 2003; Esteve-Rudd et al., 2014). Briefly, cultures were fixed with 4% formaldehyde for 10 min, and blocked with 1% BSA in PBS-CM for 15 min. Surface-bound ROSs were labeled with the RHO pAb01, followed by an Alexa

Fluor 488-nm-conjugated goat anti-rabbit secondary antibody. After permeabilization with 50% ethanol in PBS-CM for 5 min, all ROSs were labeled with the same RHO antibody, followed by an Alexa Fluor 594-nm-conjugated goat anti-rabbit secondary antibody. Finally, cells were washed with DPBS-CM before the membranes of the Transwell inserts were excised and mounted onto microscopy slides. Confocal Z-stacks of randomly selected fields of view were acquired on an Olympus confocal microscope using a 60x NA1.4 oil objective. Surface-bound ROSs were labeled with both secondary antibodies, thereby appearing yellow. Internalized ROSs were labeled only with the Alexa Fluor 594-nm-conjugated secondary antibody, and therefore appeared red. For quantification, ROSs with a minimum diameter of 0.5 μm were counted from a total of 6-8 fields of view using imageJ software. Analysis of ROS degradation was performed by comparing the total number of ROSs after the 2h-pulse with the number after 2 h- and 5 h-chase periods.

5.3.7 Live-Cell Imaging

iPSC-RPE cells were plated on laminin-coated chambered coverglass (LabTek; Fisher Scientific; 155411), and allowed to polarize for 8 weeks. To label acidic organelles, including endolysosomes, the cells were incubated with RPE medium containing 100 nM LysoTracker Red DND-99 (Thermo Scientific; L7528) for 1 h at 37 °C. After washing to remove excess dye, fresh medium, containing 25 mM HEPES (Gibco; 15630-080), was added to the cells. Live-cell imaging was performed using an Ultraview ERS spinning disk with a Zeiss Axio Observer microscope, and an environmental chamber maintained at 37 °C. Movies were acquired with a 63x oil objective at 1.9 frames per second, using Volocity (PerkinElmer). The trajectories of labeled organelles were analyzed in the x- and y-dimensions, during a 20-40-second time period, using the Volocity and Imaris x64 (Bitplane) software.

5.3.8 Transepithelial Resistance Measurements

Transepithelial resistance (TER) was measured for iPSC-RPE cells cultured on laminin-coated Transwell inserts (growth surface area, 0.33 cm^2), using an $EVOM^2$ Epithelial Voltohmmeter (World Precision Instruments) with a STX2 electrode. Measurements were made within 3 min of removal from the incubator. The net TER was determined by subtracting the resistance across a laminin-coated Transwell insert, lacking cells, from measured values, and then multiplying by the surface area.

5.3.9 RNA Preparation and Expression Analysis

Total RNA from the iPSC-derived RPE was extracted using the RNeasy Mini Kit (Qiagen; 74104). RNA concentrations were measured using a Qubit fluorometer. Single-stranded cDNA was synthesized from 200 ng of total RNA, using Superscript IV and random hexamer primers (Fisher Scientific; N8080127) in a volume of 20 µl. The cDNA was used for semi-quantitative reverse transcription-polymerase chain reaction (RT-PCR) analysis. PCR reactions were performed using GoTaq® Flexi DNA polymerase (Promega; M829). Thermal cycling conditions were performed as follows: one cycle at 94 °C for 300 s; 30 cycles at 94 °C for 30 s, 60 °C for 30 s, and 72 °C for 30 s; one cycle at 72 °C for 300 s. The sequences of primers used for the PCR include: *RPE65* (5'_TCCCCAATACAACTGCCACT_3'; 5'_CCTTGGCATTCAGAATCAGG_3'), *MERTK* (5'_TCCTTGGCCATCAGAAAAAG_3'; 5'_CATTTGGGTGGCTGAAGTCT_3'), *BEST1* (5'_TAGAACCATCAGCGCCGTC_3'; 5'_TGAGTGTAGTGTGTATGTTGG_3'), and *GAPDH* (5'_ACCACAGTCCATGCCATCAC_3'; 5'_TCCACCACCCTGTTGCTGTA_3') (Kamao et al., 2014).

5.3.10 Western Blot Analyses

Cells were lysed in RIPA-I lysis buffer (Fisher Scientific; 89900) with added protease inhibitor cocktail (Roche; 11836153001). Protein concentrations were estimated using a Qubit fluorometer (~30 µg protein was applied to each lane). Proteins were transferred to Immobilon

PVDF membranes (EMD Millipore; IPVH00010), which were blocked with TBS with 0.05% Tween 20 (Sigma-Aldrich; P9416) and 5% skimmed milk for 30 min, and then probed with anti-RPE65. HRP-conjugated secondary antibodies were visualized by enhanced chemiluminescence (GE-Healthcare; RPN2232).

5.3.11 Subretinal Injections

iPSC-RPE cells were injected into the subretinal space of *Mertk* $^{-/-}$ mice (129 genetic background) and BALB/cJ albino mice. Cultures of iPSC-RPE cells were washed thoroughly with PBS before enzymatic dissociation with TrypLE™. BSS PLUS™ (Alcon Laboratories; 0065080050) was added to create a suspension at a concentration of 50,000 cells/µl. Mice (postnatal day (P) 10-16) were anesthetized by isoflurane inhalation. Their pupils were dilated with a drop of 1% (w/v) Atropine Sulfate ophthalmic solution (Akorn Pharmaceuticals; 17478-215-02), and the corneas were kept moist with Hypromellose ophthalmic demulcent 2.5 % solution (Wilson Ophthalmic Corp; 51394-315-15). A 1-µl suspension of iPSC-RPE was injected into the subretinal space of each eye, under a Zeiss Stemi 2000 microscope, as described (Engelhardt et al., 2012). Ophthalmic ointment (Neomycin & Polymyxin B sulfates and Dexamethasone; Falcon Pharmaceuticals; 61314-631-36) was applied to each eye, immediately following injection. Cyclosporine (200 mg/l; Novartis; 0078-0109-61) was added to the drinking water of the dam from 1 day prior to the injection until the pups were weaned at P28. Mice were kept on a 12-hour dark/12-hour light cycle. For experiments concerning phagosomes, they were killed between 15 and 30 min after lights-on.

5.3.12 Microscopy

For fluorescence microscopy, eyes were fixed, embedded in OCT, cryosectioned, and immunolabeled as described (Jiang et al., 2015). Semi-thin sections were prepared for light microscopy by fixation and Epon-embedment, as described (Jiang et al., 2015).

5.3.13 Statistical Test

GraphPad Prism 7 and Microsoft Excel were used to perform statistical analyses. The data was represented by the mean ± the standard deviation or standard error of the mean. A two-tailed Student t-test was used to determine if there was a significant difference in photoreceptor nuclei counts between control vs. iPSC-RPE-injected eyes. A $p \leq 0.05$ was considered statistical significant.

5.4 Discussion

Numerous in vitro cell models have been used to study basic human RPE cell biology, including primary cultures from donor tissues, and immortalized cell lines, such as ARPE-19, d407, and hTERT-RPE1 (Davis et al., 1995; Dunn et al., 1996). Although RPE cultures from human fetal tissue do mimic in vivo characteristics well (Hu and Bok, 2001; Maminishkis et al., 2006), their supply is limited, and a large supply of isogenic cell cultures is not feasible. On the other hand, RPE cultures from immortalized cell lines have been reported to fall short of in vivo characteristics, including signature gene expression, robust TER, structural polarity, and functional aspects such as kinetics of POS phagosome degradation (Finnemann et al., 2002; Strunnikova et al., 2010; Lehmann et al., 2014; Mazzoni et al., 2014). Many of these limitations have been mitigated by using human pluripotent stem cells to obtain RPE cells in large quantities for cell culture studies as well as therapeutic transplantation. Here, we have advanced the use of iPSC-RPE cells by a GMP-compatible method of iPSC generation, coupled with novel analyses of critical cell biological functions.

RPE cells were one of the first cell types to be isolated from pluripotent stem cells, due to their readily discernible pigmentation (Kawasaki et al., 2002), and a variety of protocols have been developed to improve and hasten this process (Idelson et al., 2009; Buchholz et al., 2013; Gong et al., 2015; Maruotti et al., 2015). Some of these protocols have generated RPE cells from integration-free iPSCs (Leach et al., 2016; Saini et al., 2017) as these cells are more likely

to be free of mutations due to the reprogramming process, and are therefore better candidates for transplantation purposes. Here, we have used GMP-compatible conditions to differentiate RPE from iPSCs that have been generated using integration-free reprogramming, and demonstrated that the iPSC-RPE cells possessed key characteristics that will likely be essential to their function in clinical uses.

Cultures of iPSC-RPE cells have been characterized with respect to gene expression, the presence of selected protein markers, and some functional assays (Kokkinaki et al., 2011; Kamao et al., 2014). An extensive recent study focused on ATP-dependent, RPE physiology (Miyagishima et al., 2016). The particular focus in the present study has been on aspects of RPE cell biology that are critical for retinal health. By week 7 of the differentiation process, we observed robust expression of signature RPE proteins, including BEST1, RPE65, and MITF. At that time, the cytoskeleton of the cells resembled that of an epithelium, with actin filaments organized at the cortex, and microtubules arranged horizontally in the apical cell body and vertically throughout the cell body (Bacallao et al., 1989; Bre et al., 1990; Gilbert et al., 1991; Meads and Schroer, 1995). The epithelial arrangement of the cytoskeleton was underscored by our live-cell imaging analysis, in which 8-week cultures of iPSC-RPE cells exhibited lateral and vertical motility of endolysosomes. The observed intracellular motility is a critical indicator of RPE cell health. Each RPE cell in the human retina must efficiently degrade phagosomes derived from 30 POSs on a daily basis (Volland et al., 2015). Defects in motor proteins that drive organelle motility in the RPE have been shown to compromise phagosome degradation, and lead to retinal pathology, including symptoms of AMD, which is potentially the most significant target disease of RPE transplantation (Gibbs et al., 2003; Jiang et al., 2015).

In addition, the iPSC-RPE cells showed both normal expression and localization of tight junction proteins, including ZO-1, occludin, and claudin19, by week 7 of the differentiation (Peng et al., 2011; Stanzel et al., 2014). This was reflected functionally by the TER of the cultures,

which by week 7 had reached 200 $\Omega.cm^2$. Finally, by week 8 of the differentiation process, we observed surface localization of the receptors integrin $\alpha_v\beta_5$ and MERTK, which participate in the binding and ingestion of POSs, respectively (Lin and Clegg, 1998; D'Cruz et al., 2000). These receptors were shown to be functional in assays that demonstrated the phagocytosis of POSs by iPSC-RPE cells, with kinetics comparable to that in vivo.

These results support the use of iPSC-RPE cells for in vitro studies of pathogenicity in RPE disease. In addition, a clinically-relevant goal for RPE cells derived from iPSCs is to be able to transplant these cells into patients with maculopathies, where RPE dysfunction or dystrophy contributes to the overall pathology. The RPE can be transplanted as either an intact sheet of cells or as a suspension of dissociated cells (Schwartz et al., 2012; Sugita et al., 2016). A major concern with the suspension method is that the cells may not integrate properly in order to perform their function. Here, we demonstrated that a suspension of iPSC-RPE cells can integrate into the host RPE monolayer, and is capable of partially rescuing a critical function of the RPE that has been compromised due to a genetic defect. The ability of iPSC-RPE cells to rescue the pathology associated with certain maculopathies is likely to be dependent on the quality of the RPE cells that are used. In this study, we placed a special emphasis on characterizing the highly-sensitive cell biological characteristics of iPSC-RPE cells, such as intracellular trafficking, to obtain well differentiated cultures suitable for transplantation.

Chapter 6

Rapid Differentiation of the Human RPE Cell Line, ARPE-19, Induced by Nicotinamide

6.1 Introduction

The retinal pigment epithelium (RPE) is a single monolayer of cells that resides between the light-sensitive photoreceptors and the fenestrated choriocapillaris. It performs specific functions in support of the photoreceptor cells, such as the reisomerization of visual chromophore, and phagocytosis of photoreceptor outer segment (POS) membrane (Strauss, 2005). The importance of the RPE for proper vision is underscored by several retinal degenerative diseases that involve RPE pathology, including age-related macular degeneration (AMD) (Bhutto and Lutty, 2012).

Due to the scarcity of donor eyes, primary human RPE cells are in limited supply. Moreover, these primary cultures exhibit significant heterogeneity among cultures from different donors (Burke et al., 1996; Kuznetsova et al., 2014). In addition to donor eyes, human RPE cells can be derived from embryonic and induced pluripotent stem cells (Idelson et al., 2009; Buchholz et al., 2013; Hazim et al., 2017). Although the RPE cells differentiated from stem cells have been shown to exhibit native RPE characteristics, the differentiation process is costly and time-consuming. Furthermore, stem cell-derived RPE cells have been found to lose their polarized organization and RPE functions after only a few passages in culture (Singh et al., 2013a). Hence, human RPE cell lines continue to provide an important source, with the ARPE-19 line being the most commonly used; in recent years, there have been ~170 papers published annually that specifically mention ARPE-19 cells in the title or abstract (PubMed search for ARPE-19 or ARPE19).

When first reported, standard cultures of the ARPE-19 cell line readily exhibited many of the characteristics of well-differentiated RPE cells, including cobblestone morphology, apical-

basal polarity, and expression of RPE-specific proteins (Dunn et al., 1996). However, after two decades of passaging, such well-differentiated cultures no longer form with the commonly-used culture methods. The cells typically exhibit incomplete execution of the epithelial polarity program (Rodriguez-Boulan and Macara, 2014), thus compromising their ability to represent in vivo biology. We describe here a significantly-improved method to culture ARPE-19 cells that are currently commercially available. It involves culture in medium with supplements including nicotinamide (referred to as MEM-Nic hereafter), and selective trypsinization to generate a homogeneous cell population. The requirement for nicotinamide demonstrates the importance of metabolism in differentiation of the cells.

6.2 Results

6.2.1 Cobblestone Morphology

ARPE-19 were thawed and cultured in DMEM/F12 with GlutaMAX, 10% certified FBS, and 1% Penicillin/Streptomycin until the culture vessel was 95-100% confluent. For medium comparison studies, the cells were passaged and cultured in a 6-well tissue culture plate (seeding density, 1.66×10^5 cells.cm^{-2}) or on a Transwell filter insert (at the same density) in one of the following media: **(1) DMEM/F12** (DMEM/F12, 1% FBS, and 1% Penicillin/Streptomycin); **(2) DMEM + pyruvate** (DMEM with high glucose (4.5 g/l), 1 mM pyruvate, and 1% Penicillin/Streptomycin); **(3) MEM-Nic** (MEM alpha with GlutaMAX, 1% FBS, 1% Penicillin/Streptomycin, 1% N1 supplement, taurine (83 mg/ml), hydrocortisone (20 µg/ml), triiodo-thyronin (13 ng/ml), and 10 mM nicotinamide). The cells were maintained at 37 °C, 5% CO_2, and fed three times per week.

First, we examined the gross morphology of ARPE-19 cells in two standard media commonly used to culture these cells and compared them with those cultured in MEM-Nic. As a simple epithelium, RPE forms a single monolayer with cobblestone appearance. After one week

in culture on a plastic tissue culture plate, with either of the standard media, the ARPE-19 cells formed a disorganized monolayer with fibroblast-like morphology, as evident by bright-field microscopy. In contrast, the cells cultured in MEM-Nic formed a monolayer of mostly epithelial-like cells, exhibiting cobblestone morphology (Figure 6.1A). When grown on Transwell inserts (as describe in the next section) for one week, and examined by immunofluorescence of zona occludens-1 (ZO-1), which labels the periphery of the cells, a comparable difference was evident (Figure 6.1B). After an extended period in culture, we observed improvements in the organization of ARPE-19 cultures in the two standard media, with the appearance of a cobblestone-like morphology after > 2 months, but still not to the extent of cells after one week in culture with MEM-Nic.

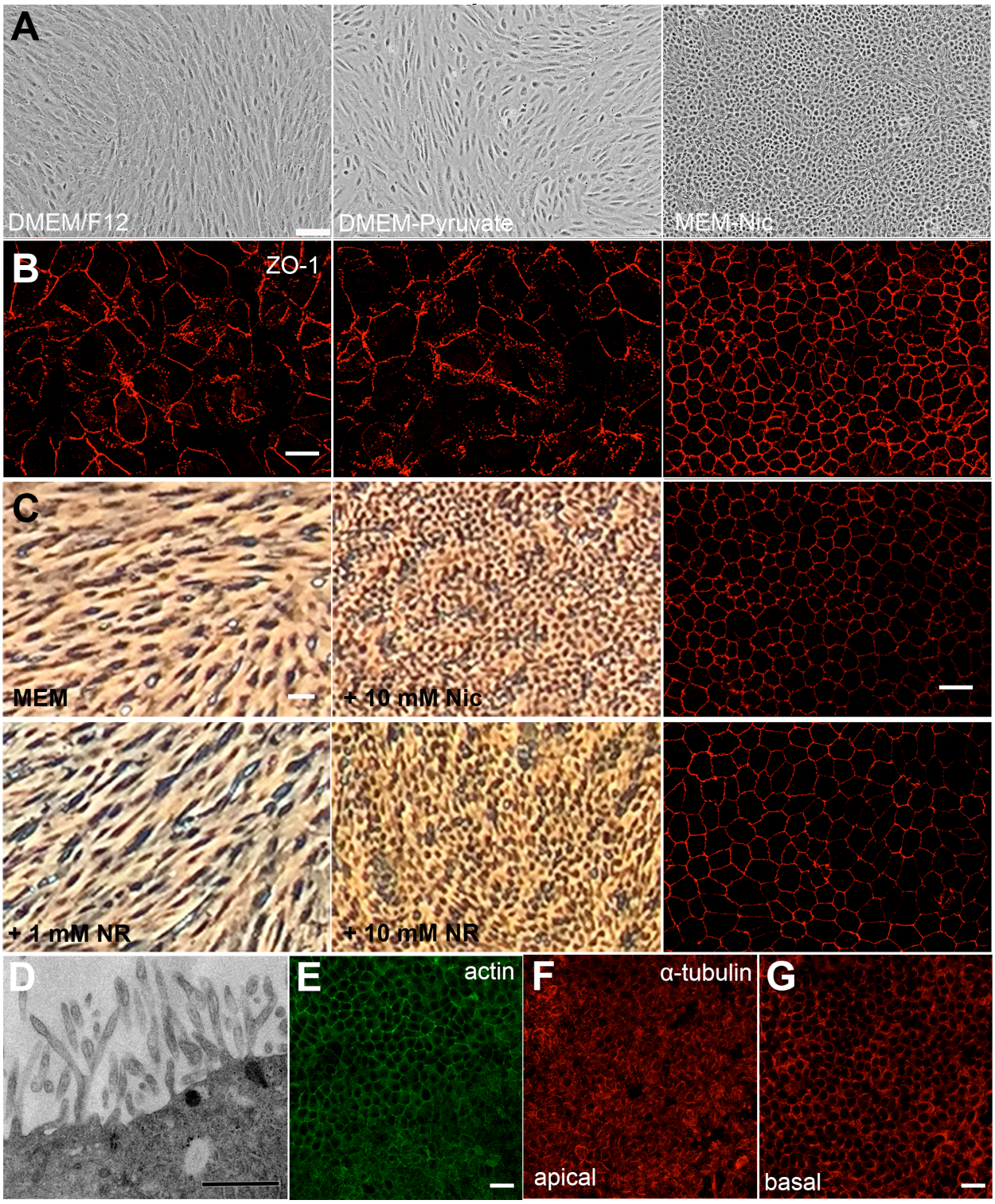

Figure 6.1: Cellular morphology of differentiated ARPE-19 cells. (A) Brightfield micrographs of ARPE-19 cells differentiated on plastic surfaces for one week in standard media (DMEM/F12 or DMEM-Pyruvate) or in MEM-Nic medium. (B) Immunofluorescence micrographs of ZO-1 in ARPE-19 cells differentiated on Transwell inserts for one week in the media mentioned above. Only cells differentiated in MEM-Nic medium show cobblestone morphology. (C) Nicotinamide is

necessary for the differentiation of ARPE-19 cells. Brightfield micrographs of ARPE-19 cells plated at the same density and cultured for two weeks in MEM-Nic medium without nicotinamide (but with other supplements to the MEM), with 1 mM or 10 mM NR instead of nicotinamide in MEM-Nic, or with 10 mM nicotinamide (i.e. MEM-Nic). Cobblestone morphology can only be observed in medium containing 10 mM NR or 10 mM nicotinamide. (D-G) ARPE-19 cells differentiated on Transwell inserts for 2-3 weeks in MEM-Nic medium. (D) TEM micrograph shows numerous microvilli emanating from the apical surface of ARPE-19 cells. (E) Phalloidin labeling of apical section shows actin filaments in the apical microvilli (lower) and the slightly less apical circumferential ring (upper). (F and G) Single plane confocal microscopy of α-tubulin immunolabeling revealed horizontal microtubules in apical region (f) and vertical microtubules in the basal region (G) of polarized ARPE-19 cells. Scale bars: (A and C), 100 μm; (B, E, and G), 20 μm; (D), 0.5 μm. NR, nicotinamide riboside. All images are representative of ≥ 3 experiments.

6.2.2 Role of Nicotinamide in ARPE-19 Cell Differentiation

Given the role that nicotinamide has been shown to play in the differentiation of RPE from pluripotent stem cells (Idelson et al., 2009; Maruotti et al., 2015; Saini et al., 2017), we tested the necessity of nicotinamide in the MEM-Nic medium for the morphological phenotype we observed. We thus compared cultured ARPE-19 cells in the presence or absence of nicotinamide, or a nicotinamide-related compound, nicotinamide riboside (NR). Brightfield micrographs revealed that, in MEM-Nic without nicotinamide (but with the other supplements), the cells failed to acquire cobblestone morphology, and instead remained fibroblastic in shape. They also showed that the addition of 10 mM NR was approximately as effective as 10 mM nicotinamide in inducing the rapid differentiation of ARPE-19 cells (Figure 6.1C). The cobblestone arrangement of ARPE-19 cultures, grown on Transwell inserts in MEM with 10 mM Nic or 10 mM NR, is evident by ZO-1 immunofluorescence (Figure 6.1C, right panels).

As a member of the vitamin B3 family, nicotinamide has been implicated to play a central role in cellular metabolism. In particular, it serves as a precursor for the production of NAD^+, $NADP^+$, and other substrates that participate in metabolic pathways, including the TCA cycle, and the mitochondrial electron transport chain (Jang et al., 2012). Interestingly, many of the key enzymes and coenzymes in these metabolic pathways have been shown to become

upregulated as cells differentiate into their terminal fate (Shyh-Chang et al., 2013; Hu et al., 2016). Nicotinamide has been shown to protect against oxidative stress and maintain mitochondrial health (Gomes et al., 2013; Mitchell et al., 2018), while its related compound, NR, was demonstrated to promote oxidative metabolism by means of increasing the NAD^+/NADH ratio (Canto et al., 2012). Interestingly, there is evidence to suggest that oxidative stress, and in particular reactive oxygen species, can promote epithelial-to-mesenchymal transition (Rhyu et al., 2005; Wang et al., 2010).

6.2.3 Culture on Permeable Transwell Inserts

Transwell culture systems provide a permeable support for epithelial cells that promotes their differentiation in vitro into a polarized state by establishing distinct apical and basal compartments. To generate homogenous polarized monolayers, ARPE-19 cells differentiated in MEM-Nic for two weeks in plastic vessels were subjected to three 10-minute treatments with TrypLE, a recombinant trypsin substitute. The TrypLE was discarded after each 10-min treatment, releasing weakly-adherent fibroblastic cells, approximately 5% of cells in the cultures, leaving behind the firmly attached epithelial cells. This method of selective trypsinization generates a homogenous population of cobblestone cells in subsequent cultures. Following the last treatment of TrypLE, the remaining cells were harvested in MEM-Nic (by gentle pipetting) and the suspension was passed through a 40-µm cell strainer (BD Falcon) to ensure the absence of cell clumps. Cells were then counted on a hemocytometer and plated on laminin-coated (10 $\mu g.cm^{-2}$) Transwell inserts at a density of 1.66×10^5 $cells.cm^{-2}$ in MEM-Nic. The cells were fed three times per week by replacing 100 µl of medium in the apical compartment and 600 µl in the basal compartment of each Transwell insert.

6.2.4 Characterization of the Apical Microvilli and the Cytoskeleton

Differentiated ARPE-19 cells grown on Transwells were prepared for transmission electron microscopy (TEM), and fixed by removing the culture medium and replacing it with primary fixative, 2% formaldehyde and 2.5% glutaraldehyde (EM grade from Electron Microscopic Sciences) in 0.1 M sodium cacodylate buffer. Cells were fixed for 20 min, before the Transwell membrane was excised with a scalpel and quickly placed in 0.1 M sodium cacodylate buffer, in which they were washed (3x5 min). The cells were then post-fixed for 20 min with 1% osmium tetroxide in 0.1 M sodium cacodylate buffer and thoroughly washed (3x5 min) in 0.1 M sodium cacodylate buffer. Samples were then gradually dehydrated in increasing levels of ethanol (30-90%) for 5 min each. Dehydration concluded with three, 5-min washes in 100% ethanol. Finally, cells were rinsed 3x5 min in propylene oxide and infiltrated with increasing concentrations of Araldite 502 resin (Electron Microscopic Sciences, Hatfield, USA), starting with 2 parts propylene oxide to 1 part resin for 20 min, followed by 1 part propylene oxide to 2 parts resin for 20 min, and ending with 2 successive incubations in pure resin for 20 min each. Cells were then embedded in flat molds and polymerized in an oven at 60 °C for 48 h. Ultrathin sections were collected on copper mesh grids and contrast stained with 5% uranyl acetate in ethanol and 0.4% lead citrate.

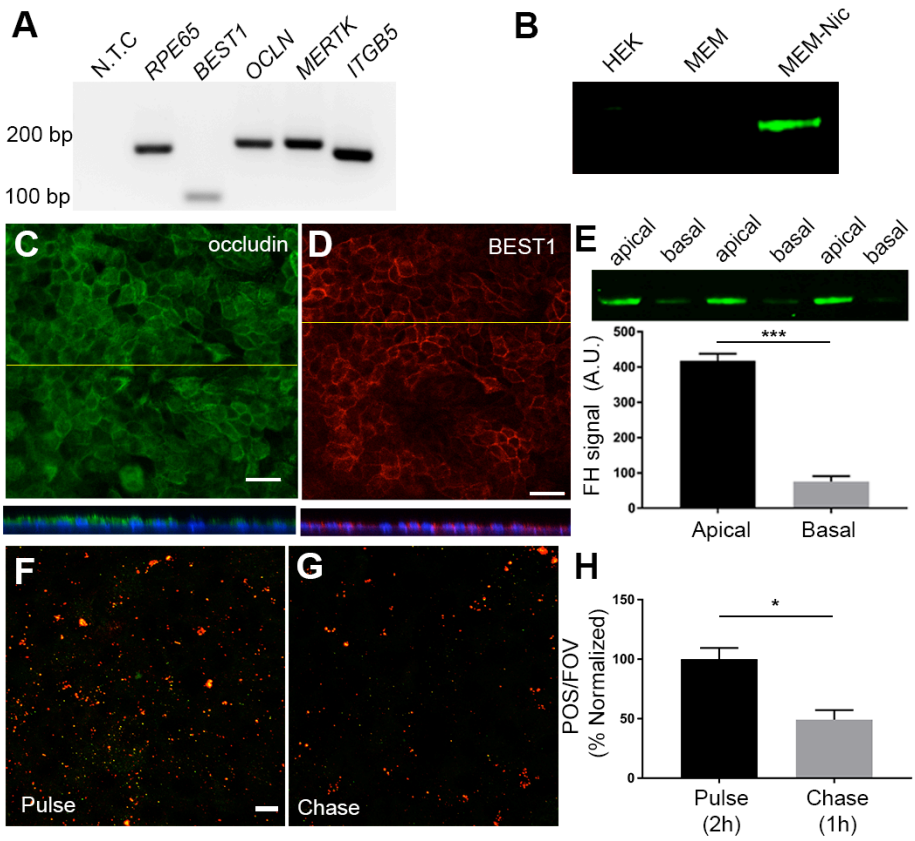

Figure 6.2: Expression profile and functional assessment of differentiated ARPE-19 cells. (A) RT-PCR shows expression of RPE-specific and RPE-related genes. (B) Western blot revealed expression of RPE65 in ARPE-19 cells differentiated in MEM-Nic for 4 weeks; the protein is undetectable in HEK cells and ARPE-19 cells differentiated in MEM without nicotinamide. (C and D) Fluorescence micrographs of ARPE-19 cells differentiated on Transwell inserts for 3 weeks show expression and polarized localization of occludin (C; apical due to tight junction localization) and BEST1 (D; basolateral surface). The nuclei are counterstained with DAPI in the z-planes (taken at the yellow lines) underneath each panel. (E) Western blot revealed the presence of CFH in serum-free medium conditioned by differentiated ARPE-19 cells for 48 h. Quantification of band intensity showed significantly more CFH present in the apical medium relative to the basal medium. Equal volume samples from three different cultures are shown. (F and G) Micrographs of opsin-labeled ARPE-19 cells (before and after cell permeabilization) differentiated on Transwell inserts, challenged with porcine POS for 2 h and fixed immediately (F; pulse) or fixed after a 1-h chase period (G). Surface-bound POS appear in yellow whereas internalized POS appear in red. (H) Quantification of total POS revealed a significant decrease after the 1-h chase relative to the pulse, indicating degradation of ingested POS at a rate comparable to that in vivo. Scale bars: (C and D), 20 μm; (F), 10 μm. N.T.C, no template control; HEK, human embryonic kidney cells; FOV, field of view. All images are representative of ≥ 3 experiments. Error bars in (E and H) represent ± S.E.M. *** P = 0.0002; * P = 0.015.

For immunofluorescence, cells cultured on Transwell inserts were washed twice with Dulbecco's phosphate buffered saline (DPBS; Fisher Scientific) and fixed with 4% formaldehyde in DPBS for 10 min. Following 3 washes with DPBS, the cells were permeabilized with 0.25% Triton X-100, and then blocked in DPBS containing 5% normal goat serum and 1% BSA for 1 h. The cells were then incubated for 1 h at RT in DPBS containing 1% BSA and one or a combination of primary antibodies. Following the primary-antibody incubation, the cells were washed 3x5 min, and incubated with appropriate Alexa Fluor-conjugated secondary antibodies and, in some instances, Phalloidin-TRITC (Sigma-Aldrich) for 1 h at RT in the dark. The cells were washed 3x5 min with DPBS, and the membranes of the Transwell inserts were excised and mounted on frosted microscope slides using Fluoro-Gel II mounting medium with DAPI (Electron Microscopy Sciences) to counterstain the nuclei. Images were acquired on a confocal microscope (FluoView 1000, Olympus) with FluoView FV10-ASW 3.1 software.

Electron microscopy revealed the presence of microvilli emanating from the apical surface of differentiated ARPE-19 cells (Figure 6.1D). Fluorescence microscopy demonstrated an epithelial-like arrangement of cytoskeletal elements. Phalloidin labeling revealed actin filaments in the apical RPE, with a circumferential ring at the level of the cell-cell junctions (Figure 6.1E). By immunolabeling, we also observed that apically-located microtubules were horizontal (Figure 6.1F) while those found more basally were vertically-oriented (Figure 6.1G). In addition to these classes of microtubules, immunolabeling with antibodies specific for acetylated α-tubulin indicated the presence of cilia at the apical surface of the cells (Figure 6.3).

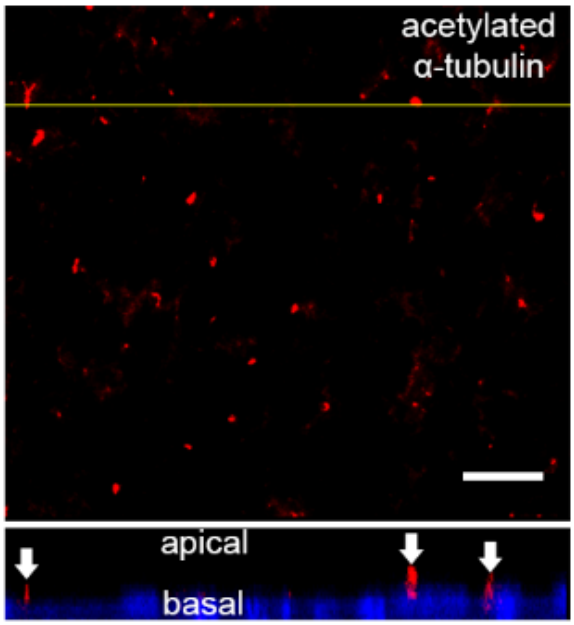

Figure 6.3: Differentiated ARPE-19 cells possess apically-oriented cilia. Fluorescence micrograph of acetylated α-tubulin revealed the presence of primary cilia. Below the micrograph is a z-plane taken at the yellow line and showing cilia (indicated by white arrows) emanating from the apical region of the cells. The nuclei are counterstained with DAPI. Scale bar: 10 μm.

Because these cytoskeletal elements support actin-based (myosins) and microtubule-based (dyneins and kinesins) motility, they play an essential role in organelle trafficking and protein sorting. In epithelial cells, the spatial organization of microtubules, in addition to their associated motors, have been shown to be critical for the polarized targeting of secretory vesicles, as well as the machinery of the endocytic pathway (Gilbert et al., 1991; Musch, 2004). The ARPE-19 cells differentiated by our method establish a polarized epithelial cell model that can be used to investigate general epithelial processes, including secretory and endocytic vesicular transport, as well as RPE-specific processes such as the trafficking of phagosomes and the degradative organelles that are necessary for their clearance (Wavre-Shapton et al., 2014; Jiang et al., 2015; Esteve-Rudd et al., 2018).

6.2.5 Expression of RPE Genes

Total RNA was harvested from ARPE-19 cells differentiated on plastic for 2 weeks using Qiagen RNeasy Plus Mini Kit (cat # 74134) following the manufacturer's protocol. Single-strand cDNA was synthesized from 2 µg of total RNA using the SuperScript III First-Strand Synthesis Kit (Invitrogen). PCR was performed using Taq PCR Premix (Bioland Scientific). Thermal cycling conditions were as follows: one cycle at 95 °C for 5 min; 40 cycles at 95 °C for 15 s, 60 °C for 15 s, and 72 °C for 20 s; and one cycle at 72 °C for 5 min.

To test for the expression of RPE-signature genes, we probed for *RPE65*, encoding an essential retinoid isomerase required for the visual cycle function, bestrophin 1 (*BEST1*), encoding an RPE-specific protein localized to the basolateral surface, occludin (*OCLN*), encoding a tight junction component, and *MERTK* and integrin β5 (*ITGB5*), encoding critical receptors for the phagocytosis of photoreceptor outer segment disk membranes. RT-PCR revealed that two-week cultures of ARPE-19 cells in MEM-Nic detected the expression of all these genes (Figure 6.2A).

6.2.6 Protein Expression, Localization, and Secretion

SDS-PAGE was performed to separate 20 ug of proteins (denatured at 95 °C for 5 min) from whole-cell lysates on a 4-12% bis-tris gradient gel. Proteins were transferred onto PVDF membrane using semi-dry transfer. Membranes were blocked with Odyssey blocking buffer (LI-COR) for 1 h at RT to prevent non-specific binding of the antibodies. For RPE65 detection, the membrane was incubated with rabbit anti-RPE65 (pin 5) in Odyssey buffer containing 0.1% Tween-20 overnight at 4 °C. The signal was detected by incubating the membrane with goat anti-rabbit IRDye 800CW secondary antibodies in Odyssey buffer with 0.1% Tween-20 and 0.01% SDS for 1 h at RT. For Factor H detection in ARPE-19 conditioned medium, samples were collected from the apical and basal compartments of Transwell inserts (six times more volume was collected from the basal compartment relative to the apical compartment to account

for the medium volumes used when culturing the cells). The samples were heated at 70 °C for 10 min before being separated on a 4-12% bis-tris gradient gel. The transfer and blocking steps were performed as described above. The membrane was incubated with goat anti-FH for 2 h at RT followed by an incubation with donkey anti-goat IRDye 800CW secondary antibodies. Blots were imaged using the Odyssey CLx Imaging System (LI-COR) and processed using Image Studio Lite Ver5.2 software.

Western blotting confirmed the expression of RPE65 protein (Figure 6.2B). After 3 weeks of differentiation, properly localized occludin (Figure 6.2C) and BEST1 (Figure 6.2D), were detected at the apical and basolateral surfaces, respectively. Taken together, these data show that ARPE-19 cells can be rapidly differentiated such that their expression of some key RPE proteins compares to native RPE.

Demonstration of polarity in differentiated ARPE-19 cells was evident in the vectorial secretion of complement factor H. The RPE is a local source of Factor H in the retina, and the gene (*CFH*) is one of the two very high-risk genes for AMD (Edwards et al., 2005; Haines et al., 2005). Serum-free media conditioned by ARPE-19 cells differentiated on Transwell inserts for 48 h was collected from the apical and basal compartments of the inserts and tested for Factor H using western blotting. The results demonstrated significantly more Factor H present in the apical medium relative to the basal medium (Figure 6.2E), suggesting that the protein is secreted in a polarized manner, similar to that observed in vivo. This observation is consistent with immunofluorescence data showing Factor H localization on the apical surface of human fetal RPE cultured on Transwell inserts (Kim et al., 2009b).

6.2.7 Isolation of Porcine Photoreceptor Outer Segments

Fresh porcine eyes were obtained from a local slaughterhouse and kept on ice at all times. POS were isolated using a previously published protocol for isolation of bovine POS

(Azarian et al., 1995), with a few modifications. Briefly, the retinas were isolated from eyecups under dim red light and homogenized with a Teflon glass pestle. The homogenate was then loaded onto a continuous (27-50%) sucrose gradient and centrifuged at 26,000 *g* for 1 h at 4 °C. Following centrifugation, the POS settle in a band on the gradient, easily identifiable due to its orange/pink color. The band containing the POS was collected, diluted three times in Ringer solution (130 mM NaCl, 3.6 mM KCl, 2.4 mM $MgCl_2$, 1.2 mM $CaCl_2$, 10 mM HEPES, and 0.02 mM EDTA, pH 7.4) and centrifuged at 10,000 *g* for 10 min at 4 °C. The POS were counted under a hemocytometer and stored in DMEM with 2.5% sucrose at -80 °C for subsequent experiments. POS were stored frozen. Immediately prior to use they were thawed at RT and centrifuged at 2,400 *g* for 5 min. The POS were then suspended in DMEM, and FBS was added at 10% final concentration.

6.2.8 Phagocytosis of Photoreceptor Outer Segments and Degradation of Phagosomes

To test the functionality of differentiated ARPE-19 cells, we focused on an essential function of the RPE, phagocytosis of POS. Frozen POS were thawed at RT and centrifuged at 2,400 *g* for 5 min. The POS were then suspended in DMEM, and FBS was added at 10% final concentration. Differentiated ARPE-19 cells cultured on Transwell inserts were then challenged with 100 µl of POS suspension (~7.5 x 10^7 POS/ml) for 2 h at 37 °C, 5% CO_2. After the POS challenge, cells were extensively washed with DPBS containing 0.9 mM calcium and 0.49 mM magnesium (DPBS-CM), and immediately processed for immunofluorescence (pulse; Figure 6.2F) or returned to the 37 °C incubator for 1 h (chase; Figure 6.2G) before being processed for immunofluorescence.

A previously described double immunofluorescence labeling strategy (Hazim and Williams, 2018) was used to distinguish between POS bound to the surface of the ARPE-19 cells and POS that have been internalized. Briefly, the cells were fixed with 4% EM-grade

formaldehyde (Electron Microscopy Sciences) for 10 min and blocked with blocking buffer (1% BSA in DPBS-CM) for 15 min. Surface-bound POS were then labeled with the pAb01 rabbit anti-opsin antibodies diluted in blocking buffer for 10 min followed by an Alexa Fluor 488 nm-conjugated goat anti-rabbit secondary antibodies for 30 min in the dark. The cells were then permeabilized with 50% ethanol for 5 min at RT. Total POS were labeled with the same opsin antibody followed by an Alexa Fluor 594 nm-conjugated goat anti-rabbit secondary antibody for 1 h at RT. Finally, cells were washed with DPBS-CM before the membranes of the Transwell inserts were excised and mounted onto frosted microscope slides using Fluoro-Gel II mounting medium with DAPI. Confocal Z-stacks of ≥ 3 randomly selected fields of view were acquired on an Olympus confocal microscope.

Surface-bound POS were labeled with both secondary antibodies, thereby appearing yellow in color. The internalized POS were labeled post-cell permeabilization with the Alexa Fluor 594 nm-conjugated secondary antibody and therefore appear red in color. For quantification, POS ≥ 0.5 μm in diameter were counted from each field of view using imageJ software. Quantification of opsin-positive particles revealed that the cells were capable of binding, ingesting, and degrading POS-derived phagosomes at a rate comparable to that of primary RPE cells (Figure 6.2H).

6.2.9 Statistical Analysis

Data were analyzed using a two-tailed Student's t-test. For CFH secretion, n = 3 separate cultures of ARPE-19 cells, with apical and basal components for each. For the phagocytosis assay, n = 3 randomly selected fields of view for both the pulse and chase conditions; each field of view contained ≥ 100 cells. Calculations were performed using GraphPad Prism 7 and Microsoft Excel software.

6.3 Materials and Methods

6.3.1 Cell Culture Components

Dulbecco's Modified Eagle Medium (DMEM)/F12 with GlutaMAX, Minimum Essential Medium (MEM) Alpha, certified-grade fetal bovine serum (FBS; US origin), nonessential amino acids (NEAA), TrypLE Express Enzyme (1X), and Penicillin/Streptomycin were obtained from Thermo Fisher Scientific (Waltham, MA). The N1 supplement, taurine, hydrocortisone, triiodo-thyronin, and nicotinamide were obtained from Sigma-Aldrich (St. Louis, MO). ARPE-19 cells were obtained from ATCC (Lot Number 63478793; Manassas, VA) at their currently advertised passage number of 19, cultured on T75 flasks or 6-well tissue culture plates, and differentiated on Transwell inserts with polyester membrane (6.5-mm diameter, 0.4-μm pores) from Corning Costar (St. Louis, MO), and coated with natural mouse laminin (Thermo Fisher Scientific).

6.3.2 Antibodies

The primary antibodies used for immunocytochemistry included: rabbit anti-ZO-1 (Invitrogen 402200), rabbit anti-occludin (Abcam ab31721), mouse anti-BEST1 (Abcam ab2182), mouse anti-α-tubulin (Sigma-Aldrich T9026), and mouse anti-acetylated α-tubulin (Sigma-Aldrich T6793). The secondary antibodies used were goat anti-mouse and goat anti-rabbit IgG conjugated to Alexa Fluor 488 or 594 (Life Technologies). For western blotting, the antibodies used included: rabbit anti-RPE65 (pin 5) (Wenzel et al., 2005) (gift from Andreas Wenzel) and goat anti-FH (Quidel A312).

6.3.3 RT-PCR Primers

For RT-PCR, the sequences of primers used include: *RPE65*, 5' – GATCTCTGCTGCTGGAAAGG – 3' and 5' – TGGGGAGCGTGACTAAATTC – 3'; *BEST1*, 5' – CCCGAAAATCACCTCAAAGA – 3' and 5' - GCTTCATCCCTGTTTTCCAA – 3'; *OCLN*, 5' – GGAGGACTGGATCAGGGAAT – 3' and 5' – TCAGCAGCAGCCATGTACTC – 3'; *MERTK*, 5' –

AGACTTCAGCCACCCAAATG – 3' and 5' – GGGCAATATCCACCATGAAC – 3'; and *ITGB5*, 5' – CGGGGACAACTGTAACTGCT – 3' and 5' – ACGCAATCTCTCTTGGTGCT – 3'.

The primers used for *BEST1*, *OCLN*, and *ITGB5* span exon-exon junctions as to avoid amplification of genomic DNA. The primers used for *RPE65* and *MERTK* could theoretically generate products from genomic DNA. However, this is unlikely, given that such amplicons would be larger than 7 kb.

6.4 Limitations

6.4.1 Low Trans-Epithelial Resistance in Differentiated ARPE-19 Cells

Trans-epithelial resistance (TER) was measured for differentiated ARPE-19 cells cultured on laminin-coated Transwell inserts using an EVOM^2 Epithelial Voltohmmeter (World Precision Instruments) with a STX2 electrode, as described previously for RPE cell cultures from iPS cells (Hazim et al., 2017). All measurements were made inside a biosafety cabinet within 3 minutes of cell removal from the incubator. The net TER was determined by subtracting the resistance across a laminin-coated Transwell insert without any cells from measured values, and multiplying by the growth surface of the Transwell insert (0.33 cm^2).

In comparison to RPE cells in vivo or primary culture, ARPE-19 cell cultures have invariably been reported to possess a relatively low TER, a measure of the barrier function of the epithelium. Even with the original ARPE-19 cultures, Dunn et al. (Dunn et al., 1996) reported TER values of 34 Ohms.cm^2 in DMEM/F12 medium. In DMEM-Pyruvate, 51 Ohms.cm^2 was reported (Ahmado et al., 2011). In MEM-Nic, we measured 40 Ohms.cm^2 after 6 weeks, which is comparable to these published values and still relatively low.

6.4.2 Lack of Pigmentation

Although the premelanosome marker, Pmel17, has been detected in ARPE-19 cells (Ahmado et al., 2011), electron micrographs of normal RPE melanosomes have never been shown. Nonetheless, a lack of pigmentation is usually considered an advantage when working with fluorescence, which is readily quenched by melanin (especially in green and shorter wavelengths).

6.4.3 Abnormal Karyotype

The immortalization of the ARPE-19 cell line occurred spontaneously, and in a recent study, it was shown that different sources of the cell line exhibited abnormal karyotypes. Interestingly, attempts to generate clonal lines with normal karyotype failed because those cells undergo cellular senescence. To test for major chromosomal aberrations in ARPE-19 cells used in this study, cells (p17) were passaged onto a T-25 flask at 50-70% confluency, and shipped to Cell Line Genetics for karyotyping.

Cytogenetic analysis of 20 G-banded metaphase cells revealed an abnormal karyotype, most notably, a loss of one copy of chromosome 15, and an unbalanced translocation between the chromosome 15q and 19q (Figure 6.4). The karyotype of our cells was similar to that reported by Fasler-Kan et. al. (2018) (Fasler-Kan et al., 2018). Despite these chromosomal aberrations, our study shows that the cells can still be differentiated into an RPE-like state.

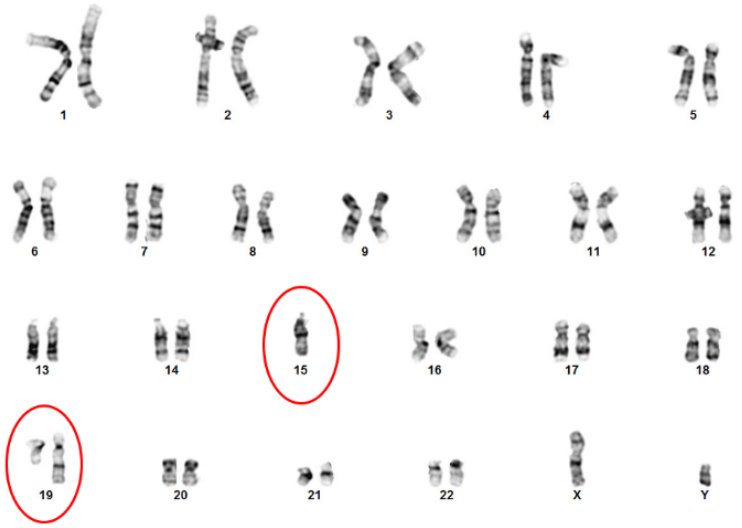

Figure 6.4: Karyotype analysis of G-banded metaphase chromosomes from ARPE-19 cells shows monosomy of chromosome 15, and an unbalanced translocation between the long arms of chromosomes 15 and 19 (red ellipsoids).

Chapter 7

Conclusions from the Present Studies

In this body of work, I have investigated a number of critical aspects of the RPE in relations to normal cellular biology and pathology. I particularly focused on the essential phagocytic function of the RPE, by which this supportive monolayer of cells in the retina binds, internalizes, and degrades the distal tips of the photoreceptor outer segments, thereby maintaining photoreceptor health and therefore proper vision. In the first two studies, I described two methods by which to test the kinetics of the process of phagocytosis using an in vitro cell culture model; one of these methods utilized spinning disk confocal microscopy to study the trafficking of phagosomes in live cultures of RPE cells. These two methods proved to be essential for investigating the RPE dysfunction observed in a mouse model of human Stargardt 3 macular degeneration.

As the mutation in Stargardt 3, which affects the *ELOVL4* gene, truncates the protein and leads to its mislocalization from the endoplasmic reticulum to the photoreceptor outer segment, it was hypothesized that the protein ends up in the RPE via phagocytosis of abnormal outer segment-derived phagosomes. Using live-cell imaging of normal RPE cells fed *ELOVL4*-mutant outer segments, I demonstrated that the resultant phagosomes have impaired motility, including reduced speed and less productive movements. The motility of phagosomes has been shown to be crucial for their degradation, as they are dependent on interactions with degradative organelles, including lysosomes and endosomes, to be efficiently cleared by the RPE. Furthermore, I also demonstrated that the impaired motility of mutant phagosomes in normal RPE cells is, in part, due to their abnormal association with the dynein motor protein. This observed defect in phagocytosis by the RPE may be a critical component in the retinal pathology that ultimately leads to photoreceptor degeneration.

The molecular and cellular mechanistic insights into RPE dysfunction in the Stargardt 3 mouse model underscore the value of RPE cell culture models. To that end, I have investigated the differentiation of human RPE cells from two sources, including induced pluripotent stem cells, and the immortalized human RPE cell line, ARPE-19. This differentiation process involves rearrangement of the cellular cytoskeleton, which results in a cobblestone epithelial-like morphology, polarization of intracellular and secreted proteins, and the capability to phagocytize photoreceptor outer segments. RPE derived from induced pluripotent stem cells, once extensively characterized as shown in Chapter 5, can be useful for future studies aiming to model retinal diseases involving RPE dysfunction, if obtained from human patients suffering from a particular blinding disease. For example, these cells can be derived from AMD patients and used to establish a disease-in-a-dish model where the role of CFH, a protein highly associated with the disease, in RPE pathology can be tested. As a complementary model, ARPE-19 cells, when differentiated using the method described in Chapter 6, can be quite useful to investigate RPE cellular processes, including organelle trafficking and homeostasis.

In summary, the aspects of the RPE investigated in this dissertation highlight cellular characteristics and processes that are essential for normal physiology. These aspects are further emphasized when they become awry, thereby compromising RPE function and overall retinal health. Thus, they must be under careful consideration if we are to gain a deeper understanding of the physiology of this supportive cellular monolayer in the retina, and to develop effective treatments that can potentially halt or reverse blinding diseases.

Appendix

Gene Therapy Approaches for Prevention of Retinal Degeneration in Usher Syndrome

The accessible and immune-privileged environment of the eye makes it ideal for gene therapy. It has been 8 years since successful gene therapy was first reported for patients with an inherited form of progressive retinal degeneration (RD), Leber Congenital Amaurosis (LCA2), following treatment in one eye with AAV2-*RPE65* (Bainbridge et al., 2008; Hauswirth et al., 2008; Maguire et al., 2008). Now, Bennett *et al.* have reported improved vision without adverse effects, such as immunogenicity, following treatment of the second eye with AAV2-*RPE65*, in children with LCA2 (Bennett et al., 2016). These results strongly support the use of *in situ* gene therapy in patients who can be treated prior to the onset of RD.

Paramount to this approach is the early identification of patients, before the retina has undergone any irreversible changes. While most forms of RD are detected only after significant retinal pathogenesis, Usher syndrome types 1 and 2 present congenital deafness that facilitates genetic identification of the disease in infancy; Usher 1 patients are born profoundly deaf, and Usher 2 patients are insensitive to high frequencies (Kimberling and Moller, 1995). Nowadays, the deafness can be treated with cochlear implants, and genetic testing of deaf infants is used to identify Usher syndrome and thus predict ensuing RD.

The first retinal gene therapy studies with Usher genes were carried out using lentiviral (LV) delivery of *MYO7A*, the gene responsible for Usher syndrome 1B (USH1B). MYO7A is present in both the photoreceptor and retinal pigment epithelial (RPE) cells (Liu et al., 1997) (Figure 1A). Injection of LV-*MYO7A* into the subretinal space of *Myo7a*-deficient mice was found to correct mutant phenotypes in both these cell types (Hashimoto et al., 2007). A phase I/II clinical trial, using LV-*MYO7A* to treat RD in USH1B, has been under way since 2012 (https://clinicaltrials.gov/ct2/show/NCT01505062).

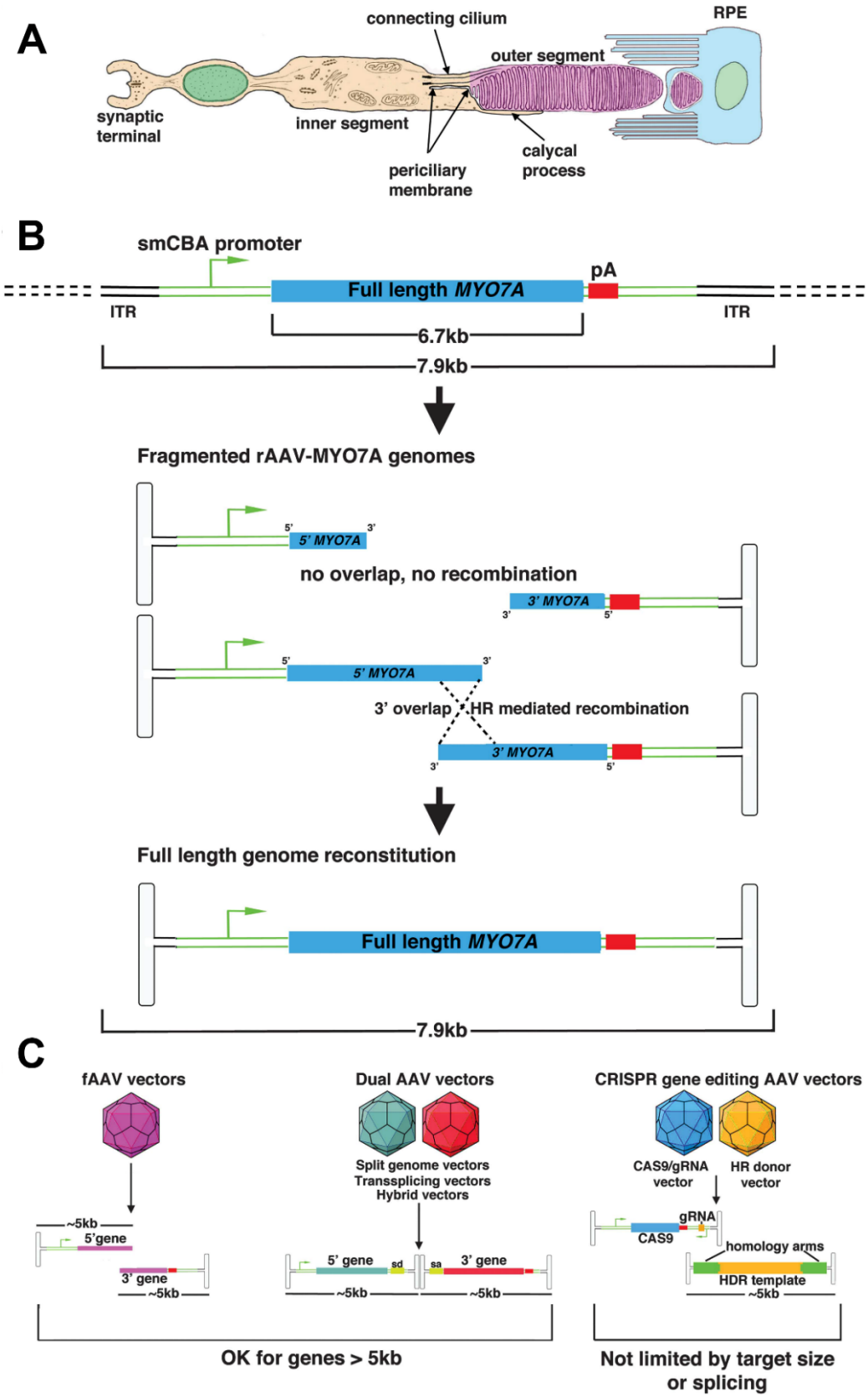
A
connecting cilium
RPE
outer segment
synaptic terminal
inner segment
calycal process
periciliary membrane
B
smCBA promoter
pA
Full length MYO7A
ITR
ITR
6.7kb
7.9kb
Fragmented rAAV-MYO7A genomes
5' MYO7A
no overlap, no recombination
3' MYO7A
5' MYO7A
3' overlap
HR mediated recombination
3' MYO7A
Full length genome reconstitution
Full length MYO7A
7.9kb
C
fAAV vectors
~5kb
5'gene
3' gene
~5kb
Dual AAV vectors
Split genome vectors
Transsplicing vectors
Hybrid vectors
5' gene
sd
sa
3' gene
~5kb
~5kb
CRISPR gene editing AAV vectors
CAS9/gRNA vector
HR donor vector
gRNA
CAS9
homology arms
HDR template
~5kb
OK for genes > 5kb
Not limited by target size or splicing

Figure 1: (A) Diagram of a photoreceptor cell and an RPE cell. Most Usher proteins are associated with the connecting cilium or periciliary membrane. Usher 1 proteins are also present in calycal processes. However, the Usher 1B protein, MYO7A, is most abundant in the RPE. (B) Schematic illustrating an overview of large genome fragmentation and subsequent full-length genome reconstitution for the AAV2-*MYO7A* fAAV vector (HR, homologous recombination; ITR, inverted terminal repeat; pA, polyadenylation signal; smCBA, small chicken beta-actin promoter). (C) Examples of AAV vector-mediated approaches for gene therapy, resulting from defects in large, very large or alternatively spliced genes (SD = splice donor, SA = splice acceptor, HDR = homology-directed repair).

Because the *MYO7A* coding sequence is 6.7 kb, it was thought that a viral vector such as LV was needed for delivery, since it features a larger carrying capacity than the reported maximum of 5 kb for adeno-associated virus (AAV). However, more recently, it was found that use of AAV, including AAV2, as used in the LCA2 treatments, mentioned above, resulted in WT levels of MYO7A and correction of retinal phenotypes in mutant mice (Allocca et al., 2008; Lopes et al., 2013; Trapani et al., 2014).

A significant body of research has now demonstrated that oversized AAV genomes can be packaged into high titer AAV as 5' truncated sense and anti-sense genomes, termed fragmented vectors (fAAV). The truncated genomes are efficiently reassembled, with high fidelity, into the full transgene product following transduction of target cells, as a result of recombination that is biased towards homologous recombination (HR) rather than non-homologous end joining (NHEJ) (Dong et al., 2010; Hirsch et al., 2010; Wu et al., 2010) (Figure 1B). Oversized gene replacement therapy, using fAAV expressing *MYO7A* cDNA, not only demonstrated reconstitution of the intact transgene product in vivo, but also reported more reliable phenotypic correction of the underlying mutation than a dual AAV vector expression system (Lopes et al., 2013). Similar success was also reported for fAAV expressing a 7.5-kb dysferlin transgene (Hirsch et al., 2013). Recently, an optimized dual vector system was shown to be comparable to fAAV vectors in a mouse model of Stargardt's RD (Trapani et al., 2015). There is an ongoing debate over which AAV system is the best for delivery of large transgenes

(Ghosh et al., 2011; Hirsch et al., 2013; Trapani et al., 2014). However, it is likely that many factors, including the transgene sequence and the epigenetic and transcriptional state of the target tissue will influence the success of each approach.

Despite the promise of gene augmentation therapy for genetic RDs, this approach is not amenable for a gene whose functional cDNA is very large or which expresses multiple essential isoforms. All the Usher genes have been reported to express multiple isoforms, although their relative importance in the human retina is unknown (Table 1). The expression of two major isoforms of *MYO7A* in the human retina (Weil et al., 1996) is a concern for the current USH1B clinical trial, which is using the single cDNA that was generated in the original mouse studies (Hashimoto et al., 2007). This isoform corrects mouse retinal phenotypes (Hashimoto et al., 2007; Lopes et al., 2013), but the relative isoform expression may differ between mouse and human retinas.

Direct targeting of genetic mutations can overcome these limitations. Recently, antisense oligonucleotides (ASOs) were used to correct a splice-site mutation in *CEP290*, a large gene defective in another form of LCA, and whose protein, like most of the Usher proteins, functions in the photoreceptor cilium (Garanto et al., 2016). Similarly, ASOs were used to target a cryptic splice site in the orthologue of *USH1C*, thereby rescuing hearing and vestibular functions in a mouse model for USH1C (Lentz et al., 2013). ASOs are limited, however, to diseases amenable to repair by blocking translation or a specific splice site.

Other mutations can potentially be repaired by gene editing strategies, including the clustered, regularly interspaced, palindromic repeats (CRISPR)-associated (Cas) system, which has revolutionized the field of genomic engineering since its introduction (Cong et al., 2013). Adapted from the microbial immune system, this technology uses a short guide RNA to target the Cas endonuclease to a specific locus in the genome. The Cas endonuclease can then

generate double-stranded breaks in the DNA, which can be repaired by one of two mechanisms: (1) NHEJ, an error-prone process that often results in insertions or deletions, or (2) homology-directed repair (HDR), which requires a repair template to introduce modifications to the targeted genetic locus (Yang et al., 2014). NHEJ occurs at a higher frequency while HDR is more suitable for repairing mutations.Recent RD studies demonstrated correction of *rd1* via CRISPR-mediated HDR of mutant mouse zygotes (Wu et al., 2016), and allele-specific ablation of a dominant mutant allele of *Rho* by CRISPR-mediated NHEJ with neonatal mice (Bakondi et al., 2016).

Viral delivery of CRISPR-Cas components offers high transduction efficiency, limited only by the size of the donor HDR template with respect to viral capacity (see above). HDR is currently also limited by its low efficiency, especially in post-mitotic cells (Ran et al., 2013). Nonetheless, the observation that an oversized AAV genome is regenerated in vivo by photoreceptor and RPE cells (Lopes et al., 2013; Trapani et al., 2014) indicates the presence of HDR in these cell types (Dong et al., 2010; Lai et al., 2010; Wu et al., 2010), and corroborates previous work demonstrating HDR in developed adult photoreceptors (Chan et al., 2011).

One strategy to help overcome limitations of HDR is to take advantage of different classes of CRISPR-Cas systems. For example, unlike the commonly used Cas9, the endonuclease Cpf1 generates staggered cuts with 5' overhangs (Zetsche et al., 2015). The resulting cleavage could mediate the insertion of a DNA fragment to correct a mutation by NHEJ, the more dominant repair mechanism.

Novel innovations in the field of gene editing will provide opportunities to optimize gene repair for RDs, however a genetic model with well-characterized cellular phenotypes would be useful to test and optimize the efficiency of gene editing. Among RDs, the cellular phenotypes resulting from loss of MYO7A in mutant mouse retinas have been particularly well

characterized. These phenotypes, such as melanosome localization in the RPE (Liu et al., 1998) and opsin concentration in the proximal photoreceptor cilium (Liu et al., 1999), can be scored on a cell-by-cell basis (Jacobson et al., 2008; Lopes et al., 2013), thus giving a direct readout of efficiency, making them potentially useful in optimization studies.

In conclusion, because patients with Usher syndrome are typically identified before RD begins, they are particularly suitable for gene therapy approaches. Preclinical tests are needed to determine if only one isoform is essential to prevent RD; in this case, all but 2 or 3 of the largest genes would appear suitable for augmentation by AAV, fAAV or dual AAV vector delivery of a single cDNA. Subtypes that are associated with a very large gene (USH2A and 2C) or more than one essential retinal isoform represent appropriate candidates for testing AAV vectors in the context of new gene editing strategies (Table 1; Figure 1C).

Table 1. Usher syndrome genes that are large or alternatively spliced

USH Subtype	Gene	Number of Isoforms	Length (amino acids)	Reference
USH1B	*MYO7A*	2[a]	2175, 2215	(Weil et al., 1996)
USH1C	*USH1C*	3 classes[a,c]	Up to 899	(Nagel-Wolfrum et al., 2011)
USH1D	*CDH23*	3 classes[b,c]	Up to 3354	(Lagziel et al., 2009)
USH1F	*PCDH15*	3 classes[a,c]	Up to 1955	(Ahmed et al., 2008)
USH1G	*SANS*	2[b]	358, 461	
USH1J	*CIB2*	3[b]	Up to 210	(Riazuddin et al., 2012)
USH2A	*USH2A*	2[a]	Up to 5202	(van Wijk et al., 2004)
USH2C	*GPR98*	3[a]	Up to 6306	(Weston et al., 2004)
USH2D	*WHRN*	3[b]	Up to 907	(Ebermann et al., 2007)
USH3A	*CLRN1*	11[a]	Up to 245	(Vastinsalo et al., 2011)

[a]Expressed in the human retina.

[b]Total number expressed in human; the number in the retina is not known.

[c]Each class represents multiple isoforms.

References

Agbaga, M.P., R.S. Brush, M.N. Mandal, K. Henry, M.H. Elliott, and R.E. Anderson. 2008. Role of Stargardt-3 macular dystrophy protein (ELOVL4) in the biosynthesis of very long chain fatty acids. *Proc Natl Acad Sci U S A*. 105:12843-12848.

Agbaga, M.P., B.M. Tam, J.S. Wong, L.L. Yang, R.E. Anderson, and O.L. Moritz. 2014. Mutant ELOVL4 that causes autosomal dominant stargardt-3 macular dystrophy is misrouted to rod outer segment disks. *Invest Ophthalmol Vis Sci*. 55:3669-3680.

Ahmado, A., A.J. Carr, A.A. Vugler, M. Semo, C. Gias, J.M. Lawrence, L.L. Chen, F.K. Chen, P. Turowski, L. da Cruz, and P.J. Coffey. 2011. Induction of differentiation by pyruvate and DMEM in the human retinal pigment epithelium cell line ARPE-19. *Invest Ophthalmol Vis Sci*. 52:7148-7159.

Ahmed, Z.M., S. Riazuddin, S. Aye, R.A. Ali, H. Venselaar, S. Anwar, P.P. Belyantseva, M. Qasim, S. Riazuddin, and T.B. Friedman. 2008. Gene structure and mutant alleles of PCDH15: nonsyndromic deafness DFNB23 and type 1 Usher syndrome. *Hum Genet*. 124:215-223.

Allikmets, R., N. Singh, H. Sun, N.F. Shroyer, A. Hutchinson, A. Chidambaram, B. Gerrard, L. Baird, D. Stauffer, A. Peiffer, A. Rattner, P. Smallwood, Y. Li, K.L. Anderson, R.A. Lewis, J. Nathans, M. Leppert, M. Dean, and J.R. Lupski. 1997. A photoreceptor cell-specific ATP-binding transporter gene (*ABCR*) is mutated in recessive Stargardt macular dystrophy *Nat Genet*. 15:236-246.

Allocca, M., M. Doria, M. Petrillo, P. Colella, M. Garcia-Hoyos, D. Gibbs, S.R. Kim, A. Maguire, T.S. Rex, U. Di Vicino, L. Cutillo, J.R. Sparrow, D.S. Williams, J. Bennett, and A. Auricchio. 2008. Serotype-dependent packaging of large genes in adeno-associated viral vectors results in effective gene delivery in mice. *J Clin Invest*. 118:1955-1964.

Ambati, J., J.P. Atkinson, and B.D. Gelfand. 2013. Immunology of age-related macular degeneration. *Nature reviews. Immunology*. 13:438-451.

Anderson, D.H., M.J. Radeke, N.B. Gallo, E.A. Chapin, P.T. Johnson, C.R. Curletti, L.S. Hancox, J. Hu, J.N. Ebright, G. Malek, M.A. Hauser, C.B. Rickman, D. Bok, G.S. Hageman, and L.V. Johnson. 2010. The pivotal role of the complement system in aging and age-related macular degeneration: hypothesis re-visited. *Prog Retin Eye Res*. 29:95-112.

Azarian, S.M., A.J. King, M.A. Hallett, and D.S. Williams. 1995. Selective proteolysis of arrestin by calpain. Molecular characteristics and its effect on rhodopsin dephosphorylation. *J Biol Chem*. 270:24375-24384.

Bacallao, R., C. Antony, C. Dotti, E. Karsenti, E.H.K. Stelzer, and K. Simons. 1989. The subcellular organization of Madin-Darby canine kidney cells during the formation of a polarized epithelium. *J Cell Biol*. 109:2817-2832.

Bainbridge, J.W., A.J. Smith, S.S. Barker, S. Robbie, R. Henderson, K. Balaggan, A. Viswanathan, G.E. Holder, A. Stockman, N. Tyler, S. Petersen-Jones, S.S. Bhattacharya, A.J. Thrasher, F.W. Fitzke, B.J. Carter, G.S. Rubin, A.T. Moore, and R.R. Ali. 2008. Effect of gene therapy on visual function in Leber's congenital amaurosis. *N Engl J Med*. 358:2231-2239.

Bakondi, B., W. Lv, B. Lu, M.K. Jones, Y. Tsai, K.J. Kim, R. Levy, A.A. Akhtar, J.J. Breunig, C.N. Svendsen, and S. Wang. 2016. In Vivo CRISPR/Cas9 Gene Editing Corrects Retinal Dystrophy in the S334ter-3 Rat Model of Autosomal Dominant Retinitis Pigmentosa. *Mol Ther*. 24:556-563.

Bennett, J., J. Wellman, K.A. Marshall, S. McCague, M. Ashtari, J. DiStefano-Pappas, O.U. Elci, D.C. Chung, J. Sun, J.F. Wright, D.R. Cross, P. Aravand, L.L. Cyckowski, J.L. Bennicelli, F. Mingozzi, A. Auricchio, E.A. Pierce, J. Ruggiero, B.P. Leroy, F. Simonelli, K.A. High,

and A.M. Maguire. 2016. Safety and durability of effect of contralateral-eye administration of AAV2 gene therapy in patients with childhood-onset blindness caused by RPE65 mutations: a follow-on phase 1 trial. *Lancet*. 388:661-672.

Bernstein, P.S., J. Tammur, N. Singh, A. Hutchinson, M. Dixon, C.M. Pappas, N.A. Zabriskie, K. Zhang, K. Petrukhin, M. Leppert, and R. Allikmets. 2001. Diverse macular dystrophy phenotype caused by a novel complex mutation in the *ELOVL4* gene. *IOVS*. 42:3331-3336.

Bhutto, I., and G. Lutty. 2012. Understanding age-related macular degeneration (AMD): relationships between the photoreceptor/retinal pigment epithelium/Bruch's membrane/choriocapillaris complex. *Mol Aspects Med*. 33:295-317.

Boal, D. 2012. Dynamic Filaments. *In* Mechanics of the Cell. D. Boal, editor. Cambridge University Press, Cambridge.

Boesze-Battaglia, K., F. Kong, O.P. Lamba, F.P. Stefano, and D.S. Williams. 1997. Purification and light-dependent phosphorylation of a candidate fusion protein, the photoreceptor cell peripherin/rds. *Biochemistry*. 36:6835-6846.

Bok, D. 1993. The retinal pigment epithelium: a versatile partner in vision. *J Cell Sci Suppl*. 17:189-195.

Bok, D., and M.O. Hall. 1971. The Role of the Pigment Epithelium in the Etiology of Inherited Retinal Dystrophy in the Rat. *The Journal of Cell Biology*. 49:664-682.

Bonilha, V.L. 2014. Retinal pigment epithelium (RPE) cytoskeleton in vivo and in vitro. *Exp Eye Res*. 126:38-45.

Booij, J.C., D.C. Baas, J. Beisekeeva, T.G. Gorgels, and A.A. Bergen. 2010. The dynamic nature of Bruch's membrane. *Prog Retin Eye Res*. 29:1-18.

Bosch, E., J. Horwitz, and D. Bok. 1993a. Phagocytosis of outer segments by retinal pigment epithelium: phagosome- lysosome interaction. *J Histochem Cytochem*. 41:253-263.

Bosch, E., J. Horwitz, and D. Bok. 1993b. Phagocytosis of outer segments by retinal pigment epithelium: phagosome–lysosome interaction. *J Histochem Cytochem.* 41.

Bowes Rickman, C., S. Farsiu, C.A. Toth, and M. Klingeborn. 2013. Dry age-related macular degeneration: mechanisms, therapeutic targets, and imaging. *Investigative ophthalmology & visual science*. 54:ORSF68-80.

Bre, M.-H., R. Pepperkok, A.M. Hill, N. Levilliers, W. Ansorge, E.H.K. Stelzer, and E. Karsenti. 1990. Regulation of microtubule dynamics and nucleation during polarization in MDCK II cells. *J Cell Biol*. 111:3013-3021.

Brunk, U.T., and A. Terman. 2002. Lipofuscin: Mechanisms of age-related accumulation and influence on cell function. *Free Radical Biology & Medicine*. 33:611-619.

Buchholz, D.E., S.T. Hikita, T.J. Rowland, A.M. Friedrich, C.R. Hinman, L.V. Johnson, and D.O. Clegg. 2009. Derivation of Functional Retinal Pigmented Epithelium from Induced Pluripotent Stem Cells. *Stem Cells* 27:2427-2434.

Buchholz, D.E., B.O. Pennington, R.H. Croze, C.R. Hinman, P.J. Coffey, and D.O. Clegg. 2013. Rapid and efficient directed differentiation of human pluripotent stem cells into retinal pigmented epithelium. *Stem Cells Transl Med*. 2:384-393.

Burke, J.M., C.M.B. Skumatz, P.E. Irving, and B.S. McKay. 1996. Phenotypic heterogeneity of retinal pigment epithelial cells in vitro and in situ. *Exp Eye Res*. 62:63-73.

Canto, C., R.H. Houtkooper, E. Pirinen, D.Y. Youn, M.H. Oosterveer, Y. Cen, P.J. Fernandez-Marcos, H. Yamamoto, P.A. Andreux, P. Cettour-Rose, K. Gademann, C. Rinsch, K. Schoonjans, A.A. Sauve, and J. Auwerx. 2012. The NAD(+) precursor nicotinamide riboside enhances oxidative metabolism and protects against high-fat diet-induced obesity. *Cell Metab*. 15:838-847.

Chan, F., W.W. Hauswirth, T.G. Wensel, and J.H. Wilson. 2011. Efficient mutagenesis of the rhodopsin gene in rod photoreceptor neurons in mice. *Nucleic Acids Res*. 39:5955-5966.

Chien, S.H.-L., D.Y. Teller, and J. Palmer. 2000. The transition from scotopic to photopic vision in 3-month-old infants and adults: an evaluation of the rod dominance hypothesis. *Vision Res*. 40:3853-3871.

Cong, L., F.A. Ran, D. Cox, S. Lin, R. Barretto, N. Habib, P.D. Hsu, X. Wu, W. Jiang, L.A. Marraffini, and F. Zhang. 2013. Multiplex genome engineering using CRISPR/Cas Systems. *Science*. 339:819-823.

Cope, M.J., J. Whisstock, I. Rayment, and J. Kendrick-Jones. 1996. Conservation within the myosin motor domain: implications for structure and function. *Cell Structure*. 4:969-987.

Curcio, C.A., N.E. Medeiros, and C.L. Millican. 1996. Photoreceptor loss in age-related macular degeneration. *Invest Ophthalmol Vis Sci*. 37:1236-1249.

D'Cruz, P.M., D. Yasumura, J. Weir, M.T. Matthes, H. Abderrahim, M.M. LaVail, and D. Vollrath. 2000. Mutation of the receptor tyrosine kinase gene *Mertk* in the retinal dystrophic RCS rat. *Hum Mol Genet*. 9:645-651.

Davis, A.A., P.S. Bernstein, D. Bok, J. Turner, M. Nachtigal, and R.C. Hunt. 1995. A human retinal pigment epithelial cell line that retains epithelial characteristics after prolonged culture. *Invest Ophthalmol Vis Sci*. 36:955-964.

Desjardins, M., L.A. Huber, R.G. Parton, and G. Griffiths. 1994. Biogenesis of phagolysosomes proceeds through a sequential series of interactions with the endocytic apparatus. *J Cell Biol*. 124:677-688.

Diemer, T., D. Gibbs, and D.S. Williams. 2008. Analysis of the Rate of Disk Membrane Digestion by Cultured RPE Cells. *Recent Advances in Retinal Degeneration*:321-326.

Ding, J.D., U. Kelly, M. Landowski, C.B. Toomey, M. Groelle, C. Miller, S.G. Smith, M. Klingeborn, T. Singhapricha, H. Jiang, M.M. Frank, and C. Bowes Rickman. 2015. Expression of human complement factor H prevents age-related macular degeneration-

like retina damage and kidney abnormalities in aged Cfh knockout mice. *Am J Pathol*. 185:29-42.

Dong, B., H. Nakai, and W. Xiao. 2010. Characterization of genome integrity for oversized recombinant AAV vector. *Mol Ther*. 18:87-92.

Duncan, J.L., M.M. LaVail, D. Yasumura, M.T. Matthes, H. Yang, N. Trautmann, A.V. Chappelow, W. Feng, H.S. Earp, G.K. Matsushima, and D. Vollrath. 2003. An RCS-Like Retinal Dystrophy Phenotype in Mer Knockout Mice. *invest Ophthalmol Vis Sci*. 44:826.

Dunn, K.C., A.E. Aotaki-Keen, F.R. Putkey, and L.M. Hjelmeland. 1996. ARPE-19, A Human Retinal Pigment Epithelial Cell Line with Differentiated Properties. *Exp. Eye Res.* 62:155-160.

Ebermann, I., H.P. Scholl, P. Charbel Issa, E. Becirovic, J. Lamprecht, B. Jurklies, J.M. Millan, E. Aller, D. Mitter, and H. Bolz. 2007. A novel gene for Usher syndrome type 2: mutations in the long isoform of whirlin are associated with retinitis pigmentosa and sensorineural hearing loss. *Hum Genet*. 121:203-211.

Edwards, A.O., L.A. Donoso, and R. Ritter, 3rd. 2001. A novel gene for autosomal dominant Stargardt-like macular dystrophy with homology to the SUR4 protein family. *Invest Ophthalmol Vis Sci*. 42:2652-2663.

Edwards, A.O., R. Ritter, 3rd, K.J. Abel, A. Manning, C. Panhuysen, and L.A. Farrer. 2005. Complement factor H polymorphism and age-related macular degeneration. *Science*. 308:421-424.

Edwards, R.B., and R.B. Szamier. 1977. Defective phagocytosis of isolated rod outer segments by RCS rat retinal pigment epithelium in culture. *Science*. 197:1001-1003.

Engelhardt, M., C. Tosha, V.S. Lopes, B. Chen, L. Nguyen, S. Nusinowitz, and D.S. Williams. 2012. Functional and morphological analysis of the subretinal injection of retinal pigment epithelium cells. *Vis Neurosci*. 29:83-93.

Esteve-Rudd, J., R.A. Hazim, T. Diemer, A.E. Paniagua, S. Volland, A. Umapathy, and D.S. Williams. 2018. Defective phagosome motility and degradation in cell nonautonomous RPE pathogenesis of a dominant macular degeneration. *Proc Natl Acad Sci U S A*. 115:5468-5473.

Esteve-Rudd, J., V.S. Lopes, M. Jiang, and D.S. Williams. 2014. In vivo and in vitro monitoring of phagosome maturation in retinal pigment epithelium cells. *Adv Exp Med Biol*. 801:85-90.

Fasler-Kan, E., N. Aliu, K. Wunderlich, S. Ketterer, S. Ruggiero, S. Berger, and P. Meyer. 2018. The Retinal Pigment Epithelial Cell Line (ARPE-19) Displays Mosaic Structural Chromosomal Aberrations. *Methods Mol Biol*. 1745:305-314.

Feeney, L. 1973. The phagolysosomal system of the pigment epithelium. A key to retinal disease. *Invest Ophthalmol*. 12:635-638.

Ferrer, M., B. Corneo, J. Davis, Q. Wan, K.J. Miyagishima, R. King, A. Maminishkis, J. Marugan, R. Sharma, M. Shure, S. Temple, S. Miller, and K. Bharti. 2014. A multiplex high-throughput gene expression assay to simultaneously detect disease and functional markers in induced pluripotent stem cell-derived retinal pigment epithelium. *Stem Cells Transl Med*. 3:911-922.

Finnemann, S.C., V.L. Bonilha, A.D. Marmostein, and E. Rodriguez-Boulan. 1997. Phagocytosis of rod outer segments by retinal pigment epithelial cells requires avb5 integrin for binding but not for internalization. *Proc Natl Acad Sci U S A*. 94:12932-12937.

Finnemann, S.C., L.W. Leung, and E. Rodriguez-Boulan. 2002. The lipofuscin component A2E selectively inhibits phagolysosomal degradation of photoreceptor phospholipid by the retinal pigment epithelium. *Proc Natl Acad Sci U S A*. 99:3842-3847.

Gal, A., Y. Li, D.A. Thompson, J. Weir, U. Orth, S.G. Jacobson, E. Apfelstedt-Sylla, and D. Vollrath. 2000. Mutations in MERTK, the human orthologue of the RCS rat retinal dystrophy gene, cause retinitis pigmentosa. *Nat Genet*. 26:270-271.

Garanto, A., D.C. Chung, L. Duijkers, J.C. Corral-Serrano, M. Messchaert, R. Xiao, J. Bennett, L.H. Vandenberghe, and R.W. Collin. 2016. In vitro and in vivo rescue of aberrant splicing in CEP290-associated LCA by antisense oligonucleotide delivery. *Hum Mol Genet*.

Ghosh, A., Y. Yue, and D. Duan. 2011. Efficient transgene reconstitution with hybrid dual AAV vectors carrying the minimized bridging sequences. *Hum Gene Ther*. 22:77-83.

Gibbs, D., S.M. Azarian, C. Lillo, J. Kitamoto, A.E. Klomp, K.P. Steel, R.T. Libby, and D.S. Williams. 2004. Role of myosin VIIa and Rab27a in the motility and localization of RPE melanosomes. *J Cell Sci*. 26:6473-6483.

Gibbs, D., T. Diemer, K. Khanobdee, J. Hu, D. Bok, and D.S. Williams. 2010. Function of MYO7A in the human RPE and the validity of shaker1 mice as a model for Usher syndrome 1B. *Invest Ophthalmol Vis Sci*. 51:1130-1135.

Gibbs, D., J. Kitamoto, and D.S. Williams. 2003. Abnormal phagocytosis by retinal pigmented epithelium that lacks myosin VIIa, the Usher syndrome 1B protein. *Proc Natl Acad Sci U S A*. 100:6481-6486.

Gibbs, D., and D.S. Williams. 2003. Isolation and culture of primary mouse retinal pigmented epithlelial cells. *Adv. Exp. Med. Biol.* 533:347-352.

Gibson, F., J. Walsh, P. Mburu, A. Varela, K.A. Brown, M. Antonio, K.W. Beisel, K.P. Steel, and S.D. Brown. 1995. A type VII myosin encoded by the mouse deafness gene shaker-1. *Nature*. 374:62-64.

Gilbert, T., A. Le Bivic, A. Quaroni, and E. Rodriguez-Boulan. 1991. Microtubular organization and its involvement in the biogenetic pathways of plasma membrane proteins in Caco-2 intestinal epithelial cells. *J Cell Biol*. 113:275-288.

Goldstein, L.S., and Z. Yang. 2000. Microtubule-based transport systems in neurons: the roles of kinesins and dyneins. *Annu Rev Neurosci*. 23:39-71.

Gomes, A.P., N.L. Price, A.J. Ling, J.J. Moslehi, M.K. Montgomery, L. Rajman, J.P. White, J.S. Teodoro, C.D. Wrann, B.P. Hubbard, E.M. Mercken, C.M. Palmeira, R. de Cabo, A.P. Rolo, N. Turner, E.L. Bell, and D.A. Sinclair. 2013. Declining NAD(+) induces a pseudohypoxic state disrupting nuclear-mitochondrial communication during aging. *Cell*. 155:1624-1638.

Gong, J., M.A. Fields, E.F. Moreira, H.E. Bowrey, M. Gooz, Z. Ablonczy, and L.V. Del Priore. 2015. Differentiation of Human Protein-Induced Pluripotent Stem Cells toward a Retinal Pigment Epithelial Cell Fate. *PLoS One*. 10:e0143272.

Goodson, H.V., C. Valetti, and T.E. Kreis. 1997. Motors and membrane traffic. *Current Opinion in Cell Biology*. 9:18-28.

Grayson, C., and R.S. Molday. 2005. Dominant negative mechanism underlies autosomal dominant Stargardt-like macular dystrophy linked to mutations in ELOVL4. *J Biol Chem*. 280:32521-32530.

Hageman, G.S., D.H. Anderson, L.V. Johnson, L.S. Hancox, A.J. Taiber, L.I. Hardisty, J.L. Hageman, H.A. Stockman, J.D. Borchardt, K.M. Gehrs, R.J. Smith, G. Silvestri, S.R. Russell, C.C. Klaver, I. Barbazetto, S. Chang, L.A. Yannuzzi, G.R. Barile, J.C. Merriam, R.T. Smith, A.K. Olsh, J. Bergeron, J. Zernant, J.E. Merriam, B. Gold, M. Dean, and R. Allikmets. 2005. A common haplotype in the complement regulatory gene factor H (HF1/CFH) predisposes individuals to age-related macular degeneration. *Proc Natl Acad Sci U S A*. 102:7227-7232.

Haines, J.L., M.A. Hauser, S. Schmidt, W.K. Scott, L.M. Olson, P. Gallins, K.L. Spencer, S.Y. Kwan, M. Noureddine, J.R. Gilbert, N. Schnetz-Boutaud, A. Agarwal, E.A. Postel, and M.A. Pericak-Vance. 2005. Complement factor H variant increases the risk of age-related macular degeneration. *Science*. 308:419-421.

Hartsock, A., and W.J. Nelson. 2008. Adherens and tight junctions: structure, function and connections to the actin cytoskeleton. *Biochim Biophys Acta*. 1778:660-669.

Hashimoto, T., D. Gibbs, C. Lillo, S.M. Azarian, E. Legacki, X.M. Zhang, X.J. Yang, and D.S. Williams. 2007. Lentiviral gene replacement therapy of retinas in a mouse model for Usher syndrome type 1B. *Gene Ther*. 14:584-594.

Hauswirth, W.W., T.S. Aleman, S. Kaushal, A.V. Cideciyan, S.B. Schwartz, L. Wang, T.J. Conlon, S.L. Boye, T.R. Flotte, B.J. Byrne, and S.G. Jacobson. 2008. Treatment of leber congenital amaurosis due to RPE65 mutations by ocular subretinal injection of adeno-associated virus gene vector: short-term results of a phase I trial. *Hum Gene Ther*. 19:979-990.

Hazim, R., M. Jiang, J. Esteve-Rudd, T. Diemer, V.S. Lopes, and D.S. Williams. 2016. Live-Cell Imaging of Phagosome Motility in Primary Mouse RPE Cells. *Adv Exp Med Biol*. 854:751-755.

Hazim, R.A., S. Karumbayaram, M. Jiang, A. Dimashkie, V.S. Lopes, D. Li, B.L. Burgess, P. Vijayaraj, J.A. Alva-Ornelas, J.A. Zack, D.B. Kohn, B.N. Gomperts, A.D. Pyle, W.E. Lowry, and D.S. Williams. 2017. Differentiation of RPE cells from integration-free iPS cells and their cell biological characterization. *Stem Cell Research & Therapy*. 8:1-17.

Hazim, R.A., and D.S. Williams. 2018. Cell Culture Analysis of the Phagocytosis of Photoreceptor Outer Segments by Primary Mouse RPE Cells. *Methods Mol Biol*. 1753:63-71.

Herman, K.G., and R.H. Steinberg. 1982a. Phagosome degradation in the tapetal retinal pigment epithelium of the opossum. *Invest Ophthalmol Vis Sci*. 23:291-304.

Herman, K.G., and R.H. Steinberg. 1982b. Phagosome movement and the diurnal pattern of phagocytosis in the tapetal retinal pigment epithelium of the opossum. *Invest Ophthalmol Vis Sci*. 23:277-290.

Hirsch, M.L., L. Green, M.H. Porteus, and R.J. Samulski. 2010. Self-complementary AAV mediates gene targeting and enhances endonuclease delivery for double-strand break repair. *Gene Ther*. 17:1175-1180.

Hirsch, M.L., C. Li, I. Bellon, C. Yin, S. Chavala, M. Pryadkina, I. Richard, and R.J. Samulski. 2013. Oversized AAV transductifon is mediated via a DNA-PKcs-independent, Rad51C-dependent repair pathway. *Mol Ther*. 21:2205-2216.

Hogan, M.J. 1972. Role of the retinal pigment epithelium in macular disease. *Trans Am Acad Ophthalmol Otolaryngol*. 76:64-80.

Hou, P., Y. Li, X. Zhang, C. Liu, J. Guan, H. Li, T. Zhao, J. Ye, W. Yang, K. Liu, J. Ge, J. Xu, Q. Zhang, Y. Zhao, and H. Deng. 2013. Pluripotent Stem Cells Induced from Mouse Somatic Cells by Small-Molecule Compounds. *Science*. 341:651-654.

Hu, C., L. Fan, P. Cen, E. Chen, Z. Jiang, and L. Li. 2016. Energy Metabolism Plays a Critical Role in Stem Cell Maintenance and Differentiation. *Int J Mol Sci*. 17:253.

Hu, J., and D. Bok. 2001. A cell culture medium that supports the differentiation of human retinal pigment epithelium into functionally polarized monolayers. *Molecular Vision*. 7:14-19.

Idelson, M., R. Alper, A. Obolensky, E. Ben-Shushan, I. Hemo, N. Yachimovich-Cohen, H. Khaner, Y. Smith, O. Wiser, M. Gropp, M.A. Cohen, S. Even-Ram, Y. Berman-Zaken, L. Matzrafi, G. Rechavi, E. Banin, and B. Reubinoff. 2009. Directed differentiation of human embryonic stem cells into functional retinal pigment epithelium cells. *Cell Stem Cell*. 5:396-408.

Ilieva, H., M. Polymenidou, and D.W. Cleveland. 2009. Non-cell autonomous toxicity in neurodegenerative disorders: ALS and beyond. *J Cell Biol*. 187:761-772.

Imai, H., S. Kuwayama, A. Onishi, T. Morizumi, O. Chisaka, and Y. Shichida. 2005. Molecular properties of rod and cone visual pigments from purified chicken cone pigments to mouse rhodopsin in situ. *Photochem Photobiol Sci*. 4:667-674.

Israel, M.A., S.H. Yuan, C. Bardy, S.M. Reyna, Y. Mu, C. Herrera, M.P. Hefferan, S. Van Gorp, K.L. Nazor, F.S. Boscolo, C.T. Carson, L.C. Laurent, M. Marsala, F.H. Gage, A.M. Remes, E.H. Koo, and L.S. Goldstein. 2012. Probing sporadic and familial Alzheimer's disease using induced pluripotent stem cells. *Nature*. 482:216-220.

Jacobson, S.G., A.V. Cideciyan, T.S. Aleman, A. Sumaroka, A.J. Roman, L.M. Gardner, H.M. Prosser, M. Mishra, N.T. Bech-Hansen, W. Herrera, S.B. Schwartz, X.Z. Liu, W.J. Kimberling, K.P. Steel, and D.S. Williams. 2008. Usher syndromes due to MYO7A, PCDH15, USH2A or GPR98 mutations share retinal disease mechanism. *Human molecular genetics*. 17:2405-2415.

Jang, S.Y., H.T. Kang, and E.S. Hwang. 2012. Nicotinamide-induced mitophagy: event mediated by high NAD+/NADH ratio and SIRT1 protein activation. *J Biol Chem*. 287:19304-19314.

Jiang, M., J. Esteve-Rudd, V.S. Lopes, T. Diemer, C. Lillo, A. Rump, and D.S. Williams. 2015. Microtubule motors transport phagosomes in the RPE, and lack of KLC1 leads to AMD-like pathogenesis. *J Cell Biol*. 210:595-611.

Jin, M., S. Li, W.N. Moghrabi, H. Sun, and G.H. Travis. 2005. Rpe65 is the retinoid isomerase in bovine retinal pigment epithelium. *Cell*. 122:449-459.

Kamao, H., M. Mandai, S. Okamoto, N. Sakai, A. Suga, S. Sugita, J. Kiryu, and M. Takahashi. 2014. Characterization of human induced pluripotent stem cell-derived retinal pigment epithelium cell sheets aiming for clinical application. *Stem Cell Reports*. 2:205-218.

Karan, G., C. Lillo, Z. Yang, D.J. Cameron, K.G. Locke, Y. Zhao, S. Thirumalaichary, C. Li, D.G. Birch, H.R. Vollmer-Snarr, D.S. Williams, and K. Zhang. 2005. Lipofuscin accumulation, abnormal electrophysiology, and photoreceptor degeneration in mutant ELOVL4 transgenic mice: a model for macular degeneration. *Proc Natl Acad Sci U S A*. 102:4164-4169.

Karan, G., Z. Yang, and K. Zhang. 2004. Expression of wildtype and mutant ELOVL4 in cell culture: subcellular localization and cell viability. *Mol Vis*. 10:248-253.

Karumbayaram, S., P. Lee, S.F. Azghadi, A.R. Cooper, M. Patterson, D.B. Kohn, A. Pyle, A. Clark, J. Byrne, J.A. Zack, K. Plath, and W.E. Lowry. 2012. From skin biopsy to neurons through a pluripotent intermediate under Good Manufacturing Practice protocols. *Stem Cells Transl Med*. 1:36-43.

Kawasaki, H., H. Suemori, K. Mizuseki, K. Watanabe, F. Urano, H. Ichinose, M. Haruta, M. Takahashi, K. Yoshikawa, S. Nishikawa, N. Nakatsuji, and Y. Sasai. 2002. Generation of dopaminergic neurons and pigmented epithelia from primate ES cells by stromal cell-derived inducing activity. *Proc Natl Acad Sci U S A*. 99:1580-1585.

Kim, D., C.H. Kim, J.I. Moon, Y.G. Chung, M.Y. Chang, B.S. Han, S. Ko, E. Yang, K.Y. Cha, R. Lanza, and K.S. Kim. 2009a. Generation of human induced pluripotent stem cells by direct delivery of reprogramming proteins. *Cell Stem Cell*. 4:472-476.

Kim, Y.H., S. He, S. Kase, M. Kitamura, S.J. Ryan, and D.R. Hinton. 2009b. Regulated secretion of complement factor H by RPE and its role in RPE migration. *Graefes Arch Clin Exp Ophthalmol*. 247:651-659.

Kimberling, W.J., and C. Moller. 1995. Clinical and molecular genetics of Usher syndrome. *Journal of the American Academy of Audiology*. 6:63-72.

Kiser, P.D., M. Golczak, and K. Palczewski. 2014. Chemistry of the retinoid (visual) cycle. *Chem Rev*. 114:194-232.

Klein, R.J., C. Zeiss, E.Y. Chew, J. Tsai, R.S. Sackler, C. Haynes, A.K. Henning, J.P. SanGiovanni, S.M. Mane, S.T. Mayne, M.B. Bracken, F.L. Ferris, J. Ott, C. Barnstable, and J. Hoh. 2005. Complement Factor H Polymorphism in Age-Related Macular Degeneration. *Science*. 308:385-389.

Klopfenstein, D.R., M. Tomishige, N. Stuurman, and R.D. Vale. 2002. Role of phosphatidylinositol(4,5)bisphosphate organization in membrane transport by the unc104 kinesin motor. *Cell*. 109:347-358.

Kokkinaki, M., N. Sahibzada, and N. Golestaneh. 2011. Human induced pluripotent stem-derived retinal pigment epithelium (RPE) cells exhibit ion transport, membrane potential, polarized vascular endothelial growth factor secretion, and gene expression pattern similar to native RPE. *Stem Cells*. 29:825-835.

Kolb, H. 2007. Gross Anatomy of the Eye. *In* Webvision: The Organization of the Retina and Visual System. H. Kolb, F. E., and R. Nelson, editors, Salt Lake City (UT): University of Utah Health Sciences Center. 3-11.

Kuny, S., W.J. Cho, I.S. Dimopoulos, and Y. Sauve. 2015. Early Onset Ultrastructural and Functional Defects in RPE and Photoreceptors of a Stargardt-Like Macular Dystrophy (STGD3) Transgenic Mouse Model. *Invest Ophthalmol Vis Sci*. 56:7109-7121.

Kuznetsova, A.V., A.M. Kurinov, and M.A. Aleksandrova. 2014. Cell models to study regulation of cell transformation in pathologies of retinal pigment epithelium. *J Ophthalmol*. 2014:801787.

Lagziel, A., N. Overlack, S.L. Bernstein, R.J. Morell, U. Wolfrum, and T.B. Friedman. 2009. Expression of cadherin 23 isoforms is not conserved: implications for a mouse model of Usher syndrome type 1D. *Mol Vis*. 15:1843-1857.

Lai, Y., Y. Yue, and D. Duan. 2010. Evidence for the failure of adeno-associated virus serotype 5 to package a viral genome $\geq$ 8.2 kb. *Mol Ther*. 18:75-79.

LaVail, M.M. 1976. Rod outer segment disk shedding in rat retina: relationship to cyclic lighting. *Science*. 194:1071-1074.

Leach, L.L., R.H. Croze, Q. Hu, V.P. Nadar, T.N. Clevenger, B.O. Pennington, D.M. Gamm, and D.O. Clegg. 2016. Induced Pluripotent Stem Cell-Derived Retinal Pigmented Epithelium: A Comparative Study Between Cell Lines and Differentiation Methods. *J Ocul Pharmacol Ther*. 32:317-330.

Lebrand, C., M. Corti, H. Goodson, P. Cosson, V. Cavalli, N. Mayran, J. Faure, and J. Gruenberg. 2002. Late endosome motility depends on lipids via the small GTPase Rab7. *EMBO*. 21:1289-1300.

Lehmann, G.L., I. Benedicto, N.J. Philp, and E. Rodriguez-Boulan. 2014. Plasma membrane protein polarity and trafficking in RPE cells: past, present and future. *Exp Eye Res*. 126:5-15.

Lenis, T.L., S. Ng, J. Hu, Z. Jiang, M. Lloyd, N. Esposito, D. Bok, S.C. Finnemann, G.H. Travis, and R.A. Radu. 2018. Localization of ABCA4 in the retinal pigment epithelium and its implications for Stargardt disease. *Invest Ophthalmol Vis Sci ARVO E-Abstr*. 4502.

Lentz, J.J., F.M. Jodelka, A.J. Hinrich, K.E. McCaffrey, H.E. Farris, M.J. Spalitta, N.G. Bazan, D.M. Duelli, F. Rigo, and M.L. Hastings. 2013. Rescue of hearing and vestibular function by antisense oligonucleotides in a mouse model of human deafness. *Nat Med*. 19:345-350.

Liao, J.L., J. Yu, K. Huang, J. Hu, T. Diemer, Z. Ma, T. Dvash, X.J. Yang, G.H. Travis, D.S. Williams, D. Bok, and G. Fan. 2010. Molecular signature of primary retinal pigment epithelium and stem-cell-derived RPE cells. *Hum Mol Genet*. 19:4229-4238.

Lin, H., and D.O. Clegg. 1998. Integrin Alpha V beta 5 Participates in the Binding of Photoreceptor Rod Outer Segments during Phagocytosis by Cultured Human Retinal Pigment Epithelium. *Invest Ophthalmol Vis Sci*. 39:1703-1712.

Liu, X., B. Ondek, and D.S. Williams. 1998. Mutant myosin VIIa causes defective melanosome distribution in the RPE of shaker-1 mice. *Nat Genet*. 19:117-118.

Liu, X., I.P. Udovichenko, S.D.M. Brown, K.P. Steel, and D.S. Williams. 1999. Myosin VIIa participates in opsin transport through the photoreceptor cilium. *J Neurosci*. 19:6267-6274.

Liu, X., G. Vansant, I.P. Udovichenko, U. Wolfrum, and D.S. Williams. 1997. Myosin VIIa, the product of the Usher 1B syndrome gene, is concentrated in the connecting cilia of photoreceptor cells. *Cell Motil. Cytoskel.* 37:240-252.

Logan, S., M.P. Agbaga, M.D. Chan, N. Kabir, N.A. Mandal, R.S. Brush, and R.E. Anderson. 2013. Deciphering mutant ELOVL4 activity in autosomal-dominant Stargardt macular dystrophy. *Proceedings of the National Academy of Sciences of the United States of America*. 110:5446-5451.

Lopes, V.S., S.E. Boye, C.M. Louie, S. Boye, F. Dyka, V. Chiodo, H. Fofo, W.W. Hauswirth, and D.S. Williams. 2013. Retinal gene therapy with a large MYO7A cDNA using adeno-associated virus. *Gene Ther*. 20:824-833.

Maguire, A.M., F. Simonelli, E.A. Pierce, E.N. Pugh, Jr., F. Mingozzi, J. Bennicelli, S. Banfi, K.A. Marshall, F. Testa, E.M. Surace, S. Rossi, A. Lyubarsky, V.R. Arruda, B. Konkle, E. Stone, J. Sun, J. Jacobs, L. Dell'Osso, R. Hertle, J.X. Ma, T.M. Redmond, X. Zhu, B. Hauck, O. Zelenaia, K.S. Shindler, M.G. Maguire, J.F. Wright, N.J. Volpe, J.W. McDonnell, A. Auricchio, K.A. High, and J. Bennett. 2008. Safety and efficacy of gene transfer for Leber's congenital amaurosis. *N Engl J Med*. 358:2240-2248.

Maminishkis, A., S. Chen, S. Jalickee, T. Banzon, G. Shi, F.E. Wang, T. Ehalt, J.A. Hammer, and S.S. Miller. 2006. Confluent monolayers of cultured human fetal retinal pigment epithelium exhibit morphology and physiology of native tissue. *Invest Ophthalmol Vis Sci*. 47:3612-3624.

Mandai, M., A. Watanabe, Y. Kurimoto, Y. Hirami, C. Morinaga, T. Daimon, M. Fujihara, H. Akimaru, N. Sakai, Y. Shibata, M. Terada, Y. Nomiya, S. Tanishima, M. Nakamura, H. Kamao, S. Sugita, A. Onishi, T. Ito, K. Fujita, S. Kawamata, M.J. Go, C. Shinohara, K.I. Hata, M. Sawada, M. Yamamoto, S. Ohta, Y. Ohara, K. Yoshida, J. Kuwahara, Y. Kitano, N. Amano, M. Umekage, F. Kitaoka, A. Tanaka, C. Okada, N. Takasu, S. Ogawa, S. Yamanaka, and M. Takahashi. 2017. Autologous Induced Stem-Cell-Derived Retinal Cells for Macular Degeneration. *N Engl J Med*. 376:1038-1046.

Mandal, N.A., J.T. Tran, L. Zheng, J.L. Wilkerson, R.S. Brush, J. McRae, M.P. Agbaga, K. Zhang, K. Petrukhin, R. Ayyagari, and R.E. Anderson. 2014. In vivo effect of mutant ELOVL4 on the expression and function of wild-type ELOVL4. *Invest Ophthalmol Vis Sci*. 55:2705-2713.

Mannu, G.S. 2014. Retinal phototransduction. *Neurosciences*. 19:275-280.

Maruotti, J., S.R. Sripathi, K. Bharti, J. Fuller, K.J. Wahlin, V. Ranganathan, V.M. Sluch, C.A. Berlinicke, J. Davis, C. Kim, L. Zhao, J. Wan, J. Qian, B. Corneo, S. Temple, R. Dubey, B.Z. Olenyuk, I. Bhutto, G. Lutty, and D.J. Zack. 2015. Small-molecule-directed, efficient generation of retinal pigment epithelium from human pluripotent stem cells. *Proc Natl Acad Sci U S A*. 112:10950-10955.

Maugeri, A., F. Meire, C.B. Hoyng, C. Vink, N. Van Regemorter, G. Karan, Z. Yang, F.P. Cremers, and K. Zhang. 2004. A novel mutation in the ELOVL4 gene causes autosomal dominant Stargardt-like macular dystrophy. *Invest Ophthalmol Vis Sci*. 45:4263-4267.

Mazzoni, F., H. Safa, and S.C. Finnemann. 2014. Understanding photoreceptor outer segment phagocytosis: use and utility of RPE cells in culture. *Exp Eye Res*. 126:51-60.

McKay, B.S., P.E. Irving, C.M.B. Skumatz, and J.M. Burke. 1997. Cell-cell adhesion molecules and the development of an epithelial phenotype in cultured human retinal pigment epithelial cells. *Exp Eye Res*. 65:661-671.

Meads, T., and T.A. Schroer. 1995 Polarity and nucleation of microtubules in polarized epithelial cells. *Cell Motility and the Cytoskeleton*. 32:273-288.

Mitchell, S.J., M. Bernier, M.A. Aon, S. Cortassa, E.Y. Kim, E.F. Fang, H.H. Palacios, A. Ali, I. Navas-Enamorado, A. Di Francesco, T.A. Kaiser, T.B. Waltz, N. Zhang, J.L. Ellis, P.J. Elliott, D.W. Frederick, V.A. Bohr, M.S. Schmidt, C. Brenner, D.A. Sinclair, A.A. Sauve, J.A. Baur, and R. de Cabo. 2018. Nicotinamide Improves Aspects of Healthspan, but Not Lifespan, in Mice. *Cell Metab*. 27:667-676 e664.

Miyagishima, K.J., Q. Wan, B. Corneo, R. Sharma, M.R. Lotfi, N.C. Boles, F. Hua, A. Maminishkis, C. Zhang, T. Blenkinsop, V. Khristov, B.S. Jha, O.S. Memon, S. D'Souza, S. Temple, S.S. Miller, and K. Bharti. 2016. In Pursuit of Authenticity: Induced Pluripotent Stem Cell-Derived Retinal Pigment Epithelium for Clinical Applications. *Stem Cells Transl Med*. 5:1562-1574.

Montezuma, S.R., L. Sobrin, and J.M. Seddon. 2007. Review of genetics in age related macular degeneration. *Semin Ophthalmol*. 22:229-240.

Musch, A. 2004. Microtubule organization and function in epithelial cells. *Traffic*. 5:1-9.

Nagel-Wolfrum, K., M. Becker, T. Goldmann, C. Müller, J. Vetter, and U. Wolfrum. 2011. USH1C Transcripts And Harmonin Protein Expression In Human Retina. *Investigative Ophthalmology & Visual Science*. 52:45-45.

Nandrot, E.F., M. Anand, D. Almeida, K. Atabai, D. Sheppard, and S.C. Finnemann. 2007. Essential role for MFG-E8 as ligand for alphavbeta5 integrin in diurnal retinal phagocytosis. *Proc Natl Acad Sci U S A*. 104:12005-12010.

Nandrot, E.F., Y. Kim, S.E. Brodie, X. Huang, D. Sheppard, and S.C. Finnemann. 2004. Loss of synchronized retinal phagocytosis and age-related blindness in mice lacking alphavbeta5 integrin. *J Exp Med*. 200:1539-1545.

Nelson, S.R., K.M. Trybus, and D.M. Warshaw. 2014. Motor coupling through lipid membranes enhances transport velocities for ensembles of myosin Va. *Proc Natl Acad Sci U S A*. 111:E3986-E3995.

Nusrat, A., J.R. Turner, and J.L. Madara. 2000. Molecular physiology and pathophysiology of tight junctions IV. Regulation of tight junctions by extracellular stimuli: nutrients, cytokines, and immune cells. *Am J Physiol Gastrointest Liver Physiol*. 279:G851-G857.

Okada, Y., H. Yamazaki, Y. Sekine-Aizawa, and N. Hirokawa. 1995. The neuron-specific kinesin superfamily protein KIF1A is a unique monomeric motor for anterograde axonal transport of synaptic vesicle precursors. *Cell*. 81:769-780.

Peng, S., V.S. Rao, R.A. Adelman, and L.J. Rizzolo. 2011. Claudin-19 and the barrier properties of the human retinal pigment epithelium. *Invest Ophthalmol Vis Sci*. 52:1392-1403.

Quinn, R.H., and S.S. Miller. 1992. Ion Transport Mechanisms in Native Human Retinal Pigment Epithelium. *Invest Ophthalmol Vis Sci*. 33:3513-3527.

Radu, R.A., J. Hu, Q. Yuan, D.L. Welch, J. Makshanoff, M. Lloyd, S. McMullen, G.H. Travis, and D. Bok. 2011. Complement system dysregulation and inflammation in the retinal pigment epithelium of a mouse model for Stargardt macular degeneration. *J Biol Chem*. 286:18593-18601.

Rahner, C., M. Fukuhara, S. Peng, S. Kojima, and L.J. Rizzolo. 2004. The apical and basal environments of the retinal pigment epithelium regulate the maturation of tight junctions during development. *J Cell Sci*. 117:3307-3318.

Rai, A., D. Pathak, S. Thakur, S. Singh, Alok K. Dubey, and R. Mallik. 2016. Dynein Clusters into Lipid Microdomains on Phagosomes to Drive Rapid Transport toward Lysosomes. *Cell*. 164:722-734.

Rakoczy, P.E., D. Zhang, T. Robertson, N.L. Barnett, J. Papadimitriou, I.J. Constable, and C.M. Lai. 2002. Progressive age-related changes similar to age-related macular degeneration in a transgenic mouse model. *Am J Pathol*. 161:1515-1524.

Ran, F.A., P.D. Hsu, J. Wright, V. Agarwala, D.A. Scott, and F. Zhang. 2013. Genome engineering using the CRISPR-Cas9 system. *Nat Protoc*. 8:2281-2308.

Rapaport, D.H. 2006. Retinal Neurogenesis. *In* Retinal Development. E. Sernagor, S. Eglen, B. Harris, and R. Wong, editors. Cambridge University Press, Cambridge. 30-58.

Rhyu, D.Y., Y. Yang, H. Ha, G.T. Lee, J.S. Song, S.T. Uh, and H.B. Lee. 2005. Role of reactive oxygen species in TGF-beta1-induced mitogen-activated protein kinase activation and epithelial-mesenchymal transition in renal tubular epithelial cells. *J Am Soc Nephrol*. 16:667-675.

Riazuddin, S., I.A. Belyantseva, A. Giese, K. Lee, A.A. Indzhykulian, S.P. Nandamuri, R. Yousaf, G.P. Sinha, S. Lee, D. Terrell, R.S. Hegde, R.A. Ali, S. Anwar, P.B. Andrade-Elizondo, A. Sirmaci, L.V. Parise, S. Basit, A. Wali, M. Ayub, M. Ansar, W. Ahmad, S.N. Khan, J. Akram, M. Tekin, S. Riazuddin, T. Cook, E.K. Buschbeck, G.I. Frolenkov, S.M. Leal, T.B. Friedman, and Z.M. Ahmed. 2012. Mutations in CIB2, a calcium and integrin binding protein, cause Usher syndrome type 1J and nonsyndromic deafness DFNB48. *Nature genetics*. 44:1265-1271.

Rizzolo, L.J. 2007. Development and Role of Tight Junctions in the Retinal Pigment Epithelium. *Int Rev Cytol*. 258:195-234.

Rocha, N., C. Kuijl, R.V.D. Kant, L. Janssen, D. Houben, H. Janssen, W. Zwart, and J. Neefjes. 2009. Cholesterol sensor ORP1L contacts the ER protein VAP to control Rab7-RILP-p150 Glued and late endosome positioning. *J Cell Biol*. 185:1209-1225.

Rodriguez-Boulan, E., and I.G. Macara. 2014. Organization and execution of the epithelial polarity programme. *Nat Rev Mol Cell Biol*. 15:225-242.

Ruggiero, L., M.P. Connor, J. Chen, R. Langen, and S.C. Finnemann. 2012. Diurnal, localized exposure of phosphatidylserine by rod outer segment tips in wild-type but not Itgb5-/- or Mfge8-/- mouse retina. *Proc Natl Acad Sci U S A*. 109:8145-8148.

Saini, J.S., B. Corneo, J.D. Miller, T.R. Kiehl, Q. Wang, N.C. Boles, T.A. Blenkinsop, J.H. Stern, and S. Temple. 2017. Nicotinamide Ameliorates Disease Phenotypes in a Human iPSC Model of Age-Related Macular Degeneration. *Cell Stem Cell*. 20:1-13.

Samuel, W., C. Jaworski, O.A. Postnikova, K. Kutty, T. Duncan, L.X. Tan, E. Poliakov, A. Lakkaraju, and T.M. Redmond. 2017. Appropriately differentiated ARPE-19 cells regain phenotype and gene expression profiles similar to those of native RPE cells. *Mol Vis*. 23:60-89.

Schwartz, S.D., J.-P. Hubschman, G. Heilwell, V. Franco-Cardenas, C.K. Pan, R.M. Ostrick, E. Mickunas, R. Gay, I. Klimanskaya, and R. Lanza. 2012. Embryonic stem cell trials for macular degeneration: a preliminary report. *The Lancet*. 379:713-720.

Sethna, S., T. Chamakkala, X. Gu, T.C. Thompson, G. Cao, M.H. Elliott, and S.C. Finnemann. 2016. Regulation of Phagolysosomal Digestion by Caveolin-1 of the Retinal Pigment Epithelium Is Essential for Vision. *J Biol Chem*. 291:6494-6506.

Shaw, P.X., L. Zhang, M. Zhang, H. Du, L. Zhao, C. Lee, S. Grob, S.L. Lim, G. Hughes, J. Lee, M. Bedell, M.H. Nelson, F. Lu, M. Krupa, J. Luo, H. Ouyang, Z. Tu, Z. Su, J. Zhu, X. Wei, Z. Feng, Y. Duan, Z. Yang, H. Ferreyra, D.U. Bartsch, I. Kozak, L. Zhang, F. Lin, H. Sun, H. Feng, and K. Zhang. 2012. Complement factor H genotypes impact risk of age-related macular degeneration by interaction with oxidized phospholipids. *Proc Natl Acad Sci U S A*. 109:13757-13762.

Shyh-Chang, N., G.Q. Daley, and L.C. Cantley. 2013. Stem cell metabolism in tissue development and aging. *Development*. 140:2535-2547.

Singh, R., M.J. Phillips, D. Kuai, J. Meyer, J.M. Martin, M.A. Smith, E.T. Perez, W. Shen, K.A. Wallace, E.E. Capowski, L.S. Wright, and D.M. Gamm. 2013a. Functional analysis of serially expanded human iPS cell-derived RPE cultures. *Investigative ophthalmology & visual science*. 54:6767-6778.

Singh, R., W. Shen, D. Kuai, J.M. Martin, X. Guo, M.A. Smith, E.T. Perez, M.J. Phillips, J.M. Simonett, K.A. Wallace, A.D. Verhoeven, E.E. Capowski, X. Zhang, Y. Yin, P.J. Halbach, G.A. Fishman, L.S. Wright, B.R. Pattnaik, and D.M. Gamm. 2013b. iPS cell modeling of Best disease: insights into the pathophysiology of an inherited macular degeneration. *Hum Mol Genet*. 22:593-607.

Sommer, J.R., J.L. Estrada, E.B. Collins, M. Bedell, C.A. Alexander, Z. Yang, G. Hughes, B. Mir, B.C. Gilger, S. Grob, X. Wei, J.A. Piedrahita, P.X. Shaw, R.M. Petters, and K. Zhang. 2011. Production of ELOVL4 transgenic pigs: a large animal model for Stargardt-like macular degeneration. *Br J Ophthalmol*. 95:1749-1754.

Sonoda, S., C. Spee, E. Barron, S.J. Ryan, R. Kannan, and D.R. Hinton. 2009. A protocol for the culture and differentiation of highly polarized human retinal pigment epithelial cells. *Nat Protoc*. 4:662-673.

Sparrow, J.R., and M. Boulton. 2005. RPE lipofuscin and its role in retinal pathobiology. *Exp Eye Res*. 80:595-606.

Sparrow, J.R., D. Hicks, and C.P. Hamel. 2010. The retinal pigment epithelium in health and disease. *Curr Mol Med*. 10:802-823.

Spiteri Cornish, K., J. Ho, S. Downes, N.W. Scott, J. Bainbridge, and N. Lois. 2017. The Epidemiology of Stargardt Disease in the United Kingdom. *Ophthalmology Retina*. 1:508-513.

Stanzel, B.V., Z. Liu, S. Somboonthanakij, W. Wongsawad, R. Brinken, N. Eter, B. Corneo, F.G. Holz, S. Temple, J.H. Stern, and T.A. Blenkinsop. 2014. Human RPE stem cells grown

into polarized RPE monolayers on a polyester matrix are maintained after grafting into rabbit subretinal space. *Stem Cell Reports*. 2:64-77.

Strauss, O. 2005. The retinal pigment epithelium in visual function. *Physiol Rev*. 85:845-881.

Strunnikova, N.V., A. Maminishkis, J.J. Barb, F. Wang, C. Zhi, Y. Sergeev, W. Chen, A.O. Edwards, D. Stambolian, G. Abecasis, A. Swaroop, P.J. Munson, and S.S. Miller. 2010. Transcriptome analysis and molecular signature of human retinal pigment epithelium. *Hum Mol Genet*. 19:2468-2486.

Sugita, S., Y. Iwasaki, K. Makabe, H. Kamao, M. Mandai, T. Shiina, K. Ogasawara, Y. Hirami, Y. Kurimoto, and M. Takahashi. 2016. Successful Transplantation of Retinal Pigment Epithelial Cells from MHC Homozygote iPSCs in MHC-Matched Models. *Stem Cell Reports*. 7:635-648.

Sun, H., and J. Nathans. 2000. ABCR: rod photoreceptor-specific ABC transporter responsible for Stargardt disease. *Methods Enzymol*. 315:879-897.

Svitkina, T. 2018. The Actin Cytoskeleton and Actin-Based Motility. *Cold Spring Harb Perspect Biol*. 10.

Takahashi, K., K. Tanabe, M. Ohnuki, M. Narita, T. Ichisaka, K. Tomoda, and S. Yamanaka. 2007. Induction of pluripotent stem cells from adult human fibroblasts by defined factors. *Cell*. 131:861-872.

Thomson, J.A., J. Itskovitz-Eldor, S.S. Shapiro, M.A. Waknitz, J.J. Swiergiel, V.S. Marshall, and J.M. Jones. 1998. Embryonic stem cell lines derived from human blastocysts. *Science*. 282:1145-1146.

Toops, K.A., L.X. Tan, Z. Jiang, R.A. Radu, and A. Lakkaraju. 2015. Cholesterol-mediated activation of acid sphingomyelinase disrupts autophagy in the retinal pigment epithelium. *Mol Biol Cell*. 26:1-14.

Toops, K.A., L.X. Tan, and A. Lakkaraju. 2014. A detailed three-step protocol for live imaging of intracellular traffic in polarized primary porcine RPE monolayers. *Exp Eye Res*. 124:74-85.

Trapani, I., P. Colella, A. Sommella, C. Iodice, G. Cesi, S. de Simone, E. Marrocco, S. Rossi, M. Giunti, A. Palfi, G.J. Farrar, R. Polishchuk, and A. Auricchio. 2014. Effective delivery of large genes to the retina by dual AAV vectors. *EMBO Mol Med*. 6:194-211.

Trapani, I., E. Toriello, S. de Simone, P. Colella, C. Iodice, E.V. Polishchuk, A. Sommella, L. Colecchi, S. Rossi, F. Simonelli, M. Giunti, M.L. Bacci, R.S. Polishchuk, and A. Auricchio. 2015. Improved dual AAV vectors with reduced expression of truncated proteins are safe and effective in the retina of a mouse model of Stargardt disease. *Hum Mol Genet*. 24:6811-6825.

Turksen, K., and V.I. Kalnins. 1987. The cytoskeleton of chick retinal pigment epithelial cells in situ. *Cell Tissue Res*. 248:95-101.

Vale, R.D. 2003. The molecular motor toolbox for intracellular transport. *Cell*. 112:467-480.

van Wijk, E., R.J. Pennings, H. te Brinke, A. Claassen, H.G. Yntema, L.H. Hoefsloot, F.P. Cremers, C.W. Cremers, and H. Kremer. 2004. Identification of 51 novel exons of the Usher syndrome type 2A (USH2A) gene that encode multiple conserved functional domains and that are mutated in patients with Usher syndrome type II. *Am J Hum Genet*. 74:738-744.

Vasireddy, V., M.M. Jablonski, N.W. Khan, X.F. Wang, P. Sahu, J.R. Sparrow, and R. Ayyagari. 2009. Elovl4 5-bp deletion knock-in mouse model for Stargardt-like macular degeneration demonstrates accumulation of ELOVL4 and lipofuscin. *Exp Eye Res*. 89:905-912.

Vasireddy, V., M.M. Jablonski, M.N. Mandal, D. Raz-Prag, X.F. Wang, L. Nizol, A. Iannaccone, D.C. Musch, R.A. Bush, N. Salem, Jr., P.A. Sieving, and R. Ayyagari. 2006. Elovl4 5-bp-

deletion knock-in mice develop progressive photoreceptor degeneration. *Investigative ophthalmology & visual science*. 47:4558-4568.

Vastinsalo, H., R. Jalkanen, A. Dinculescu, J. Isosomppi, S. Geller, J.G. Flannery, W.W. Hauswirth, and E.M. Sankila. 2011. Alternative splice variants of the USH3A gene Clarin 1 (CLRN1). *Eur J Hum Genet*. 19:30-35.

Vieira, O.V., R.J. Botelho, and S. Grinstein. 2002. Phagosome maturation: aging gracefully. *Biochemical Journal* 366:689-704.

Volland, S., J. Esteve-Rudd, J. Hoo, C. Yee, and D.S. Williams. 2015. A comparison of some organizational characteristics of the mouse central retina and the human macula. *PLoS One*. 10:e0125631.

Wang, Z., Y. Li, and F.H. Sarkar. 2010. Signaling mechanism(S) of reactive oxygen species in epithelial-mesenchymal transition reminiscent of cancer stem cells in tumor progression. *Curr Stem Cell Res Ther*. 5:74-80.

Warren, L., P.D. Manos, T. Ahfeldt, Y.H. Loh, H. Li, F. Lau, W. Ebina, P.K. Mandal, Z.D. Smith, A. Meissner, G.Q. Daley, A.S. Brack, J.J. Collins, C. Cowan, T.M. Schlaeger, and D.J. Rossi. 2010. Highly efficient reprogramming to pluripotency and directed differentiation of human cells with synthetic modified mRNA. *Cell Stem Cell*. 7:618-630.

Wavre-Shapton, S.T., I.P. Meschede, M.C. Seabra, and C.E. Futter. 2014. Phagosome maturation during endosome interaction revealed by partial rhodopsin processing in retinal pigment epithelium. *J Cell Sci*. 127:3852-3861.

Wavre-Shapton, S.T., T. Tolmachova, M. Lopes da Silva, C.E. Futter, and M.C. Seabra. 2013. Conditional ablation of the choroideremia gene causes age-related changes in mouse retinal pigment epithelium. *PloS one*. 8:e57769.

Weil, D., S. Blanchard, J. Kaplan, P. Guilford, F. Gibson, J. Walsh, P. Mburu, A. Varela, J. Levilliers, M.D. Weston, P.M. Kelley, W.J. Kimberling, M. Wagenaar, F. Levi-Acobas, D.

Larget-Piet, A. Munnich, K.P. Steel, S.D.M. Brown, and C. Petit. 1995. Defective myosin VIIA gene responsible for Usher syndrome type 1B. *Nature*. 374:60-61.

Weil, D., G. Levy, I. Sahly, F. Levi-Acobas, S. Blanchard, A. El-Amraoui, F. Crozet, H. Philippe, M. Abitbol, and C. Petit. 1996. Human myosin VIIA responsible for the Usher 1B syndrome: a predicted membrane-associated motor protein expressed in developing sensory epithelia. *Proc Natl Acad Sci U S A*. 93:3232-3237.

Weismann, D., K. Hartvigsen, N. Lauer, K.L. Bennett, H.P. Scholl, P. Charbel Issa, M. Cano, H. Brandstatter, S. Tsimikas, C. Skerka, G. Superti-Furga, J.T. Handa, P.F. Zipfel, J.L. Witztum, and C.J. Binder. 2011. Complement factor H binds malondialdehyde epitopes and protects from oxidative stress. *Nature*. 478:76-81.

Weng, J., N.L. Mata, S.M. Azarian, R.T. Tzekov, D.G. Birch, and G.H. Travis. 1999. Insights into the function of Rim protein in photoreceptors and etiology of Stargardt's disease from the phenotype in abcr knockout mice. *Cell*. 98:13-23.

Wenzel, A., V. Oberhauser, E.N. Pugh, Jr., T.D. Lamb, C. Grimm, M. Samardzija, E. Fahl, M.W. Seeliger, C.E. Reme, and J. von Lintig. 2005. The retinal G protein-coupled receptor (RGR) enhances isomerohydrolase activity independent of light. *J Biol Chem*. 280:29874-29884.

Weston, M.D., M.W. Luijendijk, K.D. Humphrey, C. Moller, and W.J. Kimberling. 2004. Mutations in the VLGR1 gene implicate G-protein signaling in the pathogenesis of Usher syndrome type II. *Am J Hum Genet*. 74:357-366.

Williams, D.S., A. Chadha, R. Hazim, and D. Gibbs. 2017. Gene therapy approaches for prevention of retinal degeneration in Usher syndrome. *Gene Ther*. 24:68-71.

Williams, D.S., and S.K. Fisher. 1987. Prevention of the shedding of rod outer segment disks by detachment from the retinal pigment epithelium. *Invest. Ophthalmol. Vis. Sci.* 28:184-187.

Wu, W.H., Y.T. Tsai, S. Justus, T.T. Lee, L. Zhang, C.S. Lin, A.G. Bassuk, V.B. Mahajan, and S.H. Tsang. 2016. CRISPR Repair Reveals Causative Mutation in a Preclinical Model of Retinitis Pigmentosa. *Mol Ther*. 24:1388-1394.

Wu, Z., H. Yang, and P. Colosi. 2010. Effect of genome size on AAV vector packaging. *Mol Ther*. 18:80-86.

Yang, L., P. Mali, C. Kim-Kiselak, and G. Church. 2014. CRISPR-Cas-mediated targeted genome editing in human cells. *Methods Mol Biol*. 1114:245-267.

Yoshioka, N., E. Gros, H.R. Li, S. Kumar, D.C. Deacon, C. Maron, A.R. Muotri, N.C. Chi, X.D. Fu, B.D. Yu, and S.F. Dowdy. 2013. Efficient generation of human iPSCs by a synthetic self-replicative RNA. *Cell Stem Cell*. 13:246-254.

Youn, Y.H., J. Hong, and J.M. Burke. 2006. Cell phenotype in normal epithelial cell lines with high endogenous N-cadherin: comparison of RPE to an MDCK subclone. *Invest Ophthalmol Vis Sci*. 47:2675-2685.

Young, R.W. 1967. The renewal of photoreceptor cell outer segments. *J. Cell Biol.* 33:61-72.

Young, R.W. 1971. The Renewal of Rod and Cone Outer Segments in the Rhesus Monkey. *The Journal of Cell Biology*. 49:303-318.

Young, R.W., and D. Bok. 1969. Participation of the retinal pigment epithelium in the rod outer segment renewal process. . *J Cell Biol*. 42:392-403.

Yu, J., K. Hu, K. Smuga-Otto, S. Tian, R. Stewart, I.I. Slukvin, and J.A. Thomson. 2009. Human Induced Pluripotent Stem Cells Free of Vector and Transgene Sequences *Science*. 324:797-801.

Zarbin, M.A. 2004. Current concepts in the pathogenesis of age-related macular degeneration. *Arch Ophthalmol*. 122:598-614.

Zetsche, B., J.S. Gootenberg, O.O. Abudayyeh, I.M. Slaymaker, K.S. Makarova, P. Essletzbichler, S.E. Volz, J. Joung, J. van der Oost, A. Regev, E.V. Koonin, and F.

Zhang. 2015. Cpf1 is a single RNA-guided endonuclease of a class 2 CRISPR-Cas system. *Cell*. 163:759-771.

Zhang, K., M. Kniazeva, M. Han, W. Li, Z. Yu, Z. Yang, Y. Li, M.L. Metzker, R. Allikmets, D.J. Zack, L.E. Kakuk, P.S. Lagali, P.W. Wong, I.M. MacDonald, P.A. Sieving, D.J. Figueroa, C.P. Austin, R.J. Gould, R. Ayyagari, and K. Petrukhin. 2001. A 5-bp deletion in ELOVL4 is associated with two related forms of autosomal dominant macular dystrophy. *Nat Genet*. 27:89-93.